UNIVERSITY OF CALIFORNIA, SAN DIEGO

Dynamic Testing and Properties of Rubber O-rings and Their Application in Soft Drop Weight Tests of Low Strength Materials

A dissertation submitted in partial satisfaction of the

requirements for the degree of Doctor of Philosophy

in

Engineering Sciences (Mechanical Engineering)

by

Chien-Wei Lee

Committee in charge:

Professor Vitali F. Nesterenko, Chair
Professor David J. Benson
Professor Prabhakar R. Bandaru
Professor Renkun Chen
Professor Yuri Bazilevs

2014

This Dissertation of Chien-Wei Lee is approved, and it is acceptable in quality and form for publication on microfilm and electronically:

Chair

University of California, San Diego

2014

Table of Contents

List of Figures

List of Tables

Acknowledgements

It is a pleasure to thank those who made this thesis possible. I am heartily thankful to my supervisor, Dr. Vitali F. Nesterenko, whose encouragement; guidance and support from the initial to the final level enable me to develop an understanding of the subject. I also would like to thank the members of my dissertation committee, Dr. David Benson, Dr. Bandaru Prabhakar, Dr Renkun Chen and Dr. Yuri Bazilevs, for their comments and suggestions.

Chapter 2 contains part of the material published in the paper "Dynamic Deformation of Strongly Nonlinear Toroidal Rubber Elements" in Journal of Applied Physics 2013. The dissertation author was the primary investigator and author of this paper.

Chapter 3 contains part of the material published in the paper "Dynamic Deformation of Strongly Nonlinear Toroidal Rubber Elements" in Journal of Applied Physics 2013. The dissertation author was the primary investigator and author of this paper.

Chapter 4 contains part of the material of a submitted paper "Path Dependent High Strain, Strain-Rate, Deformation of Polymer o-rings" in Journal of Applied Physics. The dissertation author was the primary investigator and author of this paper.

Chapter 5 contains material currently being prepared for publication of "Soft drop weight tests of low strength materials." The dissertation author was the primary investigator and author of this material.

Chapter 6 contains part of materials in the paper "Characterization of the Blast Simulator Elastomer Material Using a Pseudo-Elastic Rubber Model" in International

Journal of Impact Engineering and in paper “Roles of Material Properties and Mesostructure on Dynamic Deformation and Shear Instability in Al-W Granular Composites” in Journal of Applied Physics. The dissertation author conducted experiments and obtained results on Adiprene L-100 and Al/W sample using soft drop weight tests. Chapter 6 contains material currently being prepared for publication of “Soft drop weight tests of low strength materials.” The dissertation author was the primary investigator and author of this material.

I am grateful for the partial support of my research from ONR MURI N00014-07-1-0740 (Program Officer Dr. Clifford Bedford).

VITA

2007	Bachelor of Engineering, Mechanical Engineering National Taiwan University, Taipei, Taiwan
2010	Master of Engineering, Mechanical and Aerospace Engineering University of California San Diego, San Diego, USA
2014	Doctor of Philosophy, Engineering Sciences (Mechanical Engineering) University of California San Diego, San Diego, USA

PUBLICATIONS

Chien-Wei Lee, Vitali F. Nesterenko (2014), Soft drop weight tests of low strength materials (in preparation).

Chien-Wei Lee, Vitali F. Nesterenko (2014), Path dependent high strain, strain-rate deformation of polymer toroidal elements, Journal of Applied Physics, (Submitted).

Chien-Wei Lee, Vitali F. Nesterenko (2013), Dynamic Deformation of Strongly Nonlinear Toroidal Rubber Elements, Journal of Applied Physics, 114(8), 083509.

Aaron Freidenberg, Chien-Wei Lee, B. Durant, Vitali. F. Nesterenko, L. K. Stewart, and G. A. Hegmier (2013), Characterization of the Blast Simulator Elastomer Material Using a Pseudo-Elastic Rubber Model, International Journal of Impact Engineering, 60, 58-66.

Karl L. Olney, P. H. Chiu, Chien-Wei Lee, Vitali F. Nesterenko, and D. J. Benson (2011), Role of Material Properties and Mesostructure on Dynamic Deformation and Shear Instability in Al-W Granular Composites, Journal of Applied Physics, 110(11), 114908.

REFEREED CONFERENCE PROCEEDINGS

Po-Hsun Chiu, Chien-Wei Lee, Vitali F. Nesterenko (2012), Processing and dynamic testing of Al/W granular composites, AIP Conference Proceedings, 1426, 737.

CONFERENCE PRESENTATIONS

Chien-Wei Lee, Vitali F. Nesterenko, "High Strain Rate, Path Dependent Deformation of Polymer O-rigs" 16th International Conference on Experimental Mechanics, July 7-11, 2014, Cambridge, UK (Paper is accepted for presentation).

Field of Study

Major Field: Engineering Sciences (Mechanical Engineering)

ABSTRACT OF THE DISSERTATION

Dynamic Testing and Properties of Rubber O-rings and Their Application in Soft Drop Weight Tests of Low Strength Materials

by

Chien-Wei Lee

Doctor of Philosophy in Engineering Sciences (Mechanical Engineering)

University of California, San Diego, 2014

Professor Vitali F. Nesterenko, Chair

Mechanical behavior of low strength materials and elements at high strain rates was studied using a drop tower at UCSD. A commercial drop tower was modified to conduct high strain-rate impact compression tests. Instrumentations including strain

gauges, accelerometers and a high speed camera were used to establish equilibrium conditions and stress strain relation of samples with high accuracy.

Dynamic response of strongly nonlinear, viscoelastic toroidal rubber elements (o-rings) is studied. Nonlinear dynamic model using strain-rate dependence initially proposed for contact of spherical particles by Brilliantov et. all, and Morgado et. all is modified for strongly nonlinear viscoelastic behavior of o-ring. The model successfully describes the dramatic difference between static and dynamic behavior of o-ring being consistent with measurements in high strain rate experiments.

Weaker than linear strain-rate dependence is observed when impact velocity increased. A modified model with power-law strain-rate dependence is proposed based on experimental results. It satisfactory describes the results in a whole range of strain and strain-rates corresponding to different velocities of impact.

The testing results of pre-compressed o-rings demonstrated a smaller force at similar strains in comparison with o-rings without pre-compression. At the same time, the slope of force-strain curve demonstrated a higher rigidity for precompressed o-rings. It also was observed that deformation of o-rings exhibited strong memory effect in precompressed state. This behavior of pre-compressed o-rings was explained using a model considering memory effect as a function of initial pre-compression. The model explained the observation from experiment that pre-compression of o-rings contribute to dynamic stiffness which exhibits a stiffer behavior in the initial stage of deformation.

The investigated properties of o-rings were used to develop soft drop weight tests eliminating high amplitude noise generic for experimental setup. The results of soft drop weight tests were verified by testing Al samples, whose the mechanical properties are

well known. High strain–rate stress versus strain relations of Al 6061-T6 and Al 6061-0 were measured using soft drop weight tests and the results are in agreement with data reported in previous literatures using Hopkinson Split Pressure Bar under similar strain rates.

The soft drop weight test was also used to obtain parameters for material model of Adiprene L-100 used in UCSD blast simulator. The loading and unloading curves of Adiprene L-100 under different strain-rates were measured and successfully used to generate tabulated date for elastomer material model used to optimize dynamic load of UCSD blast simulator.

Stress strain relations of Al-W composites were measured using soft drop weight tests. It was found that deformation mechanisms and mechanical properties of the composites were significantly different for samples with different mesostructure corresponding to different processing routes.

CHAPTER 1

STATE OF THE ART IN DYNAMIC DEFORMATION OF LOW STRENGTH MATERIALS

1.1 Introduction of the thesis

Mechanical behavior at high strain rates differs considerably from that observed at quasi-static or intermediate strain rates, and many engineering applications require characterization of mechanical behavior under dynamic condition. For example, strain rates ranging from 100 s^{-1} to more than 10^4 s^{-1} occur in many processes or events of practical importance, such as structural impacts, earthquakes, blast loading, foreign object damage, and metal working.

High strain-rates testing can be executed using drop weight tests. In conventional drop weight tests, high frequency noises excited from the impact between the drop mass and the target is unavoidable and high amplitude noise is always recoded by strain gauges signals in all published papers. For example, Figure 1-1 demonstrates the noisy signal recording in a conventional impact test conducted in Cavendish Laboratory, Cambridge [1]. It is evident that significant noise level masks the real signals. In order to improve the signal quality of conventional drop weight tests, a “soft” drop weight test is proposed by introducing an extra layer of “soft” elements (e.g., rubber pads or o-rings) as force profiler. From the results, we showed the quality of the signals from load cells or accelerometers significant improved in comparison with conventional drop weigh tests.

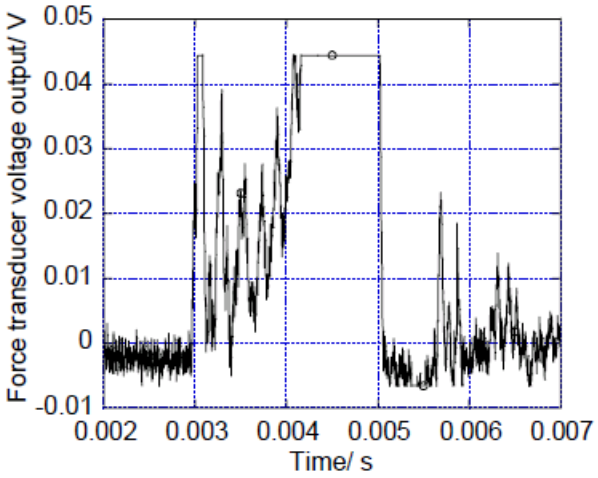

Figure 1-1 Noisy data recorded in a conventional drop-weight test. [1]

Toroidal elements (o-rings) are widely used in hydraulic and pneumatic equipments in sealing of drive shafts, pistons and lids and their static elastic properties are well studied. O-rings are also broadly used in applications as shock absorbers, but dynamic properties of these elements are not studied as extensively as their static behavior. Dynamic properties of o-rings are studied using experimental approach in this research. The existing models of behavior of o-rings were analyzed and it was demonstrated they can't explain experimental results. The proposed dynamic model of o-ring is successfully used to predict change of o-ring height as a function of force during soft drop weight tests.

Chapter 2 introduced a modified drop tower for high strain rate testing and corresponding instrumentations. An Instron 9250HV drop tower was modified by adding a bottom anvil supported using a hydraulic jack. It can be configured for the dynamic tests of single or multiple o-rings, pre-compressed o-rings, and soft drop weight tests of low strength materials. Forces were measured utilizing strain gauges and accelerometers. Signal processing using analog and digital filters was applied on strain

gauges measurement. Force equilibrium of samples during impact tests was experimentally proven. Deforming images of the sample were recorded by a high speed camera and an image tracking algorithm was designed to retrieve displacement versus time. The dynamic model of the supporting structure was analyzed and the strains in the samples can be estimated from force measurements.

Chapter 3 analyzed the dynamic properties of o-ring using drop weight tests. Quasi-static experiment was performed to measure steady state elastic modulus. Deformation of Buna-N o-ring was recorded by a high speed camera and displacement over time was calculated using image tracking algorithm with accuracy up to single pixel size. Force measurement from strain gauges was used to derive acceleration, velocity, and displacement of the drop mass. The results were independently verified utilizing optical images. Change of o-ring height was derived from strain gauges measurement with a correction from optical images for displacements of the supporting structure. Dynamic force over engineering strain of o-ring was evaluated from the measurement. Dynamic model with linear strain-rate dependence failed to explain experimental measurement indicating that nonlinearity must be considered. The approach proposed by Brilliantov et. all [2] and Morgado et. all [3] was modified for the modeling of non-linear strain-rate dependence of force applied to o-rings. The modified model is in agreement with experiments under impact velocity of 1 m/s.

Chapter 4 explored other dynamic models of o-ring deformation for a wider velocity range and precompression effect. Experimental results from impact tests using higher impact velocity showed weaker than linear strain-rate effect. Hertz-damp model was modified for dynamic behavior of o-rings. It was found that this model

underestimated the dynamic force and couldn't explain significant deviation from the static curve. The proposed modified model using power-law or logarithm strain-rates dependence successfully explained experimental results in the investigated range of strains and strain-rates. Path dependent deformation of o-rings with different levels of pre-compression was investigated under dynamic loading conditions. It was found that dynamic response of pre-compressed o-rings at the initial strain range 0.04-0.25 is similar to the behavior of uncompressed o-rings, but further increase of pre-compression to 0.4 and 0.5 results in different force-strain curves demonstrating a memory effect. This phenomena was explained using a model incorporating dependence of dynamic force on initial pre-compression introducing critical level of dynamic strain after which memory of initial pre-compression fades. This model predicts that *force history of weakly compressed o-ring (initial strain 4%) on the stage of loading is an envelope for all other data in agreement with experiments*. In all cases the dynamic behavior was characterized by stiffer force-displacement curves in comparison with quasistatic compression of o-ring.

Chapter 5 demonstrated soft drop weight tests using o-rings to reduce noise in force records. Stress data of the sample was obtained from force recorded by strain gauges. With the help of a high speed camera, samples' strain history was derived from optical images with good accuracy. The results allow proposing the approach to derive strain history of the sample from force measurement without the usage of high speed recording. Change of sample's height corresponds to the relative displacement between lower and upper pistons. Displacement of the lower piston could be estimated from a mass-dashpot-spring model of base structure and measured force. Displacement of upper

piston was related to displacement of the drop mass and change of “softening” o-ring height. Displacement of the drop mass could be derived from force integration and change of o-ring height was solved using power law strain rate dependent model proposed in Chapter 4. Using an instrumented and calibrated drop tower, change of sample’s height during soft drop weight tests could be derived from force measurement.

Chapter 6 presented the applications of soft drop weight tests to measure high strain, strain –rate mechanical properties of Al, Adiprene L-100, and Al/W composites. Dynamic tests of Al 6061-T6 and Al 6061-0 were used to verify strain and stress measurement used in soft drop weight tests. The results were compared with data measured using Hopkinson Split Pressure Bar under similar strain rate and demonstrated similar stress strain relation.

Strain-rate sensitivity of polymer materials was investigated using soft drop weight tests. The loading and unloading curves of Adiprene L-100 under different strain-rates were measured using soft drop weight tests. The results were successfully used to generate tabulated date for the elastomer material model. Strain-rate related properties were required for Adiprene L-100, which is an important component of the UCSD Blast Simulator to tailor impulsive load. The obtained data were used to construct the material model in LS-DYNA.

Mechanical properties of Al-W composites under high strain-rate were measured using soft drop weight tests. Testing results demonstrated the qualitative difference of Al-W composites with different mesostructure and processing routes.

Finally, Chapter 7 briefly outlines the summery of this research.

1.2 References

1. J. Addiss, J. Cai, S. M. Walley, W. G. Proud, and V. F. Nesterenko, (2007) "High stain and strain-rata behaviour of PTFE/aluminuim/tungsten mixtures" in shock compression of compression of condensed matter- 2007, Proceedings of the Conference of the American Physical Society Topical Group on Shock Compression of Condensed Matter, edited by M. Elert, M.D. Furnish, R. Chau, N. Holmes, and J. Nguyen (American Institute of Physics), pp. 773-776.

2. N. V. Brilliantov, F. Spahn, J.-M. Hertzsch and T. Poschel, (1996) "Model for collisions in granular gases." Physical review E 53, 5382.

3. W. Morgado, and I. Oppenheim, (1997) "Energy dissipation for quasielactic granular particle collisions." Physical Review E 55, 1940.

CHAPTER 2

EXPERIMENTAL TECHNIQUE FOR DROP WEIGHT TESTS

2.1 General Experimental Setup

General experimental setup is shown in Figure 2-1 and Figure 2-2 including an Instron Dynatup 9250HV drop tower, a Central Hydraulics 30 ton heavy duty industrial hydraulic bottle jack, a Phantom V12 high speed camera, an Ectron Model 778 amplifier, a Tektronix TDS2014 oscilloscope, a Columbia Research Lab piezoelectric accelerometer 8012 and corresponding signal conditioner, and the triggering device.

An Instron 9250HV drop tower was modified by adding a bottom anvil supported by a hydraulic jack (Central Hydraulic 30 ton) and can be configured for the testing of single or multiple o-rings, pre-compressed o-rings and soft drop weight tests. Drop mass assembly with adjustable weight can be raised to a specific height to provide designated impacting velocity and energy. Drop mass can vary from 2.7 kg to 28.9 kg and the maximum free fall height of drop tower is 1.25m. Design of Instron 9250HV is able to provide maximum spring assisted velocity of drop weight up to 20 m/s (depending on mass) and energy with mass 14.4 kg equal to 720J. A standard design of this impact test instrument has a velocimeter allowing measurements of velocity of drop mass just before its impact on the sample.

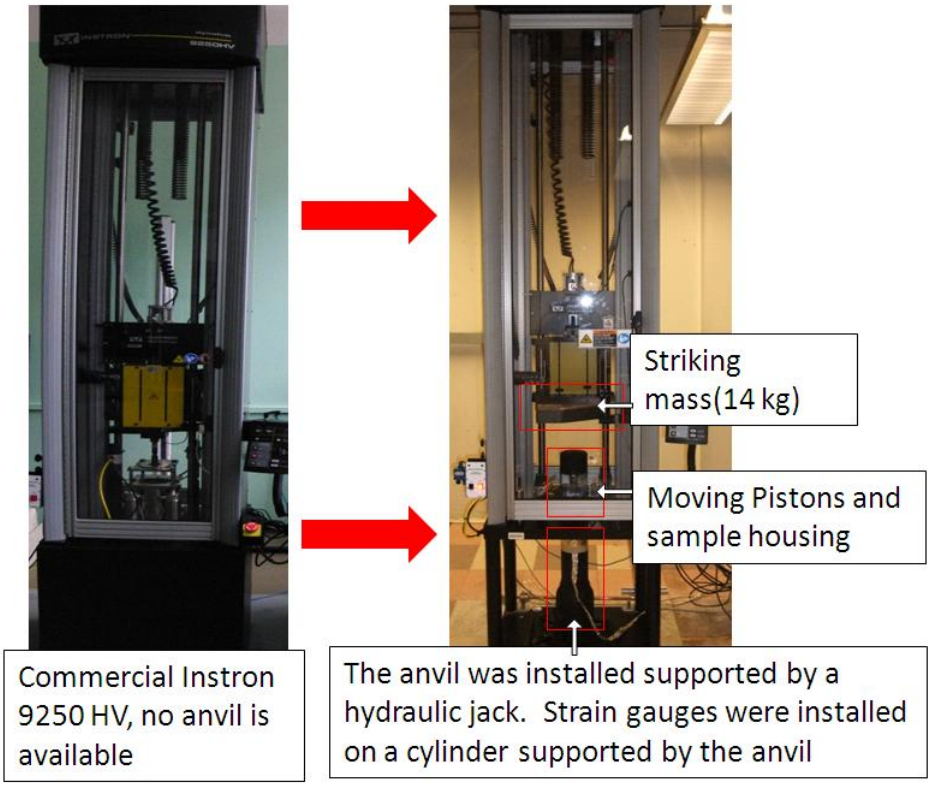

Figure 2-1 Modification on an Instron Dynatup 9250HV drop tower for high strains, high strain-rates compression dynamic tests.

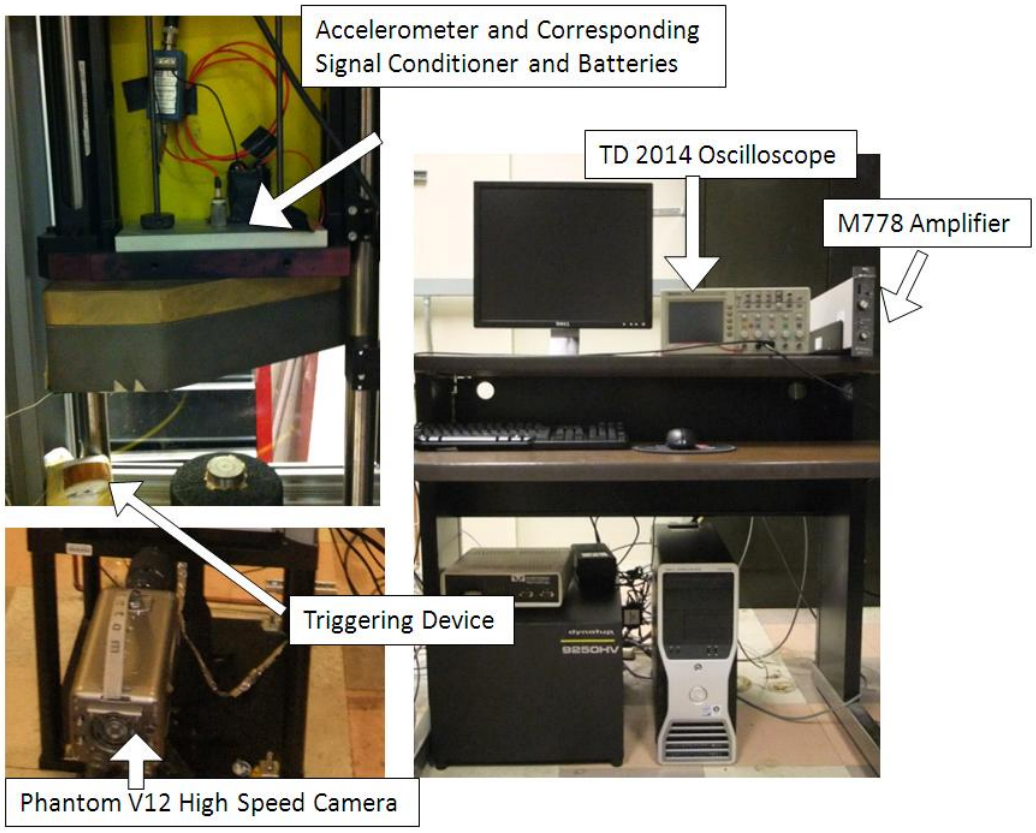

Figure 2-2 Instrumentation on Instron Dynatup 9250HV drop tower including a Phantom V12 high speed camera, an Ectron Model 778 amplifier, a Tektronix TDS2014 oscilloscope, a Columbia Research Lab piezoelectric accelerometer 8012 and corresponding Signal conditioner, and the triggering device.

Images of deformed samples during impact tests were captured by Phantom V12 high-speed camera. This camera can provide 6242 frames-per-second at full 1280X800 widescreen resolution and 10^6 frames-per-second at reduced resolution and does not require synchronization unless it is necessary. Sub-microsecond exposure time can be reduced down to 300 ns. Sigma 105mm f/2.8 DG Macro lens was used with maximum reproduction ratio of 1:1.

Two strain gauges are placed on opposite sides of a load cell to record dynamic strains in steel cylinder which can be translated to stress history of tested samples. Strain gauges are connected with two compatible resistances to form one full Wheatstone

bridge. The signals are processed by an Ectron M778 amplifier and recorded by a TD2014 oscilloscope. M778 signal conditioner/amplifier provides amplification gain up to 1000x with built in analog filter option of 300 kHz, 100 kHz, 10 kHz etc.

Piezoelectric accelerometers 8012 (Columbia Research Lab) and a corresponding signal conditioner and batteries are attached to the drop mass to measure the acceleration of drop mass in vertical direction. The accelerometer is a hexagonal prism with height 22.4 mm and weight 17gm. This sensor can measure acceleration within ±20,000g with voltage sensitivity of 0.25mv/g. The range of linear frequency response is between 2 Hz to 15 kHz with a maximum error of ±5%.

Piezoelectric accelerometers 8011 (Columbia Research Lab) was also used with smaller dynamic range and higher voltage sensitivity. This sensor can measure acceleration within ±5,000g with voltage sensitivity of 1.0 mv/g. The range of linear frequency response is between 2 Hz to 10 kHz with a maximum error of ±5%.

The triggering device for the oscilloscope and the high speed camera consists of two separated copper foils with applied voltage. It was set up next to the supporting column to detect the starting moment of the impact of drop mass on the o-ring and synchronize images of deformed o-rings with measured force. The contact of these foils generates a voltage pulse triggering the oscilloscope and high speed camera simultaneously. Two channels in the oscilloscope recorded both signals from the load cell and the accelerometer.

2.2 Configuration for Dynamic Testing of Single O-ring

The experimental setup can be configured for investigating high strain/strain-rate behavior of o-rings and a schematic presentation of force chain and gauges is shown in Figure 2-3. Our customized force chain includes three cylinders to support the sample and measure applied dynamic force. They are identified as the upper piston, the lower piston, and another piston with strain gauges – the load cell. They are made of shock resisting tool steel (S7) and have a diameter of 31.7 mm with corresponding heights 153 mm, 124.7 mm, and 77.1 mm. Two 3mm thick steel disks are placed above and below the tested o-ring to improve accuracy in the images recorded by a high speed camera. This allows us to increase accuracy of strain measurement in comparison with approach used in [1].

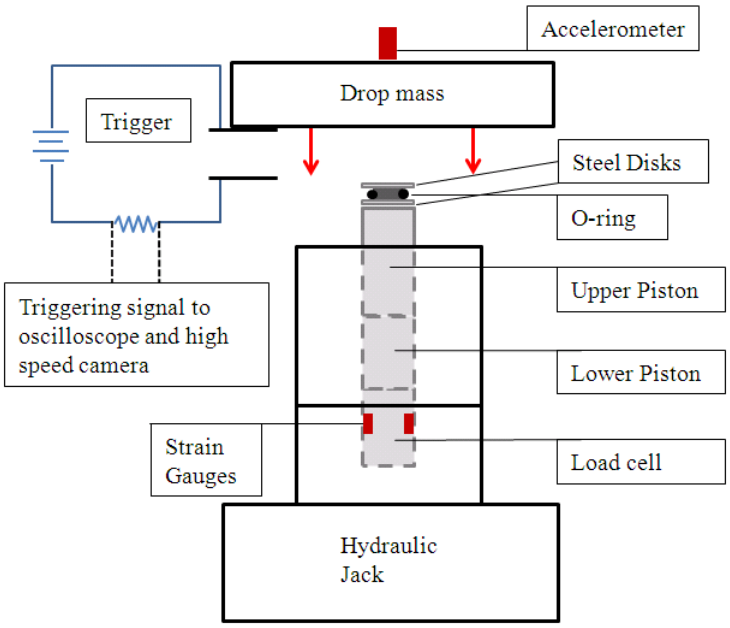

Figure 2-3 Schematic experimental set up and force chain in dynamic tests of single o-ring.

In this investigation of high strain/strain-rate behavior of o-rings we employed a modified Instron drop tower 9250HV as discussed in Chapter 2-1. A high speed camera Phantom V12 with a frame rate 40,000 fps is used to capture images of deformed o-rings and the video of deformation is used to derive the strain history. The load cell with strain gauges recorded dynamic force acting beneath the o-ring. An accelerometer was mounted on the drop mass assembly to measure the force acting on the top of the o-ring. Force equilibrium in o-rings is presented in Chapter 3. The accuracy of force measurement is determined by analog to digital resolution of the oscilloscope, which is 4mV, corresponding to 80 N in force.

2.3 Configuration for Dynamic Testing of Pre-Compressed O-rings

The tests of pre-compressed o-ring can be done by replacing the upper piston by a special holder as shown in Figure 2-4. The special holder can provide a desired level of pre-compression on samples by four steps shown in Figure 2-5. In the figure four o-rings are assembled to deform in similar conditions increasing accuracy of measurements. It present a cartoon of preparing 10 % pre-compressed 4 Buna-N o-rings (initial outer diameter D = 20mm, mean diameter Dm = 15mm, and diameter of circular cross section, d = 5mm) separated by 5 stainless steel disks (width 3mm).

Step 1: Use 11 disks to set the exact position of nuts A at 33 mm corresponding to the height of the stack of metal plates.

Step 2: Remove the nuts B and upper holder and place periodic assemble of o-rings and metal plates along the center of the holder.

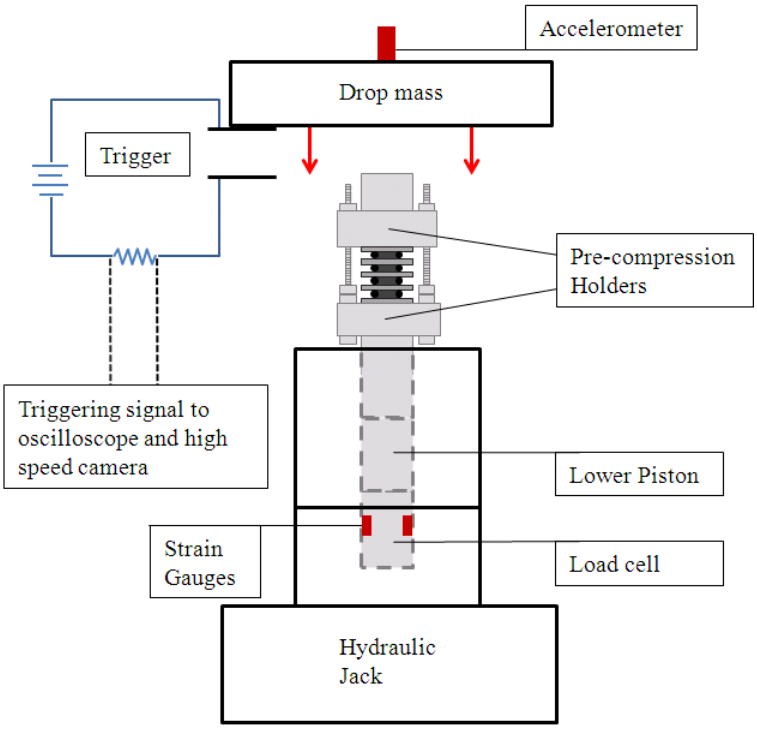

Figure 2-4 Schematic experimental set up and force chain in dynamic tests of pre-compressed o-rings.

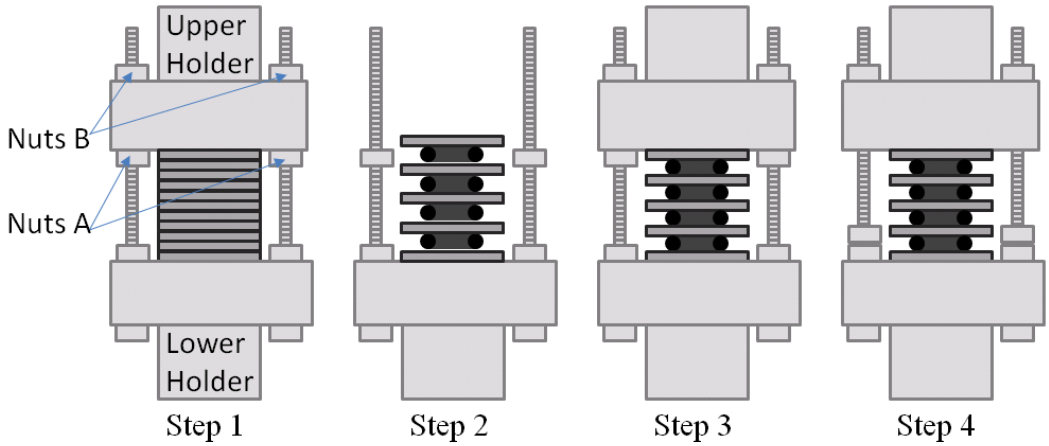

Figure 2-5 Special holders used to provide accurate pre-compression of o-rings. A cartoon shows 4 steps to provide 10% pre-compression of 4 Buna-N o-rings (initial outer diameter D = 20mm, mean diameter Dm = 15mm, diameter of circular cross section, d = 5mm).

Step 3: Tighten the upper holder using nuts B until it reaches the same height set by the nuts A in the Step 1.

Step 4: Screw down the nuts A so that the upper part of the holder can move freely during dynamic tests.

Polymer o-rings exhibit viscoelastic behavior under quasistatic loading with relaxation times. In order to perform tests with o-rings under similar initial conditions, a 3-minutes pre-compression time was maintained before each dynamic test. This is the same period of time used to determine the elastic constant of static double power law equation of Buna-N o-rings.

2.4 Configuration for Soft Drop Weight Tests

The experimental setup can be configured for soft drop weight tests of low strength samples. A schematic presentation of force chain and gauges are shown in Figure 2-6. The testing samples are placed between the upper and lower pistons. During soft drop weight tests o-rings on the top of the upper piston were used to ramp the impact force thus avoiding “parasitic” high amplitude oscillations [1-4]. All cylinders in the force chain are mounted inside supporting structure to avoid bending.

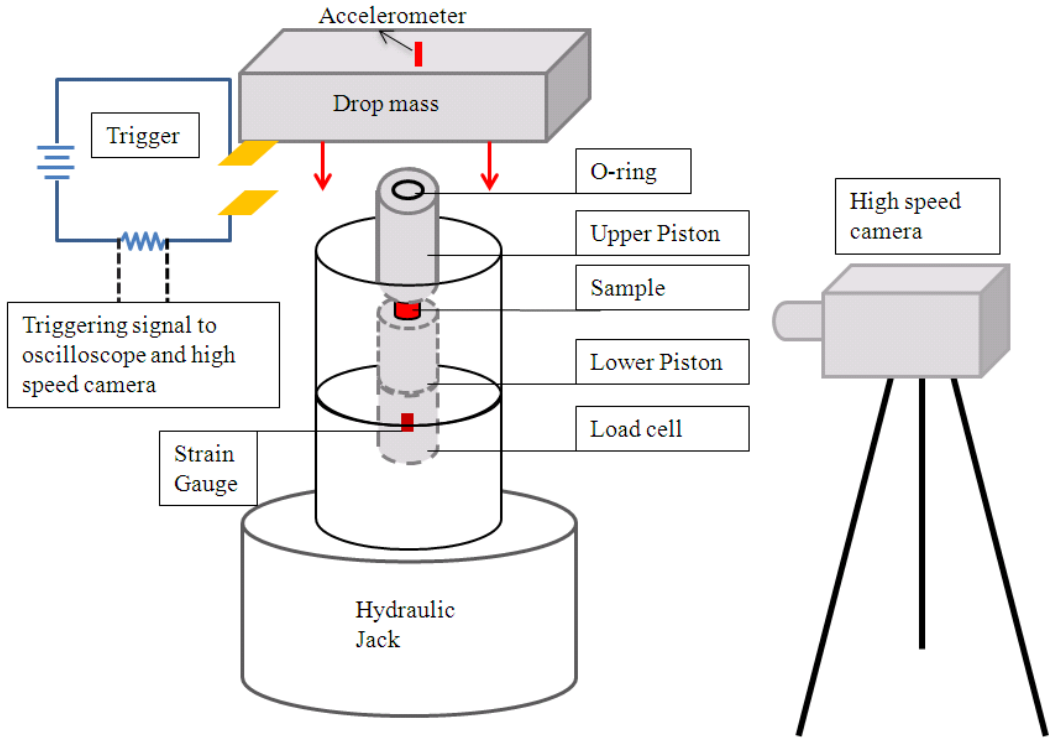

Figure 2-6 Schematic experimental set up and force chain in soft drop weight tests.

2.5 Force Measurement by the Strain Gauges and Accelerometers

Force acting on the bottom part of sample is monitored by the strain gauges in the load cell supporting samples. Voltage signal form a load cell was converted to force (F) acting on the sample using Equations (2.1), (2.2)

$$F = \frac{V}{G} K\ (N), \tag{2.1}$$

$$K = \frac{4EA}{GF \cdot V_{in}} = 2.1 \cdot 10^{7} \left({}^{N}/_{V}\right). \tag{2.2}$$

here V is the voltage signals recorded by the oscilloscope, G = 500 is the amplification factor set in the amplifier, and K is a calibration factor relating voltage output from strain gauges and force applied on the rod (sample). Here $E = 205 \cdot 10^{9}\ [Pa]$ is the Young's modulus of steel, $A = 7.89 \cdot 10^{-4}\ [m^2]$ is the cross section area of the load cell, strain

gauge factor $GF = 2.05$ is provided by the vender, and voltage input in the Wheatstone bridge is $V_{in} = 15V$. An example force history recorded by strain gauge in a dynamic test of o-ring is shown in Figure 2-7.

Signal presented in Figure 2-7 demonstrates force history during the impact testing of one Buna-N o-ring impacted by a drop mass with initial velocity 1.6 m/s. The signals are shifted in time, and t = 0 ms corresponds to the moment of force application to the sample. The force reached its maximum value 16 KN at 2.3 ms, and dropped back to zero at 4.8 ms. The force signals presented here are smoother and more repeatable comparing with noisy force history in traditional drop weight tests [5, 6] (compare Figure 2-7 with Figure 1-1). A minimum amount of analog low pass filtering with a cut-off frequency 300 kHz was applied using amplifier M778. Signal recording is improved due to nonlinear elastic character of "soft" o-ring to ramp the sharp increase in force and minimize the excitation of high frequency noises caused by vibrations of loading device and supporting structures. This behavior of o-rings was used to get smooth records of force in previous papers [2, 3]. No analysis of o-ring deformation was provided thus not allowing calculation of sample strains based on force records.

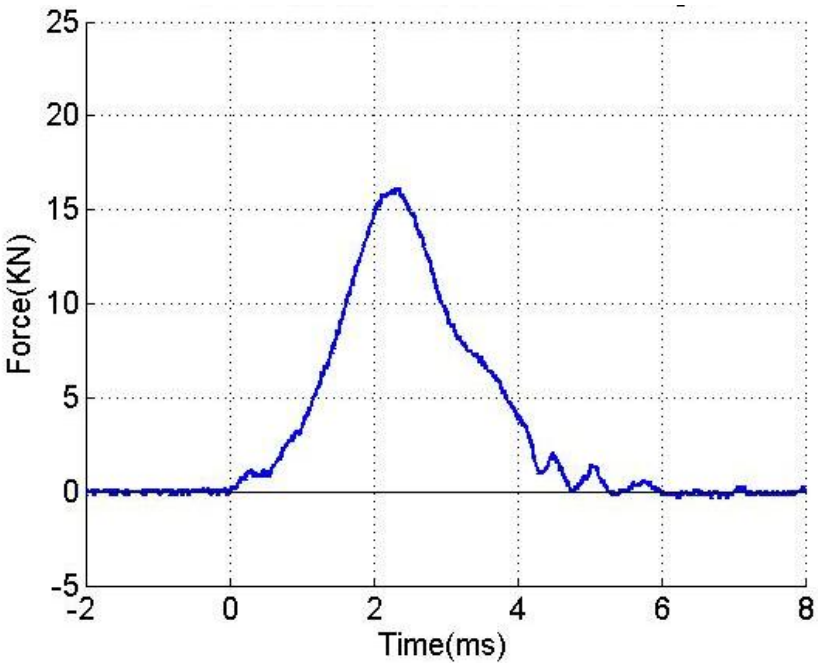

Figure 2-7 Force history of a Buna-N o-ring (initial outer diameter of o-ring D=20mm, mean diameter D_m =15mm, and diameter of circular cross section, d=5mm) recorded by strain gauges in the load cell. The drop mass had initial velocity 1.6m/s.

Piezoelectric accelerometer Model 8011 from Columbia Research lab was installed on the drop mass to record acceleration history, which can be related to the force acting on the top of the o-ring. The voltage data can be converted to the acceleration by using a calibration factor of 0.973 mv/g ±1% provided by the manufacturer. Acceleration data allows finding force acting on the top of the o-ring using Newton's second law (using the corresponding mass 15.4 kg, which includes the drop assembly, accelerometer, conditioner, and batteries). The force signal recorded by accelerometer during the same impact testing corresponding to Figure 2-7 (initial velocity of drop mass 1.6m/s on a 5mm Buna-N o-ring) is shown in Figure 2-8.

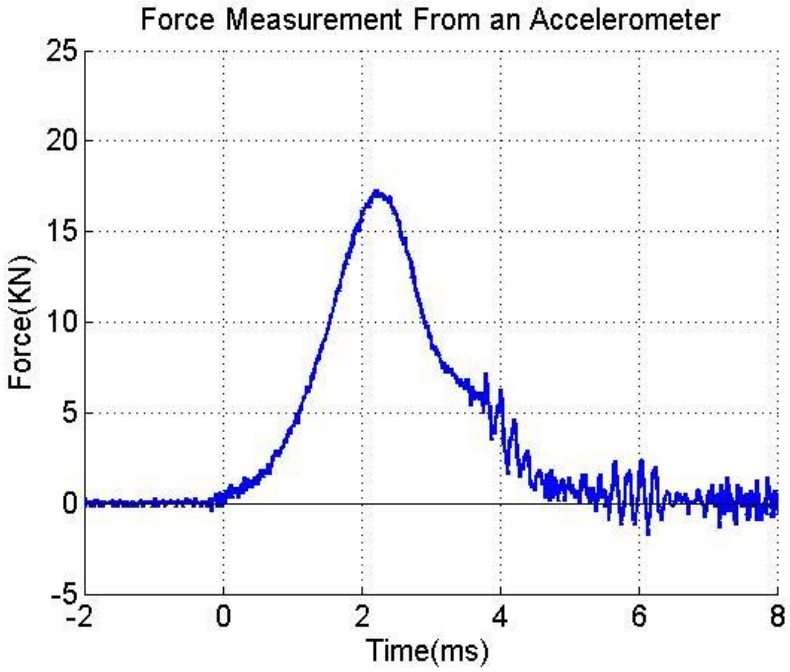

Figure 2-8 Force history of a Buna-N o-ring (initial outer diameter of o-ring D=20mm, mean diameter D_m =15mm, and diameter of circular cross section, d=5mm) recorded by an accelerometer. The drop mass had initial velocity 1.6m/s

Force acting on the top of the o-ring measured by an accelerometer is compared with the force acting on the bottom part of the o-ring obtained from the strain gauges in Figure 2-9. The results showed that these forces are almost the same demonstrating that force equilibrium was established during the dynamic test of o-rings.

Results of acceleration measurement allow finding velocity and displacement of drop mass using numerical integration. The acceleration data based on the force measurements by the load cell and the accelerometer are very similar to each other. However, the load cell data have less high frequency, low amplitude noise interference and in the following paragraphs they are used to calculate strain and strain-rate by integration.

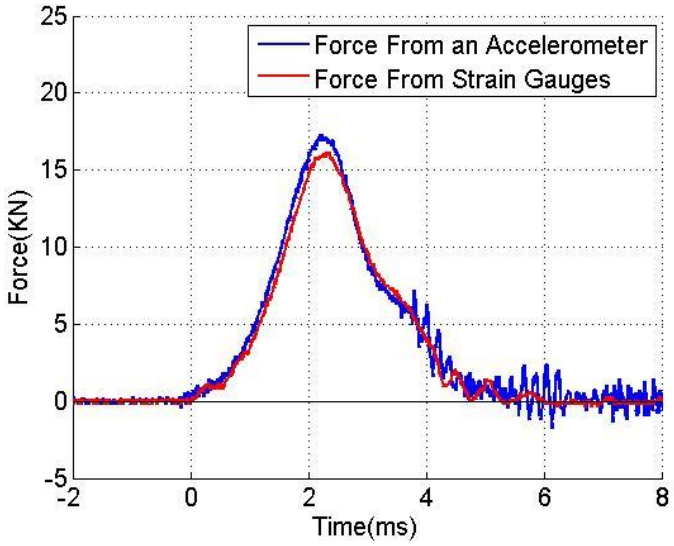

Figure 2-9 Comparing force data from an accelerometer and from the strain gauges corresponding to impact velocity 1.6m/s. The close similarity between the two measurements demonstrates force equilibrium during dynamic testing. Data correspond to Buna-N o-ring (initial outer diameter of o-ring D=20mm, mean diameter D_m =15mm, and diameter of circular cross section, d=5mm).

2.6 Signals Filtering

Analog low pass filters are embedded in Ectron Model 778 amplifier providing options to filter the input signals. In order to preserve the authenticity of dynamic force the analog filter option on the amplifier is set to 300 KHz for most measurement.

Numerical filters can be used to improve signals quality after the signals are recorded. Figure 2-8 demonstrates that unwanted high frequency, low amplitude components presented in the signals during the whole time, starting even before the impact thus indicating that this noise is not related to impact forces acting on the o-ring.

Two most used filtering techniques are discussed below: the central averaging filter and the ideal low-pass filter. The central average filter is an easiest filtering method to process the signals in time domain. For a 2N+1 term central average filter, the filtered signals are calculated by taking average of N terms before, the current term, and

N terms after. An ideal low-pass filter processes the signals in frequency domain by removing frequency components higher than the cutoff frequency.

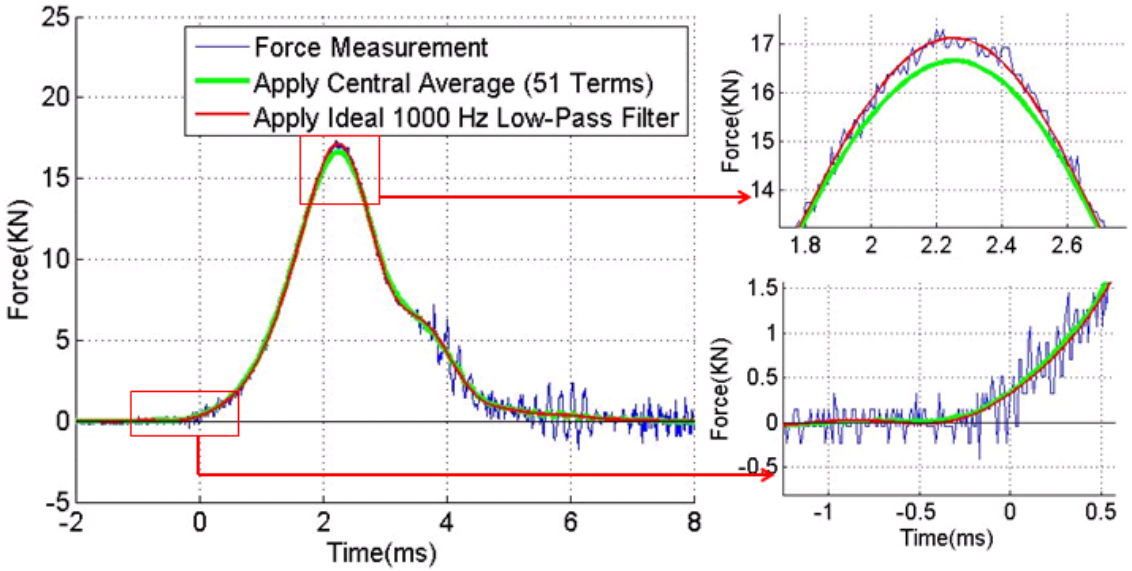

Figure 2-10 Force measurement from the accelerometer and the filtered results applying a central average filter (51 terms) and applying an ideal 1000Hz low-pass filter.

Figure 2-10 shows a comparison of filtered signals and original force signals recorded by accelerometers. The filtered signals are generated from original force measurement by applying a central average filter of 51 terms and an ideal low-pass filter with a cutoff frequency 1000 Hz. The plot on the left shows that the filtered results remain close to the original signals. The filters do not distort the force measurement. From the zoom-in views on the right, it's shown that both filters improve the smoothness of signal quality by removing white noise of ± 250 N. The ideal filter performs better regarding the interpretation in the vicinity of the top; on the other hand, central filter underestimate the curve by about 300 N. The ideal filter has better performance and is used for signal processing in the following chapters.

2.7 Images Tracking

A high speed camera is used to provide independent information on geometry of deformed samples. In most of the tests it's set to record videos with pixel number 512 X 256 at 40,000 fps, which equals to 25 μs between each frame. At this frame rate, 2.5 ms deforming history of the sample corresponds to 1000 images. Facing a large number of image data, an image tracking algorithm is developed to process the video and provide strain information with the best accuracy. The pixel size is affected by the distance from the lens of the high speed camera to the object and can go down to 0.05mm/pixel. Sigma 105mm f/2.8 DG Macro with minimum focus distance 0.41 m is used and the maximum reproduction ratio is 1:1.

A flow chart describing the algorithm to track the displacement of interested object involving the usage of MATLAB 2D correlation function is shown in Figure 2-11. Engineering strain history of a sample is derived from the relative displacements of the objects contacting the sample, above and beneath it. The calculation starts with loading a video recorded by a high speed camera into Matlab and process each image (*Image{i}*) one by one. A reference image ($Image_{ref}$), which is usually the first image of the video, is selected and the relative movement of the selected object in $Image_{ref}$ and *Image{i}* is calculated. In order to find the movement of the interested object, which can be a 3mm thick disk placed above or beneath the sample or a supporting piston in the drop weight test, the rectangular reference image is cropped ($Cropped_{ref}$) to contain desired features of the moving object. The calculation time in the following step using 2D correlation is related to the size of $Cropped_{ref}$. A larger cropped reference requires longer time in calculating 2D correlation. For example: with a cropped reference image of 20 X 40

pixels it takes 4.2 second to process 700 images, and with a cropped reference image of 160 X 40 pixels it takes 23.0 second to process the same number of images. We want to choose a $Cropped_{ref}$ as small as possible but contain enough features to track the object. The edges or specking patterns of objects are some of the most distinguishable features in the process of 2D correlation.

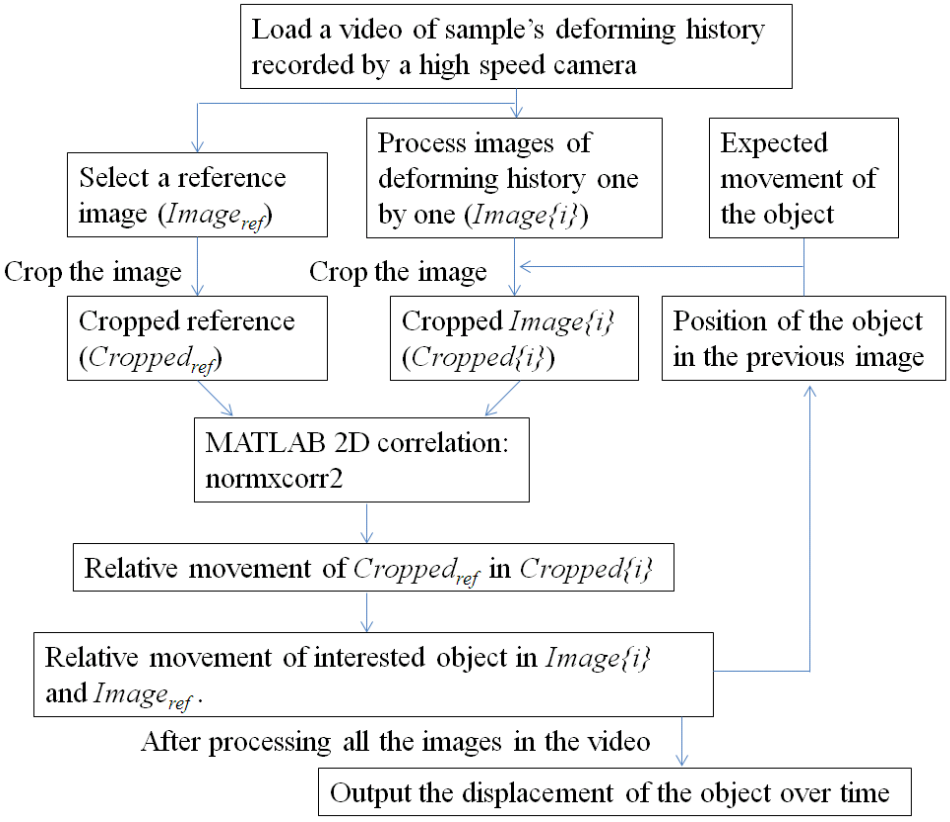

Figure 2-11 A flow chart demonstrating the algorithm used to track the displacement of dynamically deformed object using high speed images.

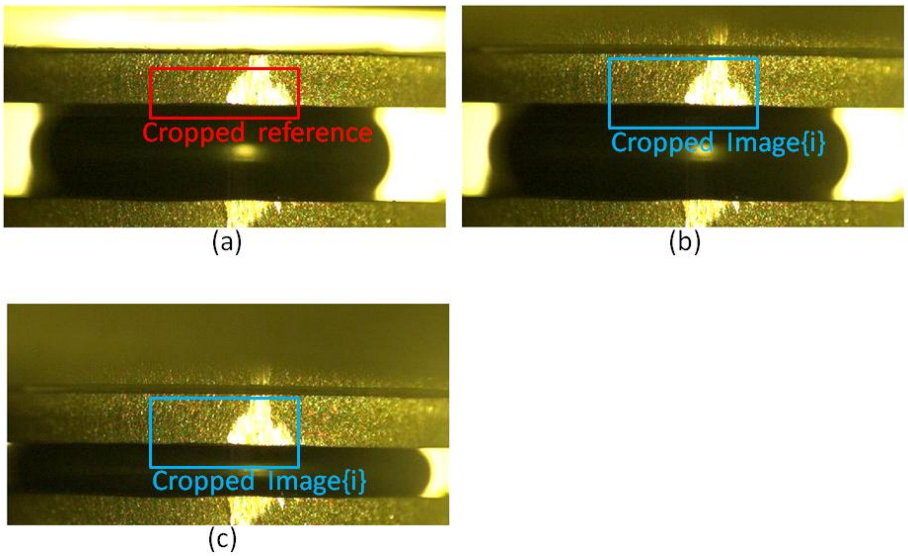

Figure 2-12 (a) Reference image and cropped reference (t=0 ms and i = 1) (b) Image of deforming history and cropped region (t=1.6 ms and i = 65) (c) Image of deforming history and cropped region (t=4.925 ms and i = 198). *i* is the number of the frames in high speed images.

Figure 2-12 (a) shows an example of $Image_{ref}$ and the region of $Cropped_{ref}$. during a dynamic test of a Buna-N o-ring with diameter of circular cross section 5mm and impact velocity V = 1.25m/s. Figure 2-12 (b) presents image of deformed sample and its corresponding cropped area (*Cropped{i}*). The following 2D correlation will search for $Cropped_{ref}$ in *Cropped{i}* . In order to get correct interpretation of movement, it's necessary to make sure *Cropped{i}* includes the objects in $Cropped_{ref}$. The region of *Cropped{i}* is determined by the expected displacement of the object and the position of the object in the previous image. For example: in the dynamic testing of an o-ring shown in Figure 2-12, it's known that the 3mm disk above the tested o-ring can only move in vertical direction and the displacement in horizontal direction is not noticeable. Knowing that, the size of *Cropped{i}* is set to be larger in vertical direction and has the same size in horizontal direction as $Cropped_{ref}$ as shown in Figure 2-12 (a),(b). The size of *Cropped{i}* also affects calculation time. For the case of tracking the 3mm disk

introduced here, it's set to be 3 pixels above the upper border and 3 pixels beneath the lower border and totally 6 pixels larger than $Cropped_{ref}$ in height. The position of *Cropped{i}* is also determined by the expected position of the object which can be found in the previous image as indicated in the flow chart. In Figure 2-12 (c), as the object moves down, it position base on a previous image and the region of *Cropped{i}* moves down accordingly.

Once $Cropped_{ref}$ and *Cropped{i}* are determined, MATLAB function 'normcorr2' is used to conduct 2D correlation. The relative movement of $Cropped_{ref}$ in *Cropped{i}* is determined by finding the maximum value in the correlation matrix. It is then translated into the relative displacement of interested object in $Image_{ref}$ and *Image{i},* which is a required information to process the next image. The processing loop continue until all the images in the video are processed and an example of displacement of the object versus time is shown in Figure 2-13. The interpreting result is smooth with no oscillation. It shows that from the recording and the image correlation algorithm the precision can reach one pixel size which is 47μm in the example. The image tracking combined with high speed recording accomplishes precise strain measurement.

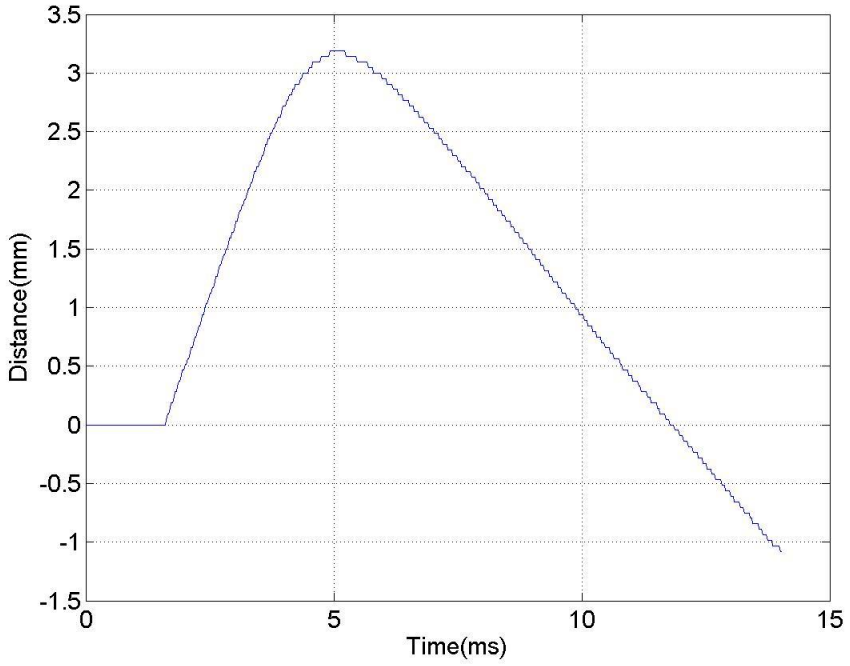

Figure 2-13 Displacement of the 3mm disk during an impact test of a 5mm cross section diameter o-ring derived from tracking optical images recorded by a high speed camera. V=1.25m/s.

Scaling is important for interpreting the distance in video recorded from a high speed camera. The depth of view would affect the scaling. Scaling images containing objects with fixed dimensions were taken before each test. An ideal case is only to track objects with the same depth of view at the distance where the scale of the object was determined. If multiple objects are on different depth of view, the distance needs to be calibrated by the following equation:

$$\boldsymbol{L_{cal} = L_o * \frac{D_o}{D_{cal}}} \qquad (2.3)$$

Where L_{cal} is calibrated length, L_o is length observed in optical images, D_{cal} is the object distance used for calibration, D_o is the object distance of the object. A calibration is

important for high reproduction ratio when D_{cal} is relatively small and slight difference between D_o and D_{cal} results to significant difference when interpreting the displacement of the object from optical images.

2.8 Displacements of Supporting Structure

During a soft drop weight test, the strain of the sample is determined by the relative displacement between the upper and lower piston. The lower piston sits on the supporting structure including a steel cylinder and a hydraulic jack which is not completely rigid and its small displacements can be observed by a high speed camera. A calibration test was executed to get the relationship between force and displacement of the supporting structure. The calibration test was a part of the dynamic deformation of o-ring using the configuration described in chapter 2-2. An o-ring was placed on the top of the upper piston and no samples were placed between upper and lower pistons. Figure 2-14 shows the relationship between force and displacement of the base.

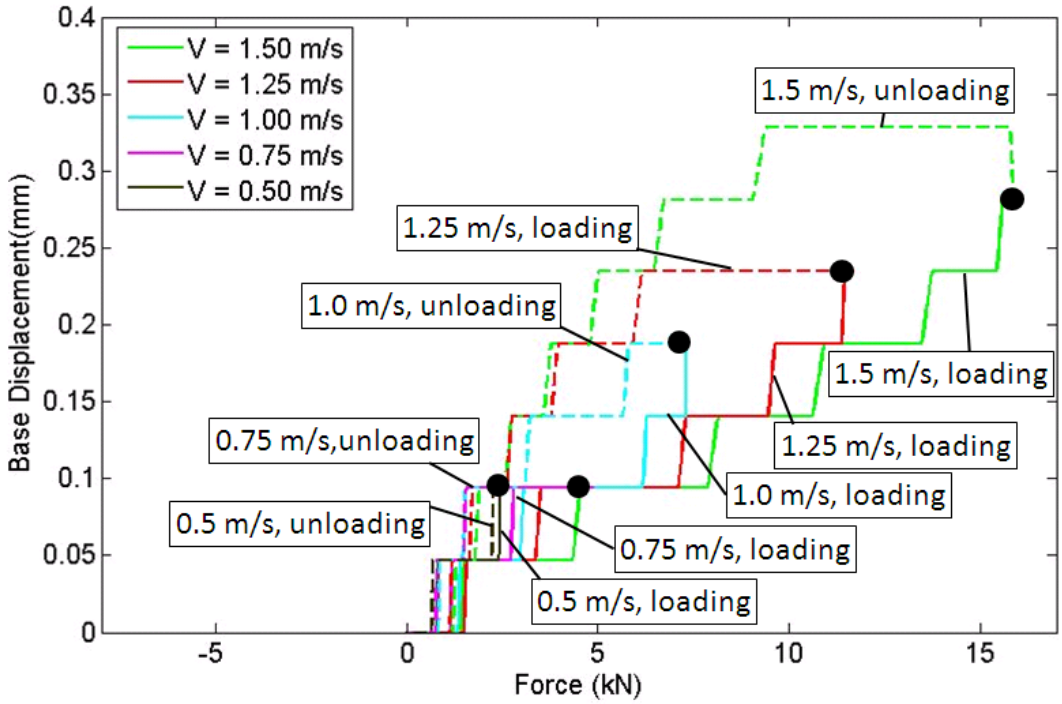

Figure 2-14 A relationship between force and displacement of the base during dynamic tests of 5mm cross section diameter o-rings under different impact velocities. Solid lines represent loading curves and dashed lines represent unloading curves. The dots on each curve correspond to the final stage of loading and beginning of unloading.

It's shown that displacement of the base is not a linear function of force. By comparing the loading(solid lines) and unloading(dash lines) curves it's found that at the same displacement of the base, the force on the loading curves is greater than the force on the unloading curves. This is the characteristic behavior of a linear Voigt model which composed of a spring and a damper in parallel.

The characteristic behavior of force versus displacement of supporting structure resembles behavior described by a linear Voigt model. Thus the movement of the supporting structure including a hydraulic jack and a lower piston subjects to force during impact tests is modeled as a mass-damper and spring system as shown in eq. (2.4)

$$M\ddot{x} + C\dot{x} + Kx = F(t) \qquad (2.4)$$

Where M is the effective mass of the supporting structure, C is the effective damping constant of the structure and K is the effective stiffness. Elastic behavior in quasistatic condition ($Kx = F(t)$) can be treated as a special case of eq.(2.4)

Base displacement is found using eq. 2.4 (Figure 2-15**)**, knowing that M = 13 [kg], and selecting C = 30 [kN·s/m], K = 45 [MN/m] and the force measured in impact tests, Solid lines represent experiment observation and dashed lines are numerical solution. It's shown that the modeling of supporting structure using a second order linear differential equation with linear viscosity matches with experimental measurement very well. The equation can be used for predicting the displacement of lower piston of drop weight test set up supporting the sample if high speed recording is not available.

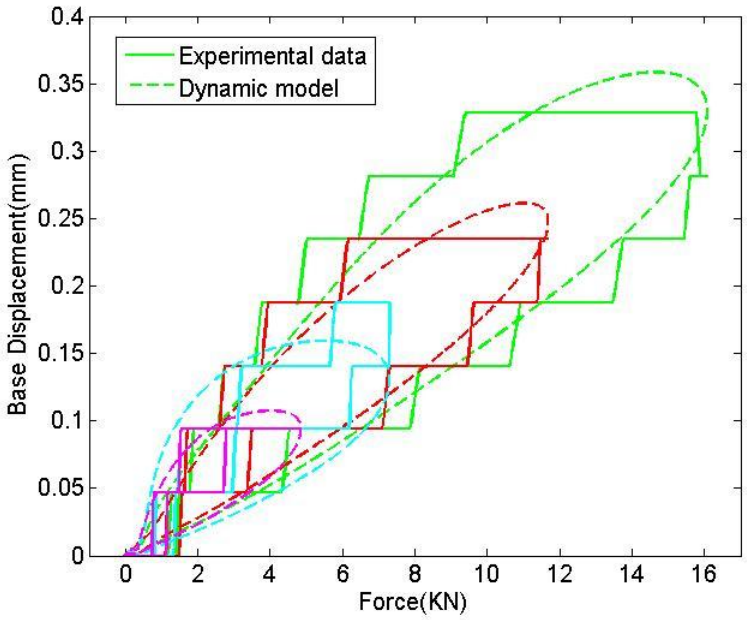

Figure 2-15 A relationship between force and displacement of the base during dynamic tests of 5mm cross section diameter o-rings under different impact velocities. Solid lines represent experimental observations and dashed lines are results of the numerical simulations.

2.9 Compressive Strain and Stress for Cylindrical Samples

The force measurement and change of sample's length are used to calculate engineering stress (σ_E) and engineering strain (ε_E) using eq. (2.5) and (2.6)

$$\sigma_E = \frac{F}{A_0} \tag{2.5}$$

$$\varepsilon_E = \frac{\Delta L}{L_0} = \frac{L_i - L_0}{L_0} \tag{2.6}$$

where F is applied load, A_0 is the initial sample cross-sectional area, ΔL is the change in length, L_i is the instantaneous sample length, and L_0 is the initial sample length. This analysis facilitates the comparison of results when testing samples have different thickness or geometry. Although these engineering values are adequate, the better measures of response of a material to loading are the true stress (σ_T) and true strain (ε_T) determined by the instantaneous dimensions of the specimen as shown in eq. (2.7) and (2.8):

$$\sigma_T = \frac{F}{A_i} = \sigma_E(1 + \varepsilon_E) \tag{2.7}$$

$$\varepsilon_T = \ln\left(\frac{L_i}{L_0}\right) = \ln(1 + \varepsilon_E) \tag{2.8}$$

Because the instantaneous dimensions of the specimen are not typically measured, the true stress and true strain may be estimated using the engineering stress and engineering strain (see eq. (2.5) and (2.6)). It is noted that these estimation are only valid during uniform compression and provides an estimation throughout the entire deformation range.

During compressive deformation, convention engineering strains and stresses are

negative. We present the data in a form of magnitude of compressive engineering strain versus the magnitude of compressive stress.

Chapter 2 contains part of the material published in the paper Dynamic Deformation of Strongly Nonlinear Toroidal Rubber Elements in Journal of Applied Physics 2013. The dissertation author was the primary investigator and author of this paper.

2.10 References

1. Chien-Wei Lee, and Vitali F. Nesterenko, (2013) "Dynamic deformation of strongly nonlinear toroidal rubber elements." Journal of Applied Physics 114.8: 083509.

2. J. Addiss, J. Cai, S. M. Walley, W. G. Proud, and V. F. Nesterenko, (2007) "High stain and strain-rata behaviour of PTFE/aluminuim/tungsten mixtures" in shock compression of compression of condensed matter- 2007, Proceedings of the Conference of the American Physical Society Topical Group on Shock Compression of Condensed Matter, edited by M. Elert, M.D. Furnish, R. Chau, N. Holmes, and J. Nguyen (American Institute of Physics), pp. 773-776.

3. E. B. Herbold, V. F. Nesterenko, D. J. Benson, J. Cai, K. S. Vecchio, and F. Jiang. (2008) "Particle size effect on strength, failure, and shock behavior in polytetrafluoroethylene-Al-W granular composite materials." Journal of Applied Physics 104.10: 103903.

4. K. L. Olney, P. H. Chiu, C. W. Lee, V. F. Nesterenko, and D. J. Benson, (2011) "Role of material properties and mesostructure on dynamic deformation and shear instability in Al-W granular composites." Journal of Applied Physics 110.11: 114908.

5. S. M. Walley, D. J. Chapman, D. M. Williamson, M. J. Morley, T. W. Fairhead, and W. Proud, (2009) "High rate mechanical properties of Dyneema in compression." Proceedings of DYMAT, 1133.

6. W. G. Proud, D. Porter, P. J. Gould, D. M. Williamson and S. M. Walley, (2010) "The Mechanical Performance of Polymers and Polymer Composites." in Proceedings of IMPLAST 2010 conference, Rhode Island, USA, October 12-14 2010, Society for Experimental Mechanics, Inc.

CHAPTER 3

DYNAMIC DEFORMATION OF STRONGLY NONLINEAR VISCOELASTIC TOROIDAL ELEMENTS

3.1 Introduction

Toroidal elements (o-rings) are widely used in hydraulic and pneumatic equipments in sealing of drive shafts, pistons and lids and their static elastic properties are well studied [1,2]. O-rings are also broadly used in applications as shock absorbers, but dynamic properties of these elements are not studied as extensively as their static behavior, though data on dynamic behavior of o-ring material (e.g. rubber) are available [3]. The characteristic highly non-linear elastic behavior of o-rings comes from geometry changes during deformation (initial circular shape of cross section) and also from nonlinear behavior of the elastomer under high strain deformation [4]. This property makes them one of the preferred elements to assemble strongly nonlinear double power law low dimensional metamaterials [5-6] which are more tunable than chains composed from spherical particles. These metamaterials can be used for attenuation of pulses caused by impact or explosion [8,9]. In these papers a double power law quasistaic stress-strain equation was used to approximate nonlinear dynamic behavior of o-ring on stage of loading and unloading. Though dissipation resulting in wave attenuation in experiments was very noticeable, it was not analyzed. O-rings have dissipative properties which are also presumably non-linear with respect to strain and

strain rate and exhibit hysteresis due to viscoelastic nature of elastomers.

In dynamic testing (e.g. drop weight tests) high frequency noise resulting from excitation of the testing machine is unavoidable and signals from strain gauges are always masked by high amplitude noise [5,6]. Usually unwanted noise signals are eliminated by using a low-pass filter before or after signal recording [12,13]. This is appropriate procedure if the noise characteristic period can be separated from characteristic time of useful signal. However, if a signal itself has high-frequency components, it will be improper to introduce any low pass filter cutoff frequencies for signals of similar magnitude. For example, in impact testing the characteristic time is about 100 μs which implies characteristic frequency of 10 kHz [12]. It may mask some details of sample's behavior if a low-pass filter with cutoff frequency 10 kHz or lower is applied to the signal.

The unwanted excitations can be also reduced by tailoring force profile applied to the sample. This can be accomplished by introducing some "soft" elements (e.g., rubber pads or o-rings) in the design of impact test resulting in desired ramping of loading force [4] and also avoiding noise excitation. This approach was successfully used in developing "soft" drop weight tests of low strength samples of reactive materials [14,15] and it is currently used for dynamic testing of Al-W composites [16]. The deformation of "soft" o-rings ramp the force applied to the sample reducing the excitation of high frequency components following abrupt change in signal during impact. The result is a significant improvement in the quality of records from load cells or accelerometers in comparison with conventional drop weigh tests [10,17,18]. From this prospective the dynamic properties of o-rings is of great interests in order to design desirable force

profile to perform high strain deformation testing of low strength samples (e.g., granular reactive materials) under strain rate in the order of 10^2 to 10^3 /s.

In both applications (design of impact mitigating metamaterials or “soft” impact testing) it is desirable to know dynamic strongly nonlinear and dissipative properties of toroidal elements. The dynamic behavior of toroidal o-rings at high strain, strain rate deformation is presented in this chapter.

Two independent instruments were used to record both forces acting on the top and bottom of toroidal element: one is an accelerometer mounted on the drop mass and another one was strain gauges placed in the supporting anvil beneath samples. The comparison between the two data was used to validate the assumption of force equilibrium in the sample under dynamic conditions. Additionally, the deformation of o-rings was monitored using a high speed camera allowing synchronized and independent record of engineering strain with measurements of force and acceleration.

It was shown that dynamic and static responses of o-rings are significantly different. The experimental force-time data, initial and recoil velocities of the impacter allowed us to evaluate dissipative properties of o-rings which can be used to improve the testing of low strength samples of granular reactive materials and in the design of low dimensional, energy absorbing and dispersive metamaterials. The same technique can be applied to study any strain-rate dependent deformation of low strength materials, e.g., low strength granular composites [19].

3.2 Experimental Setup

In this investigation of high strain/strain-rate behavior of o-rings we used the

configuration as discussed in Chapter 2-3. The impact tests are executed using a modified Instron 9250HV drop tower. The force data is translated from strain gauges recording and strain data is derived from optical images. This chapter presents results of the dynamic tests of two Buna-N rubber o-rings (McMaster-CARR, durometer hardness A70, ASTM D2000/SAE J00 standard) with diameter of circular cross section, *d* equals to 5 mm and 3mm, outer diameters *D* equals to 20 mm and 17mm, mean diameters D_m equals to 15mm and 14mm correspondingly. It is impacted by a drop assembly with a mass 14.4kg and velocities 1.04 m/s and 0.6m/s.

In order to avoid Mullin's effect [20] (softening behavior of rubber during the first couple of load cycles) the o-rings were impacted with the same velocity several times before the main test with recorded parameters of loading and unloading. No residual deformation was observed with accuracy up to 0.1 mm for any of tests.

3.3 Static Equation of Buna-N O-rings

Static compressive tests were performed with Buna-N o-rings to determine their elastic modulus. Their behavior (Figure 3-1) follows eq. (3.1) proposed by Lindley [1,2].

$$F = \pi D_m d E_0 \left[1.25 \left(\frac{x}{d}\right)^{1.5} + 50 \left(\frac{x}{d}\right)^{6}\right] \qquad (3.1)$$

where F is the compression force, D_m is a mean diameter and d is a diameter of circular cross section, and x is the change of o-ring height (initial height equals d) which is considered as having only positive values. E_0 is the elastic modulus which is equal 7.6 MPa from our data. Eq. (3.1) demonstrates strongly nonlinear, double power law force-deflection relation for an o-ring. Lindley[1] derived the first term analytically assuming

plane strain conditions, and added the second term as an empirical correction to accommodate behavior under higher strains [2]. Nonlinear static stiffness (K_s) can be derived from taking partial derivative of *F* with respect to *x* and is shown in eq. (3.2).

$$K_s = \frac{\partial F}{\partial x} = \pi D_m E_0 \left[1.875 \left(\frac{x}{d}\right)^{0.5} + 300 \left(\frac{x}{d}\right)^{5}\right] \qquad (3.2)$$

This nonlinear static stiffness is accounted in the design of o-rings. The deformation of o-rings may also be affected by viscoelastic behavior in dynamic conditions of loading. Videos of deformation were captured to observe how o-rings react to applied quasistatic force with time. Figure 3-1 shows how o-rings react to a quasistatic force as time of load application increases. Force-strain curve using eq. (3.1) with E_0 = 7.6 MPa is presented demonstrating a good agreement with experimental data. An increase in engineering strain can be observed when load time was increased from a few seconds to 30 seconds, while only slightly difference can be seen from 30 seconds to 180 seconds. The results show that elastic modulus E_0 =7.6 MPa is suited for the state close to equilibrium. This elastic modulus is similar to reported in[7] for o-rings made from the same material.

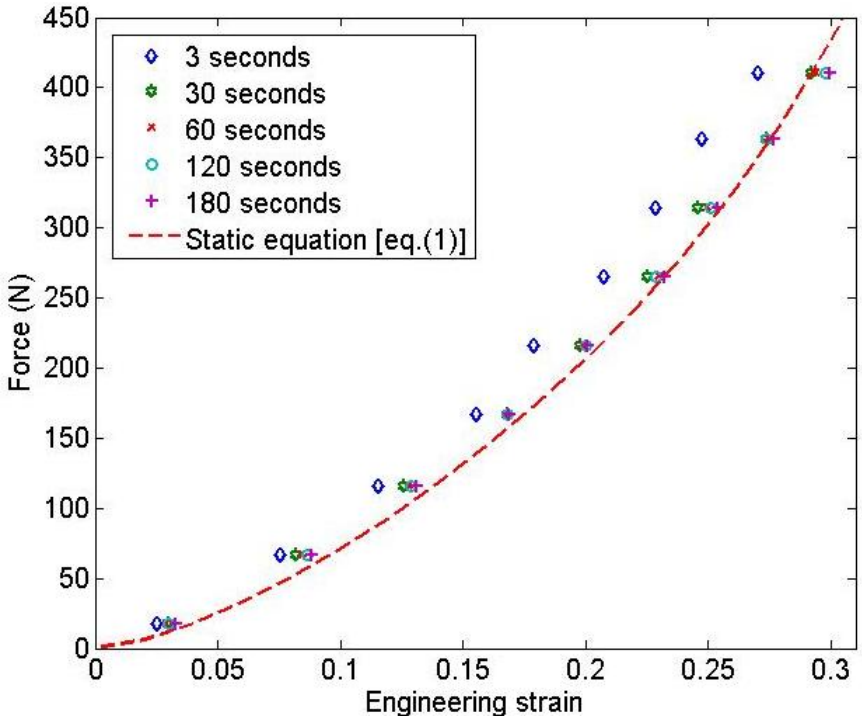

Figure 3-1 Results of quasistatic compression tests with Buna-N o-rings (outer diameter D = 20mm, diameter of cross section d = 5mm, mean diameter D_m = 15mm) corresponding to different times of load application (see insert on the left). The static equation with elastic modulus E_0 = 7.6 MPa is presented for comparison.

3.4 Deformation of a Buna-N O-ring Recorded by the High Speed Camera

Optical images of dynamically deformed o-rings were recorded by a high speed camera with a resolution 512 X 256. At this resolution, the maximum frame rate determined by the storing speed of flash memory is 40,000 fps (25 μs between every image). Six selected images of deformed o-ring impacted by drop mass with initial velocity 1.04 m/s are displayed in Figure 3-2 at corresponding times. T = 0 is defined as the first moment drop mass contact o-ring. The accuracy of defining sizes of o-ring, displacements of drop mass and upper piston supporting o-ring from optical images is 0.1mm, which is determined by the pixel size in the picture.

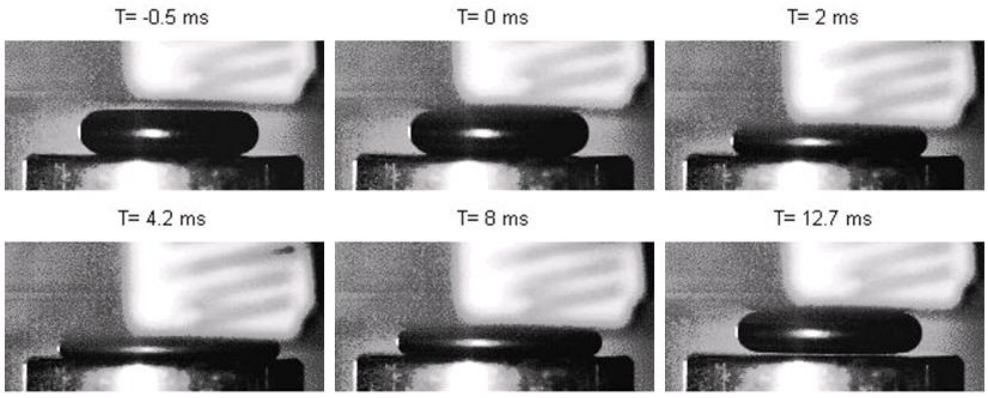

Figure 3-2 High speed camera images of a dynamically deformed Buna-N o-ring (initial outer diameter of o-ring D=20mm, mean diameter D_m =15mm, and diameter of circular cross section, d=5mm). The drop mass had initial velocity 1.04 m/s.

The position of drop mass and upper piston over time was tracked in every images recorded by high speed camera using image correlation algorithm. The displacements of drop mass, upper piston and the change of o-ring height (x) are plotted in Figure 3-3. The data were very repeatable in separate tests. The deformation of o-ring is derived from the relative movement between drop mass and upper piston when the o-ring stay in contact with both surfaces during the impact. The o-ring is supported by practically rigid upper piston which merely moved by 3 pixels corresponding to the displacement 0.25 mm. The deformation of o-ring is mainly caused by movement of the drop mass.

Note that eq. (2.3) was used to scale the movement of drop mass to calibrate for the difference in depth of view. This increases the accuracy of strain estimation.

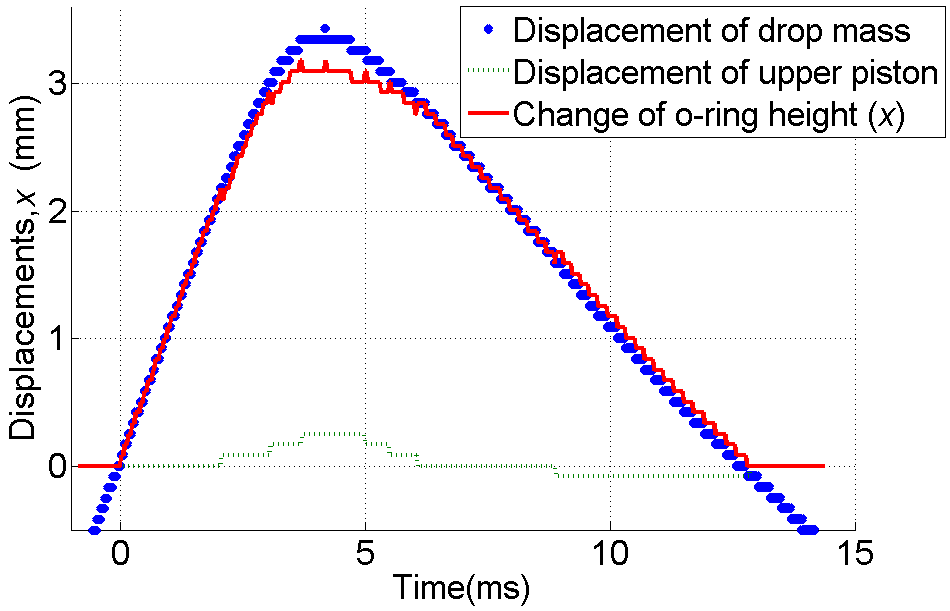

Figure 3-3 Displacements of the drop mass and upper piston from optical images recorded by high speed camera and change of compressed o-ring height (x). Buna-N o-ring (initial outer diameter of o-ring D=20mm, mean diameter D_m =15mm, and diameter of circular cross section, d=5mm). The drop mass had initial velocity 1.04 m/s.

From Figure 3-2 and Figure 3-3 it is clear that at time interval from 0 to 4.2 ms o-ring underwent large deformation with increasing contact area and decreasing strain rate at later stages. Strain rate on this compression stage is considered positive following convention accepted in literature on rubber [1,2], and it is characterized by the slope of corresponding curve in Figure 3-3. At T = 4.2 ms the o-ring reached its maximum compression (maximum $\boldsymbol{x}$) and the recovery of o-ring started. At T = 8 ms o-ring was about half way in recovery of its initial height with a negative strain rate of which absolute value is smaller than on the compression stage. The drop mass displacement curve is not symmetric on compression and recovery stages. This is due to energy dissipation during deforming process, which is reflected in different velocities of drop mass revealed by a difference in slopes of drop mass displacements on loading

and recovery phases in Figure 3-3. The duration of o-ring deformation is slightly less than 12.70 ms. At T = 12.70 ms drop mass separated from o-ring with a velocity 0.42 m/s (based on the slop of corresponding displacement curve in Figure 3-3).

The estimate of energy dissipated by o-ring can be calculated based on loss of kinetic energy of drop mass. The initial and final kinetic energies of the system are mostly determined by the velocity of drop mass because no significant movement is observed in supporting structure and the mass of o-ring is negligible comparing with drop mass. Velocity of drop mass started with 1.04 m/s downward, experiencing upward acceleration and ended up with 0.42 m/s upward. A total energy of 6.67 J was dissipated during the single impact corresponding to a coefficient of restitution 41%. An estimate of temperature increase of o-ring during impact assuming adiabatic process is equal 0.9K (o-ring weights 3.7 g and the heat capacity of Nitrile rubber is 1966 J/kg •K).

3.5 Force Acting on a Buna-N O-ring Recorded by Strain Gauges in the Load Cell

Force acting on the bottom part of o-ring is monitored by the strain gauges in the load cell supporting o-ring. Voltage signal form a load cell was converted to force (F) acting on the sample using Equation (2.2) and (2.3) with K = 2.1 *10^7 [N/V]. Force history recorded by strain gauge is shown in Figure 3-4, together with characteristic times observed from optical images marked by vertical lines.

Signal presented in Figure 3-4 demonstrates force history during the impact testing with initial impact velocity 1.04 m/s. The start of the impact corresponds to zero time in Figure 3-2, Figure 3-3, and Figure 3-4 . The force reached its maximum value

8964 N at 3.71 ms, and dropped back to zero at 9 ms.

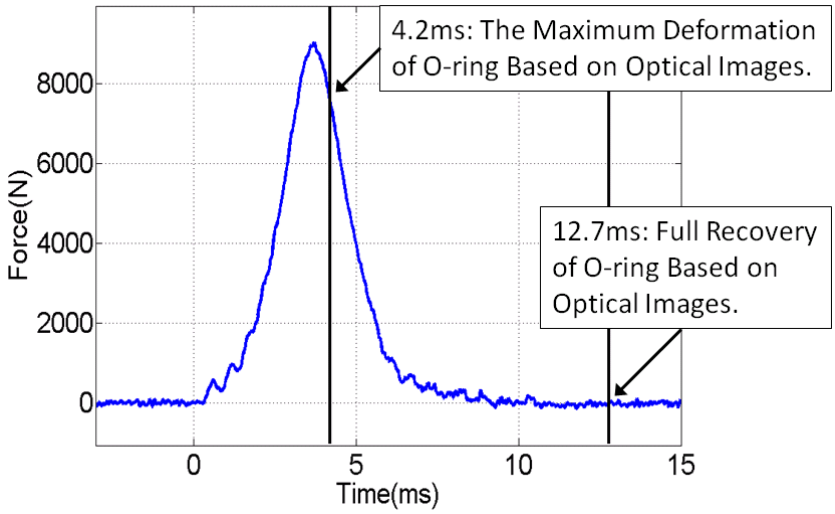

Figure 3-4 Force history recorded by strain gauges in the load cell together with characteristic times observed from optical images of a Buna-N o-ring (initial outer diameter of o-ring D=20mm, mean diameter D_m =15mm, and diameter of circular cross section, d=5mm). The drop mass had initial velocity 1.04 m/s.

It is clear from Figure 3-2, Figure 3-3, and Figure 3-4 that it took 4.2 ms to reach the maximum compression and less time 3.7 ms to reach the maximum force. The fact that the maximum force appeared 0.5 ms before the maximum compression is related to strain rate dependency of viscoelastic properties of o-ring. Similar phenomena of samples keeping straining after reaching the maximum stress commonly observed in high-strain-rate polymer testing [21]. The force- time curve (Figure 3-4) is pretty symmetric about its maximum value being in drastic difference with asymmetric behavior of deformation over time (Figure 3-3).

It is important to emphasize that despite high strain, strain rate deformation the final size of the o-ring measured after the test was the same as it was before impact with accuracy 0.1 mm. Also the initial height of o-ring experienced practically full recovery at 12.7 ms (Figure 3-2) testifying in favor of nonlinear Voigt model introduced later.

3.6 Acceleration, Velocity and Displacements of Drop Mass Based on Force Measurements

The force data collected from the load cell can be directly related to the acceleration of drop mass by Newton's second low. The force acting on the drop mass equals to the force acting on the sample plus gravity force. Therefore, velocity and displacement are available by numerical integration and results are presented in Figure 3-5 and Figure 3-6 . The optical images provide independent information about two integration constants for initial velocity and initial displacement. The velocity of drop mass is defined positive downward. Before and after impact, the velocity is only affected by gravity with a constant acceleration 9.81 m/s^2, friction act on the drop mass is negligible. During impact the o-ring experienced viscoelastic deformation and part of kinetic energy is dissipated resulting in the final velocity 0.41m/s according to optical data. The displacement of drop mass derived from integrating acceleration values based on load cell data matches very well with the data observed based on optical images.

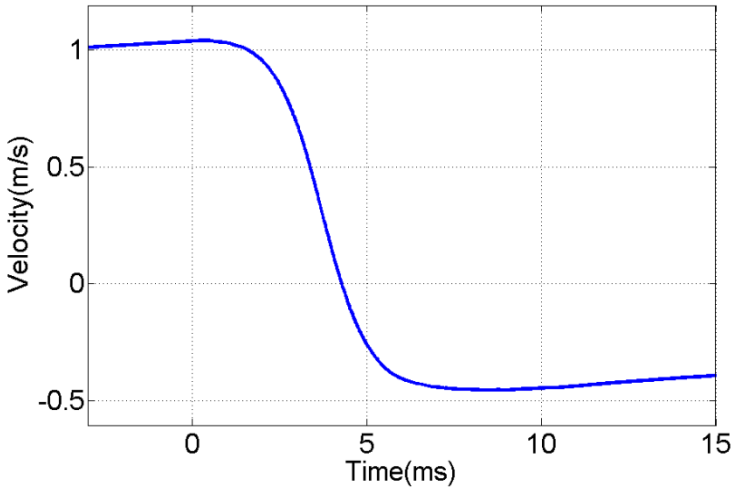

Figure 3-5 Velocity of drop mass derived from integration of acceleration values based on load cell data, gravitation force is included. Data corresponds to a Buna-N o-ring (initial outer diameter of o-ring D=20mm, mean diameter D_m =15mm, and diameter of circular cross section, d=5mm).

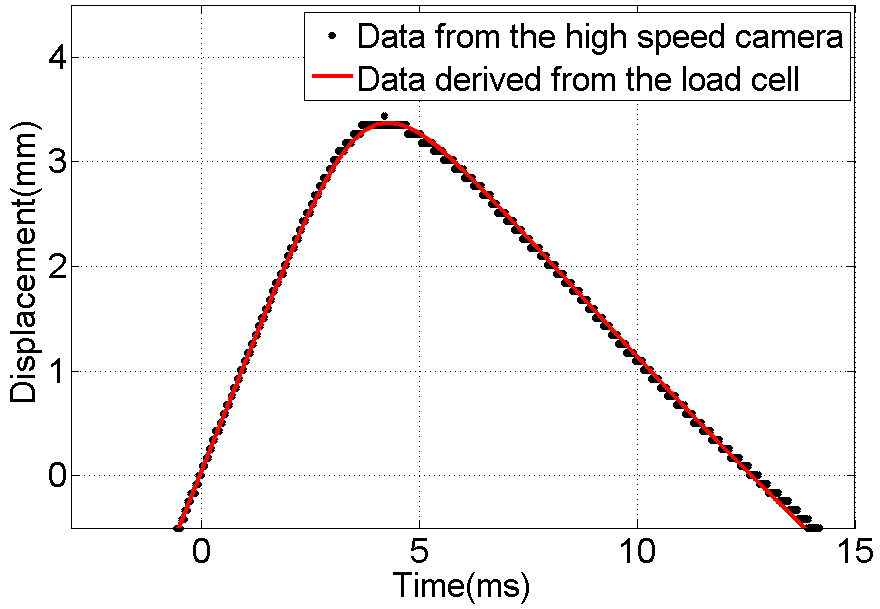

Figure 3-6 Comparing the displacement of drop mass derived from a record from strain gauge in a load cell and images recorded by high speed camera. Data corresponds to a Buna-N o-ring (initial outer diameter of o-ring D=20mm, mean diameter D_m =15mm, and diameter of circular cross section, d=5mm). The drop mass had initial velocity 1.04 m/s.

3.7 Deformation of O-ring with a Correction for Displacement of Upper Piston

Only the displacement of drop mass can be derived from integrating acceleration data based on strain gauges records in load cell. But the change of o-ring height is also slightly affected by the displacement of upper piston supporting it. With the information acquired from optical images this correction was introduced. The displacements of drop mass derived from a load cell data together with corrected data points from optical images are shown in Figure 3-7. We use these corrected data to get strain and strain rate of o-ring. Similar method using high speed camera to record strain was also used by Roland [22].

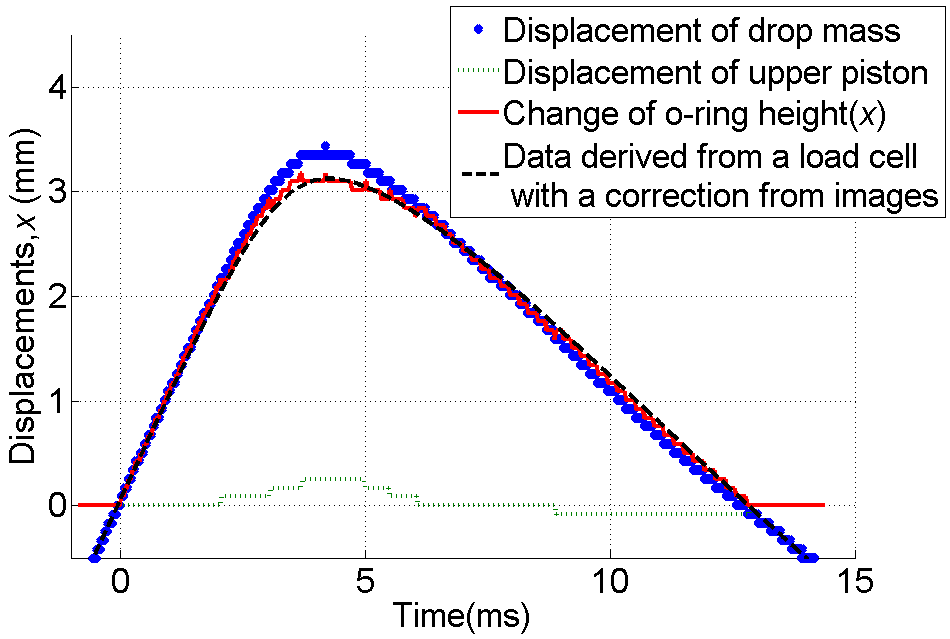

Figure 3-7 Displacements of drop mass and upper piston from optical images recorded by high speed camera and change of compressed o-ring height (x). The dashed black line is integrated from strain gauge data with correction obtained from the optical images of upper piston movement. Buna-N o-ring (initial outer diameter of o-ring D=20mm, mean diameter D_m =15mm, and diameter of circular cross section, d=5mm). The drop mass had initial velocity 1.04 m/s.

3.8 Dynamic Force-Strain Relation for Buna-N O-rings

The change of o-ring height from optical images and corresponding force data from a load cell were used to plot force over engineering strain in Figure 3-8. At the same strain the force on the loading path is higher than that on unloading path exhibiting a strong hysteresis effect. The eye shaped area between the two curves reflects the dissipation in one compression-extension cycle.

The elastic energy and dissipated energy stored in the o-ring during the initial compression stage of testing (until maximum compression was reached) can be estimated as work done by the force acting from the drop mass on o-ring until maximum deformation. The numerical integration result is 8.72 J; while the kinetic and gravitational

energy lost based on initial velocity (1.04 m/s) and maximum displacement (3.4mm) of drop mass is 8.63J. The slight difference between these two values is due to experimental error in measurements of force and displacements. The final kinetic energy of drop mass after impact is due to released elastic energy stored in o-ring minus energy dissipated during recovery stage and increase of gravitational energy. The numerical integration of force over displacement during recovery stage resulted in energy 1.78J which is very close to the value 1.81 J obtained based on final velocity (0.42 m/s) and negative displacement (3.4mm) of drop mass. This proves that the force acting on the drop mass is mainly caused by the force measured in the force chain and friction between drop mass and supporting rails and column is negligible.

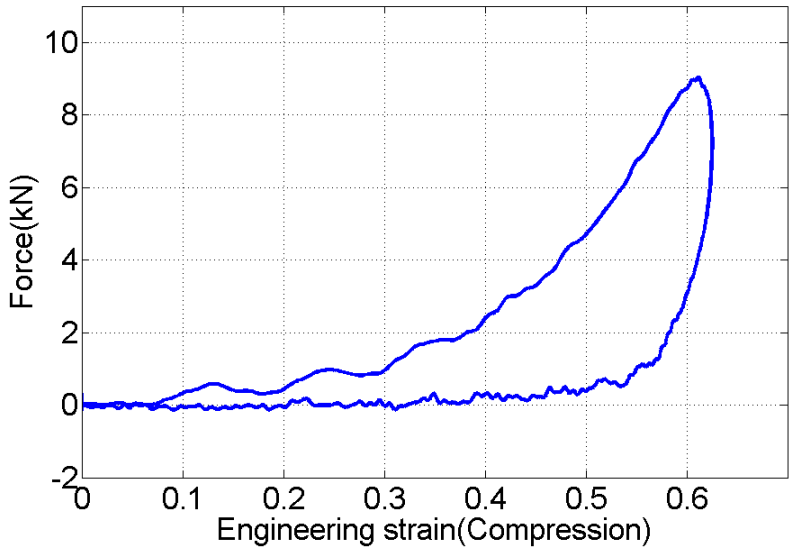

Figure 3-8 Force (from load cell record) versus global engineering strain in a o-ring (based on change of height of o-ring from optical images), the dynamic response of o-ring corresponding to impact with initial velocity 1.04 m/s. Data corresponds to a Buna-N o-ring (initial outer diameter of o-ring D=20mm, mean diameter D_m =15mm, and diameter of circular cross section, d=5mm).

The corresponding engineering strain rate versus strain is presented in Figure 3-9. It started with 196 s^{-1} and its value monotonous decreases as strain reaches its maximum

value. The transition of strain-rate from positive to negative happens at the maximum strain. After that, o-ring recovers its initial size with a lower strain-rate close to -85 s^{-1}.

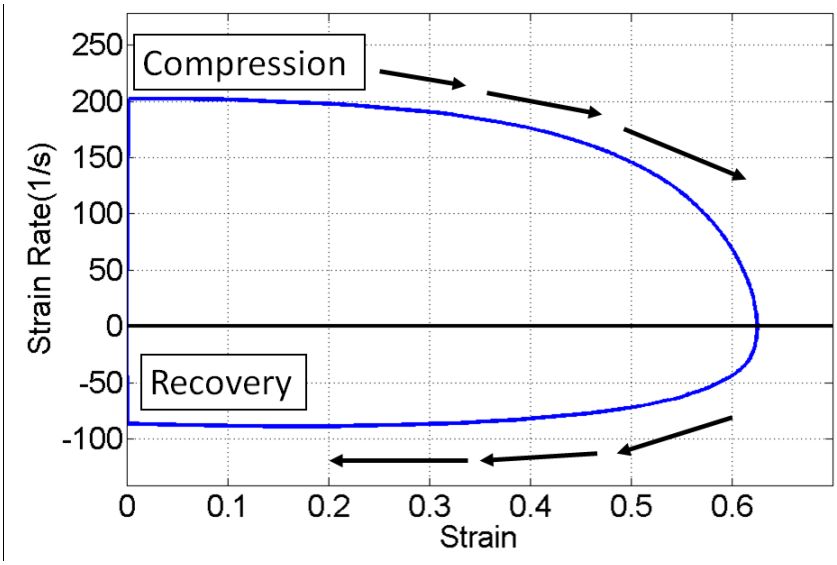

Figure 3-9 Engineering strain rate from integrated acceleration based on force measurements by strain gage versus strain (from optical images). Data corresponds to a Buna-N o-ring (initial outer diameter of o-ring D=20mm, mean diameter D_m =15mm, and diameter of circular cross section, d=5mm). The drop mass had initial velocity 1.04 m/s.

3.9 Viscoelastic Dynamic Equation for Buna-N O-rings with Linear Strain-Rate Dependence Viscous Term

Force over engineering strain data was obtained using force measured from strain gauges and strain data calibrated by optical images. We assume that the total force due to dynamic deformation of o-ring includes static and dynamic parts. During dynamic deformation, the static part follows double power law (eq. (2.1)) from geometry induced nonlinearity. The elastic modulus E_0 was found in independent measurements in the previous paragraph under static conditions and was equal 7.6 MPa correspond to 3 minutes compression. The first attempt will be to consider a dynamic term being linearly dependent on global strain rate experienced by o-ring and proportional to an effective viscosity coefficient α $[N \cdot s/m]$. This linear viscous model of dynamic

component of force added to strongly nonlinear static component is presented in Eq. (3.3).

$$F = \pi D_m d E_0 \left[1.25\left(\frac{x}{d}\right)^{1.5} + 50\left(\frac{x}{d}\right)^{6}\right] + \alpha\dot{x} \qquad (3.3)$$

Figure 3-10 presents the numerically calculated force versus engineering strain (x/d) curve with different viscosity coefficients α = 500, 5000 [$N \cdot s/m$] corresponding to the impact with 1.04 m /s on Buna-N o-ring (initial outer diameter of 0-ring D=20mm, mean diameter D_m =15mm, and diameter of circular cross section, d=5mm, drop mass 14.4 kg).

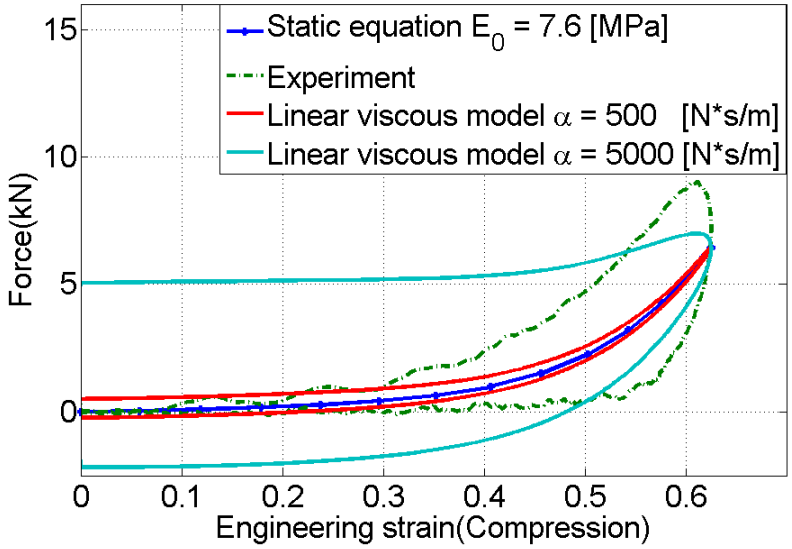

Figure 3-10 Force versus strain, comparing results of linear viscous models and static force with experimental data. Data corresponds to a Buna-N o-ring (initial outer diameter of o-ring D=20mm, mean diameter D_m =15mm, and diameter of circular cross section, d=5mm). The drop mass had initial velocity 1.04 m/s.

It's obvious that the constant coefficient of viscosity does not provide a reasonable explanation of experimental results with a broad variation of coefficient α. From experimental data, the deviation from static equation is relatively small under small

engineering strain; however, the strain rate corresponding to initial deformation is high (206 s^{-1}). Under the linear viscous model, higher strain rate will result in a larger dynamic force term, and create a larger deviation in low strain comparing with high stain. This contradicts to experimental data and there's no single coefficient α which can fit results of this model with experimental data.

From comparison of experimental data and behavior of static force with strain it is clear that viscous term must has nonlinear dependence on strain. On the first stage of loading from the strain 0.3 to 0.6 (with decreasing positive strain rate) we observe increasing deviation of experimental data from static data that can be accomplished only with nonlinear increasing value of effective viscosity with strain. Strain dependence of viscosity may be introduced by considering strain dependence of elastic modulus E_0. But it should be mentioned that this constant is an effective elastic modulus describing behavior of o-rings at relatively large global strains (x/d) with high gradients of local strains inside deformed contact area of o-rings.

Strain dependent strongly nonlinear viscoelastic models of dynamic contact deformation between spherical particles were proposed by Brilliantov, Spahn, Hertzsch and Poschel [23] and Morgado and Oppenheim [24]. A strongly nonlinear strain and strain rate depending term in force-strain relation was introduced in these papers based on static elastic force-strain relation $F_{(el)}(\varepsilon)$, (eq. (2.4)):

$$F_{(dis)} = \eta_0 \dot{\varepsilon} \frac{\partial}{\partial \varepsilon} F_{(el)}(\varepsilon) \qquad (3.4)$$

We apply a similar approach for strongly nonlinear contact interaction of o-ring and rigid plate, static and corresponding dynamic components of force using eqs. (2.1), and (2.4) are presented in eq. (3.5):

$$F(t) = \pi D_m d E_0 \left[1.25 \left(\frac{x}{d}\right)^{3/2} + 50 \left(\frac{x}{d}\right)^{6}\right] + \pi D_m d \eta_0 \left[1.875 \left(\frac{x}{d}\right)^{1/2} + 300 \left(\frac{x}{d}\right)^{5}\right] \left(\frac{\dot{x}}{d}\right) \tag{3.5}$$

The corresponding curves for static (E_0= 7.6 MPa) force based on Eq. (2.1) and dynamic force based on Eqn. (3.5) also with E_0=7.6 MPa and η_0=7.5 [KPa·s]) together with experimental dynamic data are plotted in Figure 3-11. The results of strongly nonlinear static and dynamic equations for o-ring satisfactory describe the expereimental data with 1.04 m/s impact velocity. During compression phase the resulting forces are larger than static prediction which is explained by strain rate dependence of dynamic behavior of o-rings. Our approach did not include possible dependence of effective elastic modulus E_0 on strain rate which is another possible approach for strongly nonlinear viscoelastic behavior of o-rings. At engineering strain rates varied in experiments between 200 to -100 s^{-1} and the strain rate dependent term can provide an input to overall force up to 60%. Even more important is the fact that this term is responsible for energy dissipation during dynamic loading and unloading of o-rings.

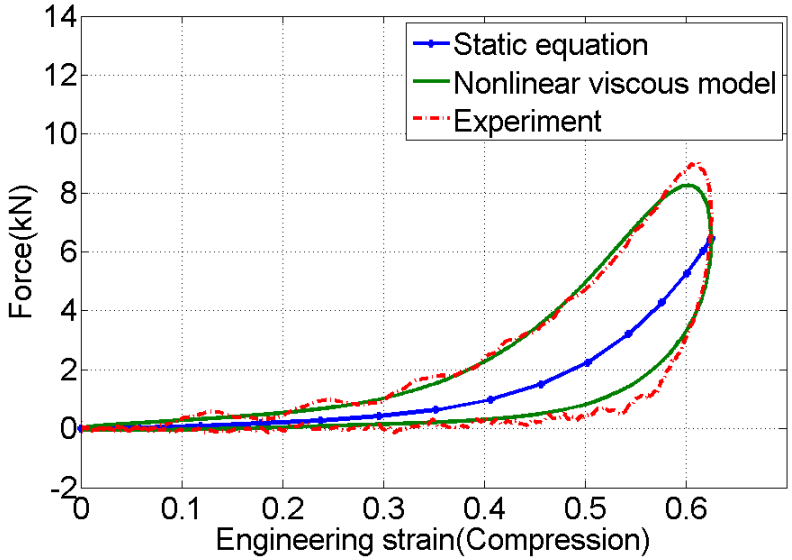

Figure 3-11 Force versus strain for dynamic deformation of o-rings based on Eq. (3.5) together with static empirical equation (Eq.(2.1)) in comparison with experimental results (E_0=7.6 MPa and η_0 =7.5 [KPa·s]). Data corresponds to a Buna-N o-ring (initial outer diameter of o-ring D=20mm, mean diameter D_m =15mm, and diameter of circular cross section, d=5mm). The drop mass had initial velocity 1.04 m/s.

It should be mentioned that used viscolestic model is dependent on sizes of o-ring. To check its validity for nonlinear viscoelastic behavior for different initial geometry of o-ring we performed experiments with Nitrile o-ring with width d=3mm and inner diameter 11 mm. The impact velocity is 0.6 m/s to achieve similar strain-rate and maximum strain. The results of experiments and numerical modeling based on Eqs. (2.1)and (3.5)are shown in Figure 3-12.

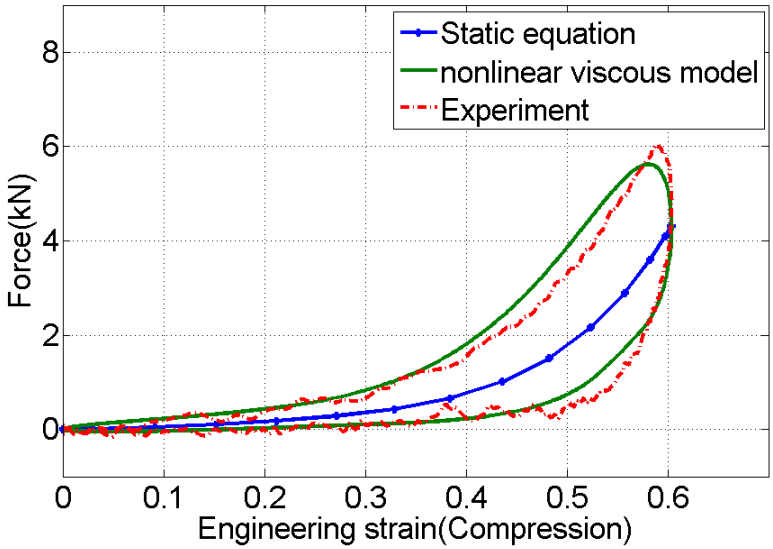

Figure 3-12 Dynamic and static equations for force in comparison with experimental results for an o-ring (E_0=7.6 MPa and η_0 =7.5 KPa·s). Buna-N o-ring (initial outer diameter of o-ring D=17mm, mean diameter D_m =14mm, and diameter of circular cross section, d=3mm). The drop mass had initial velocity 0. 6 m/s.

3.10 Conclusions

The instrumented dynamic test with three independent measurements of acceleration, displacement and force provide reliable data to analyze the strongly nonlinear viscoelastic dynamic response of toroidal rubber elements (o-rings). Forces independently recorded from accelerometer and load cell verified the force equilibrium in the sample during the impact, while optical images provided independent strain date and described deformation history of o-rings. The displacements of drop mass based on integrating its acceleration using data from load cell agree with that observed from optical images. Strain and strain-rate during dynamic deformation of o-rings also were determined using data from a load cell with a correction of bottom (upper piston) movement from optical images. Measurements of forces and strains demonstrated strain dependent strongly non-linear dynamic force-strain relations for o-rings.

Modeling of nonlinear dynamic force-strain data for viscoelastic behavior of o-ring was successfully accomplished using approach by Brilliantov, Spahn, Hertzsch and Poschel [23] and Morgado and Oppenheim [24] initially proposed for contact of spherical particles.

It was shown that the force-strain behaviors of two o-rings with different geometries were repeatable under multiple impacts testing of the same o-ring (velocity of each impact 1 m/s).

The "soft" drop weight impact test using o-ring can greatly decrease high-frequency excitations by ramping the applied forces, which will be useful for the testing of low strength samples of reactive materials.

Chapter 3 contains part of the material published in the paper Dynamic Deformation of Strongly Nonlinear Toroidal Rubber Elements in Journal of Applied Physics 2013. The dissertation author was the primary investigator and author of this paper.

3.11 References

1. P. Lindley, (1966) "Load-compression relationships of rubber units." The Journal of Strain Analysis for Engineering Design 1, 190.

2. P. Lindley, (1966) Jour. Inter. Rubber Inst. 1, 202.

3. K. Yurekli, R. Krishnamoorti, M. Tse, K. Mcelrath, A. Tsou, and H.-C. Wang, (2001) "Structure and dynamics of carbon black-filled elastomers." Journal of Polymer Science Part B: Polymer Physics 39, 256.

4. A. Freidenberg, C.W. Lee, B. Durant, V. F. Nesterenko, L. K. Stewart, G. A. Hegemier, (2013) "Characterization of the Blast Simulator elastomer material using a pseudo-elastic rubber model." International Journal of Impact Engineering, 60, 58.

5. E. Herbold, and V. Nesterenko, (2007) “Solitary and shock waves in discrete strongly nonlinear double power-law materials.” Applied Physics Letters 90, 261902.

6. P. Dias, A. Rosas, A. H. Romero, K. Lindenberg, (2010) “Pulse propagation in a chain of o-rings with and without precompression.” Physical Review E 82, 031308.

7. A. Spadoni, C. Daraio, W. Hurst and M. Brown, (2011) “Nonlinear phononic crystals based on chains of disks alternating with toroidal structures.” Applied Physics Letters 98, 161901.

8. V. F. Nesterenko, (2003) “Shock (Blast) Mitigation by ‘soft’ condensed matter” in MRS Symp. Proceedings, Vol. 759, edited by S. Sen, M. Hunt, and H. AJ (Pittsburgh, PA, 2003).

9. V. F. Nesterenko, Dynamics of Heterogeneous Materials (Springer-Verlag, 2001) Chap. 3.

10. S. M. Walley, D. J. Chapman, D. M. Williamson, M. J. Morley, T. W. Fairhead, and W. Proud, (2009) “High rate mechanical properties of Dyneema in compression.” Proceedings of DYMAT, 1133.

11. W. G. Proud, D. Porter, P. J. Gould, D. M. Williamson and S. M. Walley, (2010) “The Mechanical Performance of Polymers and Polymer Composites.” in Proceedings of IMPLAST 2010 conference, Rhode Island, USA, October 12-14 2010, Society for Experimental Mechanics, Inc.

12. E. H. Wong, C. Selvanayagam, S. Seah, W. Van Driel, J. Caers, X. Zhao, N. Owens, L. Tan, D. Frear, M. Leoni, S. Y, and C.L. Yeh, (2008) Journal of Electric Materials 37, 829.

13. W. G. Proud, S. M. Walley, D. M. Williamson, A. L. Collins, and J. W. Addiss, (2009) “Recent trends in research on energetic materials at Cambridge.” Central European Journal of Energetic Materials 6, 67.

14. J. Addiss, J. Cai, S. M. Walley, W. G. Proud, and V. F. Nesterenko, (2007) “High stain and strain-rata behaviour of PTFE/aluminuim/tungsten mixtures” in shock compression of compression of condensed matter- 2007, Proceedings of the Conference of the American Physical Society Topical Group on Shock Compression of Condensed Matter, edited by M. Elert, M.D. Furnish, R. Chau, N. Holmes, and J. Nguyen (American Institute of Physics), pp. 773-776.

15. E. B. Herbold, V. F. Nesterenko, D. J. Benson, J. Cai, K. S. Vecchio, and F. Jiang. (2008) “Particle size effect on strength, failure, and shock behavior in polytetrafluoroethylene-Al-W granular composite materials.” Journal of Applied Physics 104.10: 103903.

16. K. Olney, P. Chiu, C. Lee, V. Nesterenko, and D. Benson, (2011) “Role of material properties and mesostructure on dynamic deformation and shear instability in Al-W granular composites.” Journal of Applied Physics 110, 114908.

17. D. Radford, S. Walley, P. Church, J. Field, (2003) “Dynamic upsetting and failure of metal cylinders: Experiments and analysis” in Journal de Physique IV (Proceedings), Vol. 110 pp. 263-268.

18. J. Field, S. Walley, and W. Proud, H. Goldrein, and C. Siviour, (2004) “Review of experimental techniques for high rate deformation and shock studied.” International Journal of Impact Engineering 30.7, 725.

19. V. F. Nesterenko, P. Chiu, C. H. Braithwaite, A. Collins, D. M. Williamson, K. L. Olney, D. J. Benson, and F. McKenzie, (2012) “Dynamic behavior of particulate/porous energetic materials.” in AIP Conference Proceedings, Vol. 1426, p.533

20. L. Mullins and N.R. Tobin, (1965) “Stress softening in rubber vulcanizates. Part I. Use of a strain amplification factor to describe the elastic behavior of filler-reinforced vulcanized rubber.” Journal of Applied Polymer Science 9, 2993.

21. G. Gray III, W. Blumenthal, C. Trujillo, and R. Carpenter II, (1997) “Influence of Temperature and Strain Rate on the Mechanical Behavior of Adiprene L-100.” Le Journal de Physique IV, 7,C3.

22. C. Roland, (2006) “Mechanical Behavior of Rubber at High Strain Rates.” Rubber chemistry and technology 79, 429.

23. N. V. Brilliantov, F. Spahn, J.-M. Hertzsch and T. Poschel, (1996) “Model for collisions in granular gases.” Physical review E 53, 5382.

24. W. Morgado, and I. Oppenheim, (1997) “Energy dissipation for quasielactic granular particle collisions.” Physical Review E 55, 1940.

CHAPTER 4

INVESTIGATION OF PATH DEPENDENT RESPONSE OF STRONGLY NONLINEAR VISCOELASTIC TOROIDAL ELEMENTS

4.1 Introduction

Toroidal elements (o-rings) are widely used in their pre-compressed state in hydraulic and pneumatic equipments in sealing of drive shafts, pistons and lids. Their nonlinear static elastic properties are well studied [1,2] and used for the design of o-rings irrespective of strain rates and loading path. The characteristic highly non-linear elastic behavior of o-rings comes from geometry changes during deformation and also from nonlinear viscoelastic behavior of the elastomer under high strain deformation [3]. This property also makes them one of the preferred elements to assemble strongly nonlinear double power law low dimensional metamaterials [4-7] which are more tunable than chains composed from spherical particles [8,9].

Polymer o-rings are also preferential candidates to modify drop weight tests to reduce unwanted high frequency excitations generic for these tests [10-13]. But dynamic properties of these elements and their path dependence on initial loading conditions are practically unknown unlike their static behavior.

Information about the dynamic deformation of o-rings is needed to design their response to dynamic conditions of loading in heavy machinery, e.g., to interpret soft drop weight test. Deformation of rubber toroidal elements (o-rings) was investigated under

dynamic loading conditions at strain rates 10^2 s^{-1}. [14] It was found that dynamic behavior of initially uncompressed o-rings is significantly stiffer than under static loading and follows strongly nonlinear dependence on strain and strain rate in accord with Brilliantov et all [15] and Morgado et all [16] approach.

It should be mentioned that dynamic deformation of contacts of polymer spheres (PTFE [17], Parylene-C [18]) with each other or with rigid walls is also characterized by increased stiffness. The similar behavior of dramatically increased effective dynamic stiffness based on measured sound speed in periodic metamaterials composed from steel cylinders and precompressed Buna-N o-rings observed in experiment [7].

In this paper we investigated deformation history of o-rings in a broader range of impact velocities than reported in [14] and under high strain pre-compression conditions. Strong path dependence (with and without pre-compression) of force-displacement curves was demonstrated in experiments. In this broader dynamic strain range strain-rate effect cause more rigid behavior of o-rings while pre-compression changes the loading path. The dynamic stiffness of o-rings at the vicinity of precompressed strains was significantly larger not only than the corresponding static stiffness, but also larger than dynamic stiffness of uncompressed o-ring at similar strain.

The behavior of uncompressed o-rings under high strain-rate deformation is discussed in this paper and three models are analyzed according to their ability to explain experimental results. The first two models use linear strain-rate dependence, while the third one uses power-law strain-rate dependence of viscous term. The first model proposed by Brilliantov et all [15] and Morgado and Oppenheim [16] is based on o-ring's static empirical equation proposed by Lindley [1,2]. This model was successfully used to

describe a significant difference in force between static and dynamic loading of o-rings [14]. Another model, Hertz-damp model [19-22] is using a nonlinear damper to express dynamic deformation of contact spherical rubber elements. It was successfully applied for simulating the semi-sphere rubber shock absorbers to mitigate structural pounding during earthquakes [23]. Based on the experimental results we proposed the third model in which we keep static term and nonlinear dependence of viscous term on strain as in Brilliantov et all [15] and Morgado et all [16], but introducing power-law strain-rate dependence in accord with experimental results. It was demonstrated that the third model explains experimental data better in a broad range of dynamic strain, strain rates. Experimental data on dynamic behavior of precompressed o-rings demonstrated path dependent behavior which was explained by adding memory effect from precompression introducing a new parameter - critical engineering dynamic strain. Exceeding this strain results in a loss of memory effect. It should be emphasized that we are trying to propose a relatively simple, phenomenological model of high strain, high strain rate dynamic behavior of toroidal o-rings under contact deformation with large gradients of strains and stresses where complex geometry and material properties are responsible for the strongly nonlinear and path dependent outcome.

4.2 Experimental Setup

High strain/strain-rate behavior of o-rings was investigated using modified Instron drop tower 9250HV as discussed in previous paper [14]. A high speed camera Phantom V12 with a frame rate 40,000 fps is used to capture images of deformed o-rings and translate it to their strain history. A customized load cell with strain gauges is used to

measure dynamic force. In previous research using accelerometers mounted on the drop weight we demonstrated force equilibrium in o-rings was achieved under similar conditions of dynamic deformation. The accuracy of force measurement is associated with analog to digital resolution of the oscilloscope, which is 4 mV, corresponding to 80 N in force.

Experiment set up for the testing of single o-ring is presented in chapter 2.2. Two 3mm thick steel disks are place above and below the tested o-ring to improve accuracy in the images recorded by a high speed camera. Adding these disks allows us to increase accuracy of strain measurement.

The tests of pre-compressed o-rings were performed using configuration introduced in chapter 2.3 by placing the special holder with a few o-rings on the top of the lower piston. This holder is shown in Figure 2-4. It can provide a desired level of identical pre-compression on a few o-rings. The pre-compressed o-rings are assembled to be deformed in practically identical conditions (verified using optical images) thus increasing accuracy of measurements of strain in each o-ring.

Polymer o-rings exhibit creep behavior under loading with long relaxation times. In order to perform tests in similar initial conditions, a 3-minutes pre-compression was used before each dynamic test. This is the same period of time used to determine the elastic constant of static double power law equation of Buna-N o-rings.

When extracting strain history from high speed images we took into account that different depth of view of objects can cause misinterpretation. Positions of two steel disks adjacent to the bottom and top plates were used to extract accurate data on deformed sizes of all o-rings (with accuracy 0.1mm) based on their high speed images.

This chapter presents results of the dynamic tests of Buna-N rubber o-rings (McMaster-CARR, durometer hardness A70, ASTM D2000/SAE J00 standard) with diameter of circular cross section, *d* equals to 5 mm, outer diameters *D* equals to 20 mm, mean diameters D_m equals to 15mm. The results of uncompressed o-rings impacted with velocities in the range 0.5 m/s to 1.5 m/s is analyzed. Precompressed o-rings were impacted with velocity 2.5 m/s to provide strain rates close to 10^2 s^{-1}, similar to the experiments with uncompressed o-rings impacted with velocity 0.5 m/s and of the same order of magnitude as in tests with larger velocities of impact on uncompressed o-rings.

4.3 Optical Images of O-rings Recorded by the High Speed Camera

Optical images of dynamically deformed o-rings were recorded by a high speed camera with a resolution 512 X 256 at frame rate 40,000 fps (25 μs between every image). Six selected images of deformed o-ring impacted by drop mass with initial velocity 1.50 m/s are displayed in Figure 4-1 at corresponding times.

T = 0 is defined as the first moment drop mass contact o-ring. The accuracy of defining sizes of o-ring, displacements of 3mm disks placed above and beneath the o-ring from optical images is 0.05mm, which is determined by the pixel size in the picture. The displacement and strain data of the o-rings are calculated using the same procedures as discussed in Chapter 3. The same instrument setup is used for dynamic testing of o-ring using impact velocity 0.5m/s, 0.75m/s, 1.0m/s, 1.25m/s, and 1.5m/s.

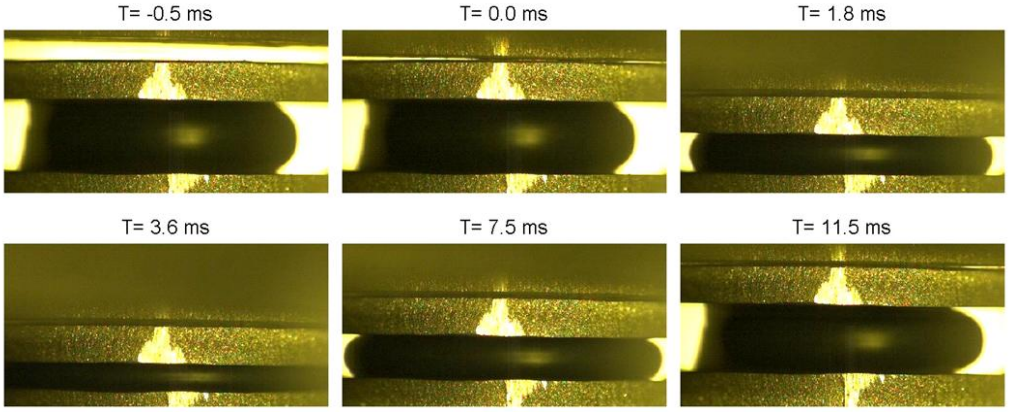

Figure 4-1 High speed images of a dynamically deformed Buna-N o-ring (initial outer diameter of o-ring D=20mm, mean diameter D_m =15mm, and diameter of circular cross section, d=5mm). The drop mass had initial velocity 1.5 m/s.

4.4 Dynamic Force-Strain Relation for O-rings

The results for dynamic force versus engineering strain corresponding to impact tests with impact velocity 0.5 m/s, 0.75 m/s, 1.00m/s, 1.25m/s, and 1.50m/s are shown in Figure 4-2. In this figure the static equation (eq.(3.1)) with E_0 =7.6 MPa is also presented.

We can see that there is 2~3 times difference in force at static tests and in dynamic deformation at the same strains. Apparently a strain-rate dependent behavior of o-rings is causing their significantly stiffer behavior. It should be mentioned that accuracy of the measurements does not allow us to conclude that the static curve with E=7.6 MPa correctly predict the value of the force at the maximum strain when strain rate equal zero. Engineering strains were taken from optical high speed images synchronized with force measurements similar to previous work [14].

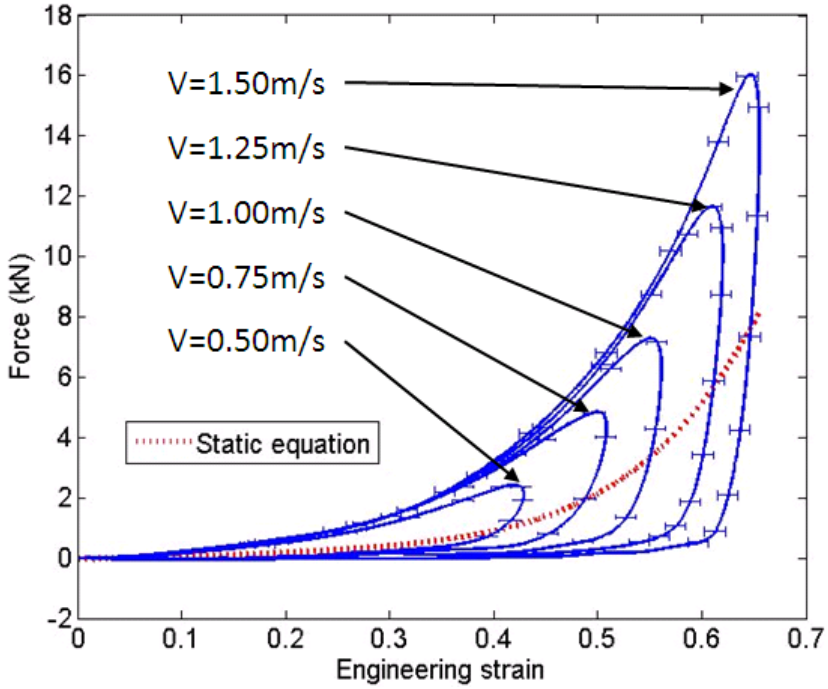

Figure 4-2 The force versus engineering strain for Buna-N o-rings (initial outer diameter of o-ring D=20mm, mean diameter D_m =15mm, and diameter of circular cross section, d=5mm) impacted by the drop mass with initial velocities 0.50 m/s, 0.75 m/s, 1.00 m/s, 1.25 m/s, 1.50 m/s, and 1.5 m/s. Static equation with E=7.6 MPa is shown by a dotted line.

The corresponding behavior of strain-rates over engineering strains on loading and unloading stages at different impact velocities are shown in Figure 4-3. Engineering strain rates were calculated based on integration of acceleration found using force measurements and known drop mass. Small corrections were introduced from optical high speed images synchronized with force measurements similar to previous publication [14]. It is clear that on the stage of compressive loading (up to 80% of maximum engineering strain in each individual test) corresponding strain-rates are proportional to the initial impact velocity. They are of the order 10^2 s^{-1} for tests with impact velocity more than 0.5 m/s. Sharp changes in strain-rates correspond to sharp changes in forces in the vicinity of maximum

engineering strain pointing out the significant role of strain rate effects in the behavior of o-rings.

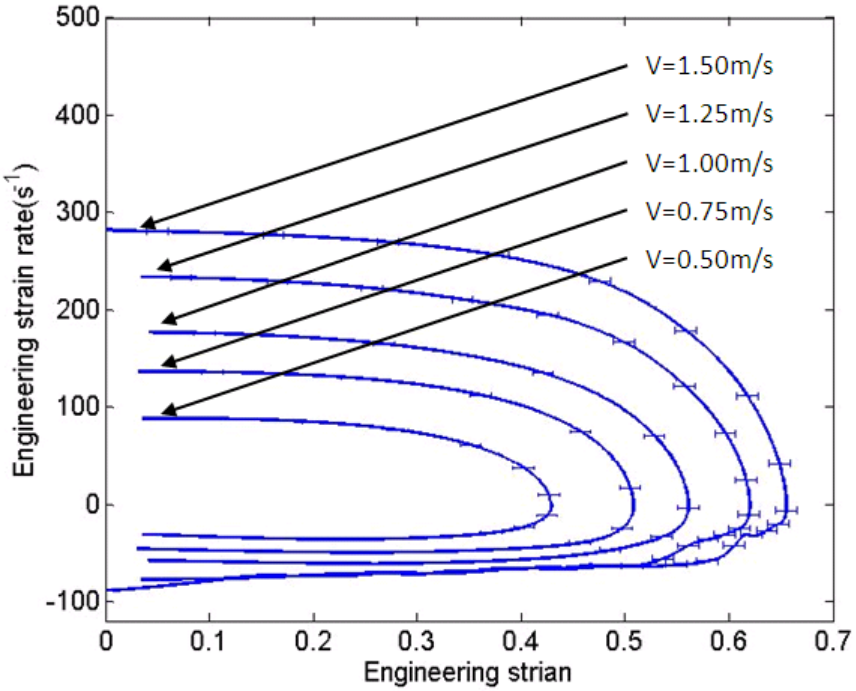

Figure 4-3 Engineering strain rate versus engineering strain. Data corresponds to Buna-N o-rings (initial outer diameter of o-ring D=20mm, mean diameter D_m =15mm, and diameter of circular cross section, d=5mm) impacted by the drop mass with initial velocities 0.50m/s, 0.75m/s, 1.00m/s, 1.25m/s, 1.50m/s, and 1.5m/s.

In order to analyze this viscoelastic behavior we use the Voigt model with a non-linear dashpot in parallel with the nonlinear spring representing static response of o-ring. This model allows the return of o-ring to its practically original shape for a time about few milliseconds after load was removed as was observed experimentally using high speed images [14].

We will examine four different dynamic models to explain the dynamic strain rate dependent response of the o-rings:

4.5 Dynamic Equation for O-rings Using Linear Strain-Rate Dependence of Viscous Term

This dynamic model described by eq. (3.5) was proposed and verified in our previous paper [14] for the impact velocity equals 1 m/s. It was introduced by using eq. eq.(3.1)and following similar approach applied to nonlinear viscoelastic contact deformation between spherical particles proposed by Brilliantov, Spahn, Hertzsch and Poschel [15] and Morgado and Oppenheim [16].

Figure 4-4 compares predictions based on this model with experimental data. The curves in Figure 4-4 were obtained using values of E_0 = 7.6 MPa and η_0 = 16 KPa·s. In the model total force is a function of instantaneous strain and strain-rates (depicted in Figure 4-3) and it is not sensitive to deformation path.

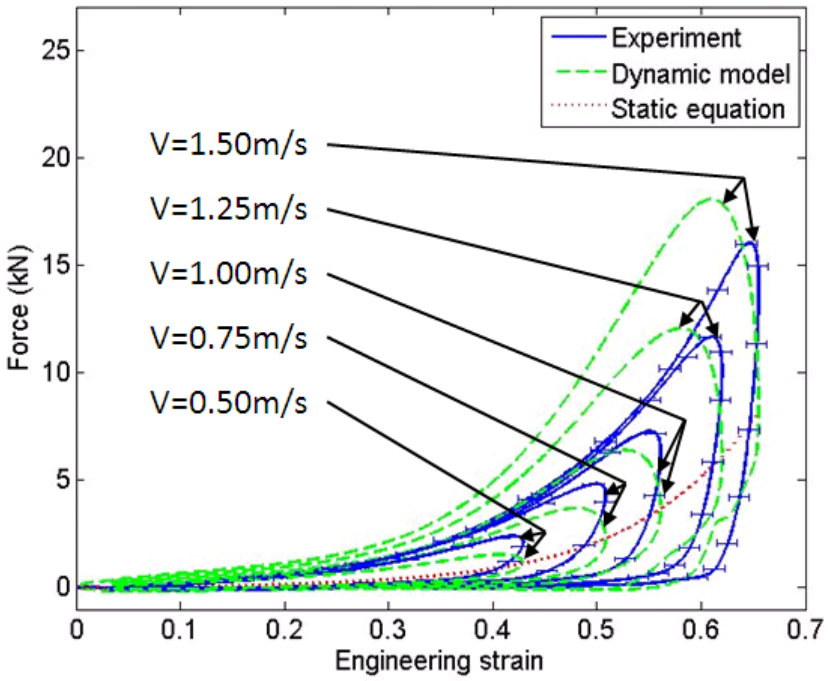

Figure 4-4 Comparison of the prediction from the dynamic model with linear strain-rate dependence on viscous term with experimental results. A static equation with E=7.6 MPa is shown by a dotted line.

We can observe that the values of force in a static curve at maximum strain correspond to the predictions by viscoelastic model at maximum strains and strain rates equal zero. The similar behavior is difficult to detect in dynamic curves due to limitations imposed by accuracy of experiments. This model agrees reasonably well with experimental data corresponding to impact velocity 1 m/s, but it underestimate value of forces at velocities 0.5m/s, 0.75m/s. At the same time we can conclude that this model overestimates the force at higher impact velocities 1.25m/s and 1.5m/s on the loading path being close to experimental data on the unloading path.

4.6 Dynamic Equation for O-rings Using Hertz-Damp Model

To check if this experimental behavior is better explained by another approach following Hertz-damp model for dissipative contact interactions (with introduction of coefficient of restitution) also with linear dependence of viscous force on strain-rate and nonlinear dependence on strains [14]. Hertz-damp model has been used in robotics, multi-body systems and structure engineering [19-22] to describe contact interaction of spherical bodies. It has a linear strain-rate dependent damper term with nonlinear dependence on strain in conjunction with the Hertzian elastic contact force as represented by eq. (4.1)-(4.4)

$$F_{static} = k_h \delta^{1.5}, \tag{4.1}$$

$$F_{dynamic} = \xi \delta^{1.5} \dot{\delta}, \tag{4.2}$$

$$\xi = k_h \frac{3(1-e^2)}{4(v_1 - v_2)}, \tag{4.3}$$

$$F_c = F_{static} + F_{dynamic} = k_h \delta^{1.5} \cdot \left(1 + \frac{3(1-e^2)}{4(v_1 - v_2)} \dot{\delta}\right). \qquad (4.4)$$

where F_{static} is compression force of sphere object under static compression, $F_{dynamic}$ is a dynamic term caused by strain-rate effect, and F_c is a the total compressive force being equal to sum of static and dynamic forces, δ is a change of the distance between centers of impacting elements calculated from the start of their impact, k_h is impact stiffness parameter depending on the material properties, ξ is the damping constant which can be expressed in terms of k_h, the coefficient of restitution (e) , and relative approaching velocity $(v_1 - v_2)$ as shown in eq. (4.3) and (4.4).

There're two major differences between the model represented by eq. (3.5) (based on approach proposed by Brilliantov, Spahn, Hertzsch and Poschel [l5] and Morgado and Oppenheim [l6]) and Hertz-damp model. First of all, in a former model the nonlinear coefficient in viscoelastic component of force is proportional to the nonlinear elastic stiffness (derivative of static force with respect to strain) and in the Hertz-damp model the corresponding part of force is proportional to the nonlinear elastic force. Secondly, according to the model described by eq. (3.5), the coefficient in the dynamic force is a separate material property which can be chosen to fit experimental data. On the other hand, in Hertz-damp model the corresponding coefficient in expression for dynamic force is a function of impact velocity and coefficient of restitution which should be determined during the test.

We can modify Hertz-damp model proposed for contact deformation of spherical bodies to the behavior of o-ring which static compression is characterized by doable power. At small strains, up to 0.3, a force exhibits a Hertzian behavior (it is

proportional to $(x/d)^{3/2}$) and at higher strains another power law term is important too (proportional to $(x/d)^6$)[2]. The modified Hertz-damp model to describe dynamic behavior of o-ring is represented by eq. (4.5):

$$F(t) = \pi D_m d E_0 \left[1.25\left(\frac{x}{d}\right)^{3/2} + 50\left(\frac{x}{d}\right)^6\right] \cdot \left(1 + \frac{3(1-e^2)}{4(v_1 - v_2)}\dot{x}\right) \tag{4.5}$$

where v_1 is the initial impact velocity and v_2 is the initial velocity of supporting structure which is 0 in our experiments. The comparison of experimental results, data form calculations based on eq. (4.5) and static curve are plotted in Figure 4-5. The corresponding velocities of drop mass before impact and after were determined in our experiments based on high speed images of drop mass giving the restitution coefficients for each impact conditions.

We can see that in conditions of our experiments dynamic force calculated based on modified Hertz-damp model significantly underestimates force observed in experiments being rather close to the static model on stages of loading and unloading. It should be mentioned that we can't select parameters in Hertz-damp model to fit experimental data because the corresponding coefficient in expression for dynamic force is a function of impact velocity and coefficient of restitution is taken from experiments.

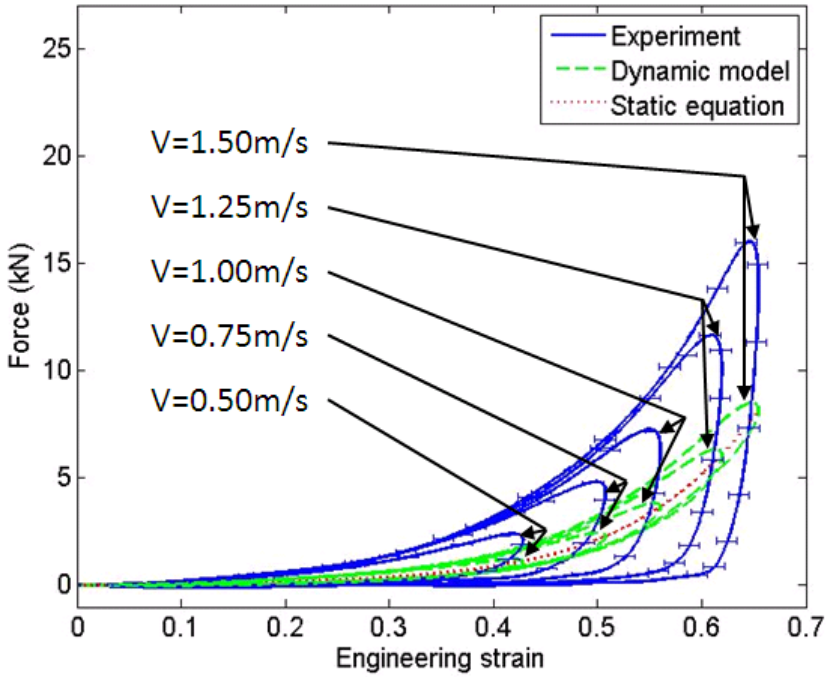

Figure 4-5 Dynamic behavior of Buna-N o-ring in experiments in comparison with results of Hertz-damp model. The impact velocity ranges from 0.5m/s to 1.5m/s. A static equation with E=7.6 MPa is shown by a dotted line.

4.7 Dynamic Equation for O-rings Using Power-Law Strain-Rate Dependence of Viscous Term

From presented analysis of two models we can see that they can't describe experimental results in the whole area of strain and strain rates. We notice that experimental data corresponding to impact velocities 1.25 m/s, and 1.50 m/s significantly deviates from predictions based on the first model. This can be expected because this model is modification of the approach proposed by Brilliantov, Spahn, Hertzsch and Poschel [l5] and Morgado and Oppenheim [l6] based on analogy with elastic contact interaction valid for small strains [l5]. Thus it is natural that this model has a restricted area of application with respect to strain and strain rate dependence. Indeed, experimental data presented in Figure 4-2, with corresponding strain rate histories presented in Figure 4-3,

clearly demonstrate that at the same strains, but different strain rates, dynamic force doesn't exhibit linear dependence on strain rates. For example, on the stage of loading, dynamic forces at the same strains corresponding to impact velocities 0.5 m/s and 1.5 m/s do not demonstrate a 3-4 times difference as observed for a strain-rates. It's also observed from Figure 4-2 and Figure 4-3 that a sharp force drop close to the maximum strain of each curve corresponds to a sharp change in strain-rate close to the maximum strain. Thus it also emphasizes that strain-rate dependence of force is crucial and must be taken in to account for adequate explanation of experimental results.

There are no published models on the viscoelastic behavior of contact deformation of o-rings at broad range of strain and strain-rate with weak dependence (weaker than linear) of force on strain rates. To account for weaker than linear dependence in strain-rate behavior of materials constitutive power law and logarithmic dependence of stresses on strain rates are widely used [25]. For example, logarithmic dependence on strain-rate for axially loaded rubber samples was proposed by Boyce et al., [26]. To account for observed weaker than linear strain-rate dependence of force during contact viscoelastic deformation of o-rings in experiments we introduce a new dynamic equation based on eq. (3.5), but with power-law strain-rate dependence as presented in eq. (4.6):

$$\begin{aligned} F(t) &= F_{static} + F_{dynamic} \\ &= \pi D_m d E_0 \left[1.25 \left(\frac{x}{d}\right)^{3/2} + 50 \left(\frac{x}{d}\right)^{6}\right] \\ &+ \pi D_m d \eta_0 \left[1.875 \left(\frac{x}{d}\right)^{1/2} + 300 \left(\frac{x}{d}\right)^{5}\right] \cdot sign(\dot{x}) \cdot \left(\left|\frac{\dot{x}}{d}\right| / \dot{\varepsilon}_{ref}\right)^{n} \end{aligned} \tag{4.6}$$

Positive and negative strain-rates are both experienced by o-rings during the

process of deformation and it's observed that positive (compressive) strain-rate significantly contribute to positive (compressive) dynamic force and vice versa. To avoid complex numbers at some values of power exponent we used the absolute value of $\dot{x}/d$ in power function and different paths (loading and unloading) are represented by sign function.

There are three parameters introduced in the model: η_0, $\dot{\varepsilon}_{ref}$, and *n*. Number *n* is the exponent in power law dependence of force on the strain-rate, which is smaller than 1 and greater than 0. The smaller the *n*, the less sensitive will be dependence of dynamic force on strain-rate. The parameter $\dot{\varepsilon}_{ref}$ is a reference state used in similar approaches to ensure nondimensional expression in the power law [25]. The parameter η_0 is a separate constant describing viscoelastic part of dynamic force in the model. It's observed that the same value of η_0 can be satisfactory used for both positive and negative strain-rates.

Figure 4-6 compares the viscoelastic model with power-law strain-rate dependence using eq. (4.6) with experimental data. The following model parameters were used: n = 0.5, $\dot{\varepsilon}_{ref} = 10^0[s^{-1}]$, $E_0 = 7.6\,MPa$, $\eta_0 = 140\,KPa$. We can see that this model fits experimental data on the loading path in the whole range of impacting velocities from V = 0.5m/s to V = 1.5m/s. Thus the power-law functional dependence of dynamic force on strain-rate reflects the phenomena observed in experiments with different strain rates. Another improvement demonstrated by this model is that it better reflects the transition from loading to unloading in the vicinity of maximum force.

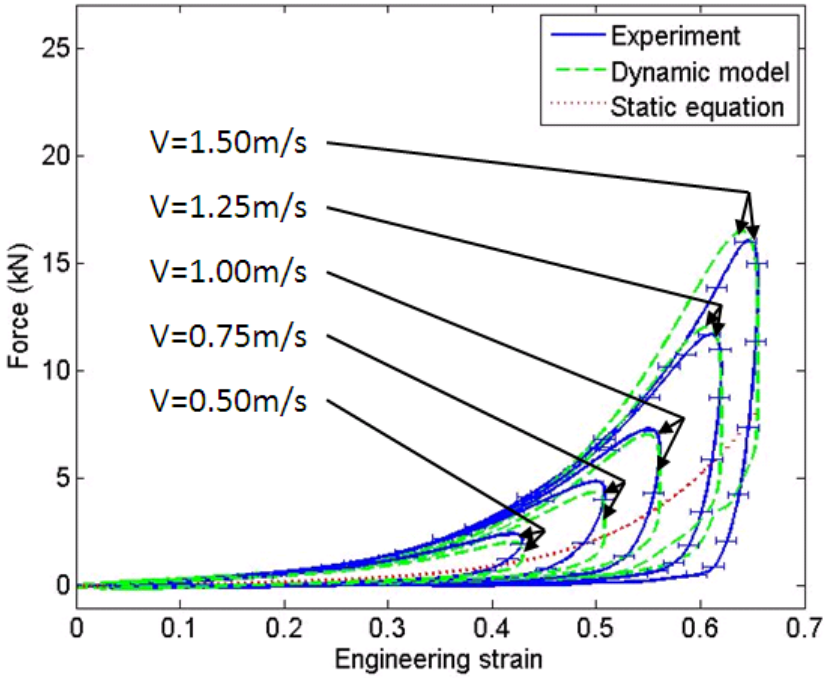

Figure 4-6 Comparison of dynamic equation with power law strain-rate dependence of viscous term with experimental data for Buna-N o-rings impacted by velocity from 0.5m/s to 1.5m/s. A static equation with E=7.6 MPa is shown by a dotted line.

This model is able to depict loading curve of dynamic deformation of o-rings while strain rate varies from 330/s to -110/s as shown in Figure 4-3. By using a power less than 1 on strain-rate, the model reflect the phenomena observed from experimental data that dynamic force is weakly associate with strain rate but still strongly affected by strain. Another improvement from this model compared with linear strain-rate dependence (Figure 4-4) is that it better reflects the transition close to maximum force.

From equation (4.6) and the non-linear stiffness equation of o-ring (eq.(3.2)), dynamic force can be expressed as following in eq. (4.7)

$$F_{dynamic} = \eta_0 \cdot d \cdot K_s \cdot sign(\dot{x}) \cdot \left(\left| \frac{\dot{x}}{d} \right| / \dot{\varepsilon}_{ref} \right)^n \qquad (4.7)$$

Eq. (4.7) demonstrates the dynamic part of the force as a function of static stiffness and power-law strain-rate dependence. In the model, dynamic force is

proportional to static stiffness of the o-ring (K_s) and is a function of engineering strain following double power law. The power law function presented a weaker than linear dependence on engineering strain rate.

The effect of changing *n* and $\dot{\varepsilon}_{ref}$ is discussed in the following paragraph.

Figure 4-7 shows the results of using two power law exponents (*n*=0.2 and *n*=0.8) in dynamic model with power-law strain-rate dependence while the value of reference strain–rate keeps the same. The effect of changing power law exponents in the dynamic model with power-law strain-rate dependence is similar to the effect of changing reference strain-rate in the dynamic model with logarithm strain-rate dependence. The value of η_0 changes correspondingly with the value of *n* to reflect experimental result. A smaller power number *n* comes with a larger dynamic force coefficient and vice versa. A model with a smaller power law exponents (as *n*=0.2 in Figure 4-7) shows a sharper change in the vicinity of the maximum force of each test. Smaller *n* also predicts smaller difference in dynamic force on loading path caused by increasing or decreasing dominant strain-rate. The loading curve with $n = 0.2$ overlap with each other while slight difference can be observed on loading curve with $n = 0.8$. When raising $\dot{\varepsilon}$ from 100/s to 200/s at the same strain level, a 15% change is predicted by a model with $n = 0.2$ and a 74% change is predicted by a model with $n = 0.8$ as shown in the following calculation.

$$\frac{\left(\frac{200}{10^0}\right)^{0.2} - \left(\frac{100}{10^0}\right)^{0.2}}{\left(\frac{100}{10^0}\right)^{0.2}} = 0.15 \qquad (4.8)$$

$$\frac{\left(\frac{200}{10^0}\right)^{0.8} - \left(\frac{100}{10^0}\right)^{0.8}}{\left(\frac{100}{10^0}\right)^{0.8}} = 0.74$$

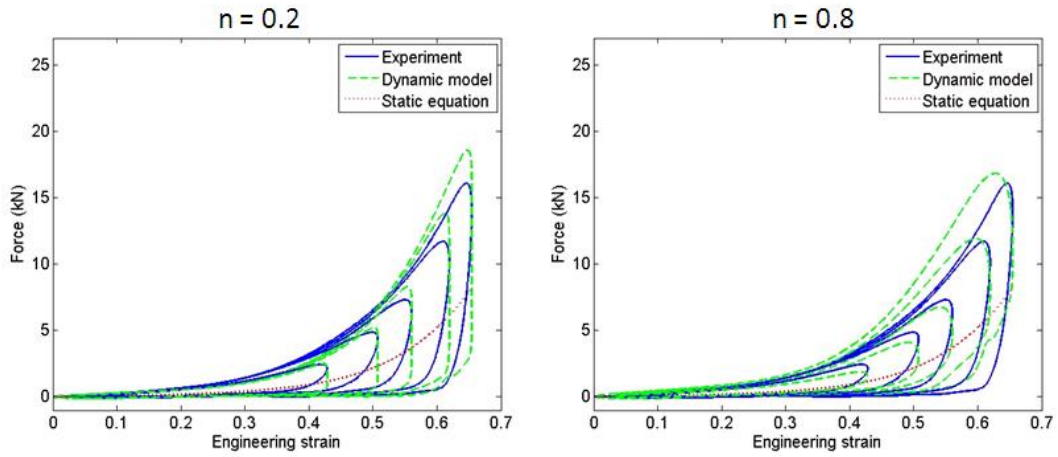

Figure 4-7 The effect of different power exponents (n=0.2 and n=0.8) in dynamic model with power-law strain-rate dependence of viscous term.

The effect of the reference engineering strain can be analyzed by pulling out the reference engineering strain-rate of power-law function in eq. (4.7), as shown in eq. (4.9).

$$F_{dynamic} = \frac{\eta_0}{\dot{\varepsilon}_{ref}{}^n} \cdot d \cdot K_s \cdot sign(\dot{x}) \cdot \left|\frac{\dot{x}}{d}\right|^n \qquad (4.9)$$

By doing this, $\frac{\eta_0}{\dot{\varepsilon}_{ref}{}^n}$ is treated as single parameter and the effect of changing reference engineering strain-rate is similar to the effect of changing dynamic force coefficient.

4.8 Dynamic Equation for O-ring Using Logarithmic Strain-Rate Dependence of Viscous Term

Based on the observation from experiment that strain-rate dependence on force is weaker than linear, using logarithmic function is another approach to explain the

phenomena. A new dynamic equation with logarithmic strain-rate dependence is proposed in eq. (4.10):

$$F(t) = F_{static} + F_{dynamic}$$

$$= \pi D_m d E_0 \left[1.25\left(\frac{x}{d}\right)^{3/2} + 50\left(\frac{x}{d}\right)^{6}\right]$$

$$+\pi D_m d \eta_0 \left[1.875\left(\frac{x}{d}\right)^{1/2} + 300\left(\frac{x}{d}\right)^{5}\right] \cdot sign(\dot{x}) \cdot \left[\log_{10}\left(\left|\frac{\dot{x}}{d}\right| / \dot{\varepsilon}_{ref}\right)\right] \quad (4.10)$$

For $\left|\frac{\dot{x}}{d}\right| < \dot{\varepsilon}_{ref}$, $F_{dynamic} = 0$

The nature of logarithmic function requires two modifications to the equation. First of all, logarithmic function can only deal with positive numbers. However, positive and negative strain-rate are both experienced by o-rings during the process of deformation and it's observed that positive strain-rate contribute to positive dynamic force and vice versa. For this reason, the absolute value of $\frac{\dot{x}}{d}$ is used inside the log function and the sign of strain-rate is pulled out of log to maintain the effect of positive and negative strain-rate. Secondly, log function of any positive number smaller than one is negative and log(1) =0. A reference state is chosen to correspond to zero strain-rate effect. If the absolute value of strain-rate is smaller than the reference state, the strain-rate effect equals to zero. Dividing the strain rate by the reference strain rata also make expression inside log function non-dimensional. Dynamic force coefficient η_0 may have different values for positive and negative strain-rate.

Figure 4-8 compares the model of dynamic equation with logarithmic strain-rate dependence using eq. (4.10) with experimental data. $\dot{\varepsilon}_{ref} = 10^0[s^{-1}]$, $E_0 = 10\ MPa$,

dynamic force constant $\eta_0 = 553\ KPa$ is used for both positive and negative strain-rate. This model matches with experimental data for impacting velocity ranging from V = 0.5m/s to V = 1.5m/s. By taking logarithm function on strain-rate, the model reflects the phenomena observed from experimental data that dynamic force is strongly affected by strain and weakly associate with strain rate. Another improvement from this model is that it better reflects the transition close to the maximum force of individual tests. By comparing with linear strain rate dependence model, the model using logarithmic strain-rate dependence describes experimental results better in the vicinity of the peak of each curve.

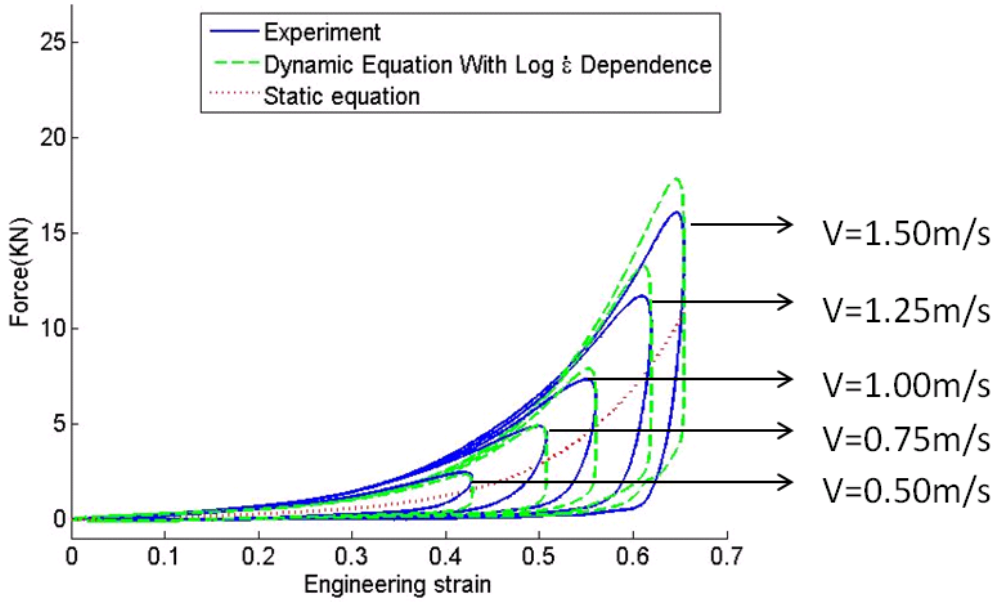

Figure 4-8 Comparison of dynamic equation with logarithmic strain-rate dependence of viscous term with dynamic test on Buna-N o-rings with velocity ranging from 0.5m/s to 1.5m/s.

From equation (4.10) and the non-linear stiffness equation of o-ring (eq.(3.2)), dynamic force can be expressed as following in eq. (4.11)

$$F_{dynamic} = \eta_0 \cdot d \cdot K_s \cdot sign(\dot{x}) \cdot \left[\log_{10}\left(\left|\frac{\dot{x}}{d}\right| / \dot{\varepsilon}_{ref}\right)\right] \qquad (4.11)$$

Eq. (4.11) represents dynamic force as a function of static stiffness and strain-rate. It demonstrates that dynamic force is proportional to static stiffness of o-ring (K_s), which is a function of engineering strain following double power law. Dynamic force is weakly related to engineering strain-rates due to logarithmic function.

Two parameters in eq. (4.10) need to be determined from experimental data: η_0, and $\dot{\varepsilon}_{ref}$. η_0 determines the dynamic force which is evaluated by the relative distance from the static curve in force - engineering strain relation. η_0 can be different with respect to positive and negative strain-rate and in our case a single constant can be used to explain the effect from both positive and negative strain-rate. The value of η_0 was chosen making sure that the sum of static and dynamic force wouldn't appear to be negative which would be a pulling force and couldn't be happening in an impact test.

Figure 4-9 showing results of using two reference strain-rates 10^{-5} and 10^{1} in dynamic model with logarithmic strain-rate dependence of viscous term. While the value of $\dot{\varepsilon}_{ref}$ changes, the value of η_{0+} and η_{0-} changes correspondingly to reflect experimental result. A larger reference strain-rate comes with larger dynamic force constants for both positive and negative strain-rate. A model with a smaller reference strain-rate shows a sharper change in the vicinity of the maximum force of each test. In a model with a smaller $\dot{\varepsilon}_{ref}$ at 10^{-5}, it reflects a smaller difference in dynamic force on the process of loading caused by different strain-rate. The loading curve with $\dot{\varepsilon}_{ref} = 10^{-5}$ overlap with each other while slight difference can be seen on loading curve with $\dot{\varepsilon}_{ref} = 10^{1}$.When raising $\dot{\varepsilon}$ from 100/s to 200/s at the same strain level, a 4.3% change

is predicted by a model with $\dot{\varepsilon}_{ref} = 10^{-5}$, and a 30% change is predicted by a model with $\dot{\varepsilon}_{ref} = 10^{1}$ as shown in eq. (4.12)

$$\frac{\log_{10}\left(\frac{200}{10^{-5}}\right) - \log_{10}\left(\frac{100}{10^{-5}}\right)}{\log_{10}\left(\frac{100}{10^{-5}}\right)} = 0.043$$

$$\frac{\log_{10}\left(\frac{200}{10^{1}}\right) - \log_{10}\left(\frac{100}{10^{1}}\right)}{\log_{10}\left(\frac{100}{10^{1}}\right)} = 0.30 \tag{4.12}$$

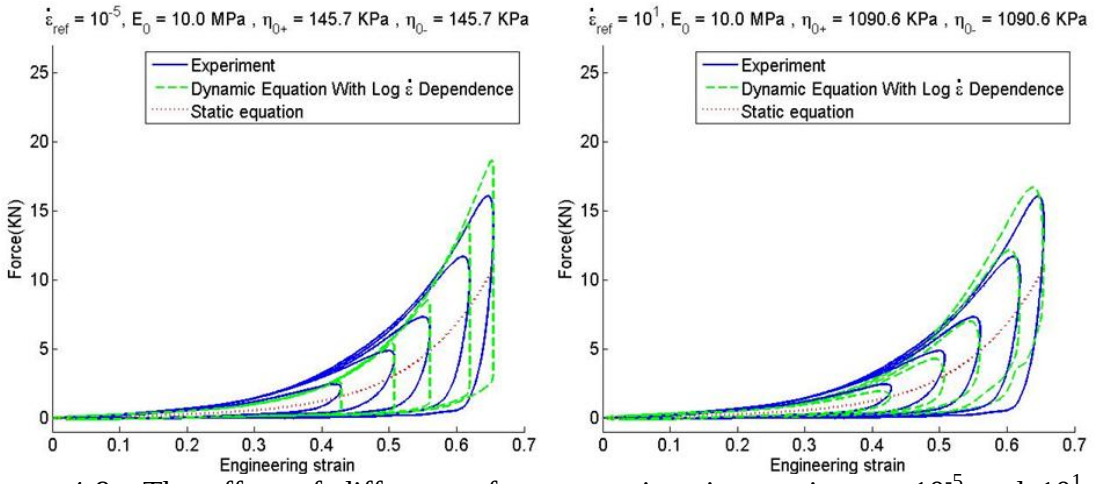

Figure 4-9 The effect of different reference engineering strain–rate 10^{-5} and 10^{1} in dynamic model with logarithmic strain-rate dependence of viscous term.

It's found that a reference strain-rate equals to 10^{0} fits experimental data better. This indicates that for engineering strain-rate smaller than 1/s or deformation velocity about 5 mm/s dynamic effect can be neglected.

The model does not perfectly match experimental results. This may be caused by uncertainty in measurement or the complexity of geometric and material properties of o-ring. Specifically, the model can't fit with unloading curve of each test with negative strain-rate. In the unloading phase, it's observed a slower drop in force in experiments

than predicted by a model with $\dot{\varepsilon}_{ref} = 10^0[s^{-1}]$ as shown in Figure 4-8. It's possible that experimental result can't be explained by the current states of strain and strain-rate alone. More complicated time dependent models caused by structure and material properties of o-rings can be a next step to explore if there're any models which can better describe the phenomena. The current model is good for the application of soft drop weight test when the loading curve can be used to predict change of o-ring height. The unloading curve is not used if recovery stage of the sample is not studied. However, in the case of energy dissipation in a chain of meta-material composed of o-rings with their multiple loading and unloading cycles, more complicated models may be desired for better accuracy.

4.9 Dynamic Models of O-rings with Initial Pre-Compression, Path Dependence of Dynamic Response

In most applications o-rings are used in precompressed state. In our experiments we used four pre-compression engineering strain levels - 4%, 25%, 40%, and 50% to observe its effect on the dynamic force strain relations. The corresponding results are presented in Figure 4-10 and Figure 4-11. The minimum static pre-compression strain in experiments with Buna-N o-ring (5mm cross section diameter) was 4%. It is caused by the weight of upper part of the holder of 16.7 N, which is much lower than maximum force even at lowest impact velocity 0.5 m/s (Figure 4-11). Thus the data for the initially prestrained o-ring with strain 4% can be considered as corresponding to no pre-compression case. Data with initial pre-compression strains 25%, 40%, and 50% were obtained using experimental approach described above. In experiments 3 minutes pre-compression time is used before

each impact tests based on independent measurements of o-ring behavior under quasistatic loading.

Figure 4-10 shows engineering strain rates over engineering strains for the tests corresponding to different precompression level and impact velocity 2.5 m/s. It demonstrates that the degree of the pre-compression does not significantly affect maximum strain-rates being around 100/s for most of the compression stage. Strain rate of each test quickly drops when it comes close to the corresponding maximum strain, which correspond to a sharp drop in force (see Figure 4-11). During the recovery stage, all tests with different pre-compression levels showed magnitude of the maximum rebounding strain-rate being close to 30/s.

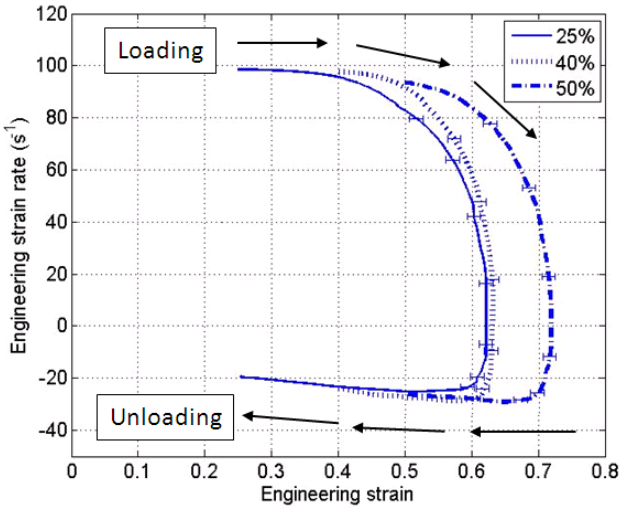

Figure 4-10 Dependence of engineering strain rates on engineering strains for Buna-N o-ring (5mm cross section diameter) with initial pre-compression 25%, 40% and 50% with identical conditions of impact with velocity 2.5 m/s.

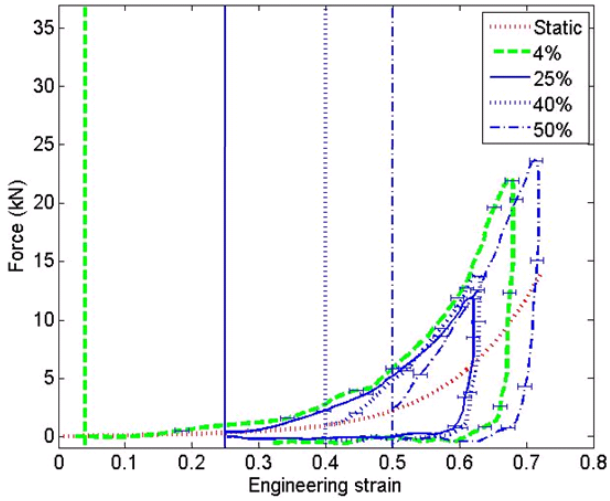

Figure 4-11 Experimental data on dynamic force versus engineering strain for Buna-N o-ring (initial outer diameter D = 20mm, mean diameter Dm = 15mm, diameter of circular cross section, d = 5mm) corresponding to different pre-compression levels indicated by corresponding vertical lines: 4%, 25%, 40%, and 50%. A static equation with E=7.6 MPa is shown by a dotted line.

Dependence of dynamic force on engineering strain at 4 different pre-compression levels (the corresponding strain rates are presented in Figure 4-10) are shown in Figure 4-11, together with static curve with E_0 = 7.6 MPa. It is important to mention that experimental data for weakly compressed o-rings (initial strain 4%) are providing envelope for all other data on the stage of loading.

As mentioned before the curve corresponding to 4% pre-compression is considered as a reference curve without pre-compression. Figure 4-11shows that o-rings with pre-compression strains 25%, 40%, and 50% exhibit weaker dynamic force than o-rings with lowest pre-precompression strain equal to 4%. It should be emphasized that the forces at the same strains 0.4 and 0.5 and different level of initial precompression (40% versus 25%) and (50% versus 25% and 40%) correspond to similar strain rates (see Figure 4-10). Thus observed difference (about 2 times) between forces at the vicinity of these initial strains corresponding to different levels of precompression can’t be attributed to the

difference in strains and in strain rates. This difference can only be attributed to the difference in deformation paths.

The difference in forces corresponding to initial precompression 4% and 40% decreases on later stages of deformation indicating that the pre-compression effect is transient and vanishes during continuous dynamic deformation.

The comparison of experimental results with the viscoelastic model using power law (eq. (4.6)) in shown in Figure 4-12. This model matches the experimental results only for 4% pre-compression. The predictions from the power law model for 40% and 50% precompression resulted in a similar curves for dynamic forces at a similar strain rates (Figure 4-10). But predictions based on this model significantly deviate from experimental results at the vicinities of the corresponding initial strains.

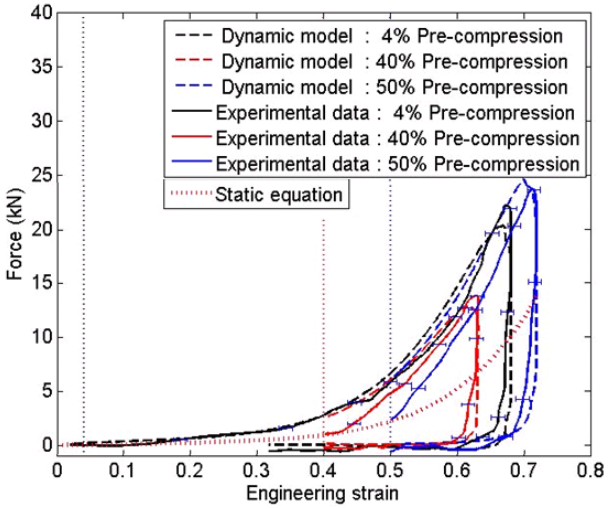

Figure 4-12 Dependence of force on engineering strain in experiments and in the model for Buna-N o-ring (initial outer diameter D = 20mm, mean diameter Dm = 15mm, diameter of circular cross section, d = 5mm). The pre-compression strains are indicated by corresponding vertical lines: 4%, 40%, and 50% (eq.(4.6)), which also correspond to the beginning of curves for dynamic forces in experiments (at corresponding points on the static curve) and in model (at points elevated vertically from the static curve). A static equation with E = 7.6 MPa is shown by a dotted line.

In order to explain the observed effect of pre-compression the model should reflect the pre-compression effect which is incorporated in the eq. (4.13). Equation (4.13) is proposed based on the observation that experimental curves corresponding to different levels of initial precompression start on the static curves, they do not experience a jump of force due to strain rate effects despite being dynamically deformed with strain rates about 10^2 s^{-1} (Figure 4-10). Thus we observe unusual phenomena that strain-rate effects in the beginning of deformation of prestressed o-rings were negligible. To account for this behavior in the proposed model we subtract a force corresponding to initial strain-rate and initial pre-compression strain expressed by last term in Eq. (4.13). Another experimental observation to be accounted by the model is a vanishing influence of initial precompression on the dynamic force at later stages of deformation. This phenomena was modeled by introduction of function *g(x)*, which negates influence of precompression after some critical dynamic strain, this critical strain ε_{cr} is a an additional parameter effectively introducing a loss of memory effect in a simplest form.

As a result this model predicts a force starting from static curve.

$$
\begin{aligned}
F(t) &= F_{static} + F_{dynamic} \\
&= \pi D_m d E_0 \times \left[1.25\left(\frac{x}{d}\right)^{3/2} + 50\left(\frac{x}{d}\right)^{6}\right] \\
&+ \pi D_m d \eta_0 \times \left[1.875\left(\frac{x}{d}\right)^{1/2} + 300\left(\frac{x}{d}\right)^{5}\right] \times sign(\dot{x}) \times \left(\left|\frac{\dot{x}}{d}\right| / \dot{\varepsilon}_{ref}\right)^{n} \\
&- \pi D_m d \eta_0 \times \left[1.875\left(\frac{x(0)}{d}\right)^{1/2} + 300\left(\frac{x(0)}{d}\right)^{5}\right] \times sign(\dot{x}(0)) \times \\
&\left(\left|\frac{\dot{x}(0)}{d}\right| / \dot{\varepsilon}_{ref}\right)^{n} \times g(x),
\end{aligned}
\tag{4.13}
$$

$$g(x) = \begin{cases} 1 - \frac{x - x(0)}{\varepsilon_{cr} d} & , if\ x < x(0) + \varepsilon_{cr} d\ \ \&\ \ \dot{x} > 0 \\ 0 & , if\ x > x(0) + \varepsilon_{cr} d\ \ or\ \ \dot{x} < 0 \end{cases}$$

A comparison between experimental result and the model using $\varepsilon_{cr} = 0.3$ is plotted in Figure 4-13. It shows that the dynamic model with correction for precompression effect matches satisfactory experimental results. It is also important that this model predicts force history of weakly compressed o-ring (initial strain 4%) on the stage of loading being an envelope for all other data in agreement with experiments.

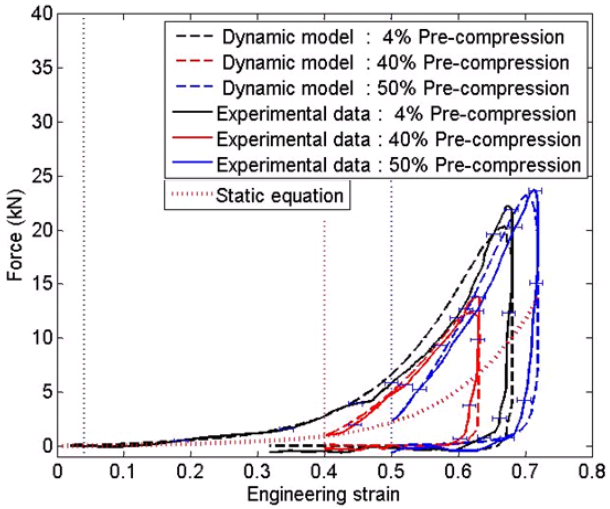

Figure 4-13 Dependence of force on engineering strain in experiments and in the model for Buna-N o-ring (initial outer diameter D = 20mm, mean diameter Dm = 15mm, diameter of circular cross section, d = 5mm). The pre-compression strains are indicated by corresponding vertical lines: 4%, 40%, and 50% (eq. (10)), which also correspond to the beginning of curves for dynamic forces in experiments and in the model (both curves start at corresponding points on the static curve). Static equation with E=7.6 MPa is shown by a dotted line.

The dynamic stiffness at the beginning of deformation can be derived by taking partial derivative of force (eq. (4.13)) with respect to displacement and is shown in eq. (4.14)

$$\left.\frac{\partial F(x)}{\partial x}\right|_{x=0} = \pi D_m E_0 \left[1.876\left(\frac{x(0)}{d}\right)^{1/2} + 300\left(\frac{x(0)}{d}\right)^{5}\right]$$

$$+\pi D_m \eta_0 \left[0.9375\left(\frac{x(0)}{d}\right)^{-1/2} + 1500\left(\frac{x(0)}{d}\right)^{4}\right] sign(\dot{x}(0))\left(\left|\frac{\dot{x}(0)}{d}\right|/\dot{\varepsilon}_{ref}\right)^{n} \quad (4.14)$$

$$+\pi D_m \eta_0 \left[1.875\left(\frac{x(0)}{d}\right)^{1/2} + 300\left(\frac{x(0)}{d}\right)^{5}\right] sign(\dot{x}(0))\left(\left|\frac{\dot{x}(0)}{d}\right|/\dot{\varepsilon}_{ref}\right)^{n} /\varepsilon_{cr} \ ,$$

Equation (4.14) demonstrates that dynamic stiffness is resulted from a combined effect from the static part of the force, dynamic part of the force and it is also influenced by a pre-compression strain. From the strongly nonlinear static elastic equation, we know that the stiffness of o-ring increases as strain increase. The power-law dynamic force indicated strain-rate dependence which is weaker than linear one. The effect of pre-compression observed from experiments demonstrated that the dynamic stiffness increases significantly faster than in static conditions with initial pre-compression at similar initial strains.

Table 4-1 Stiffness of o-rings predicted using static equation, dynamic equation with power-law model, and dynamic equation with pre-compression correction compared with average stiffness observed from experiment.

Stiffness (MN/m)	O-ring with 40% Pre-compression at Strain 40%, Strain-rate 100 /s.	O-ring with 50% Pre-compression at Strain 50%, Strain-rate 100 /s.
Static equation	1.5	3.8
Power-law model	4.2	10.1
Power-law model with pre-compression correction	5.1	12.5
Experiment (average stiffness)	4.8	13.0

The stiffness of o-rings at the beginning of the deformation process predicted using static equation, dynamic equation with power-law model, and power-law dynamic equation with pre-compression correction compared with average stiffness observed from experiment is summarized in Table 4-1. It shows that predictions based on the static equation dramatically underestimate the stiffness of prestressed o-rings. Incorporation of strain rate effects increases the stiffness. Results of a power-law model with pre-compression correction demonstrate the best agreement with the experimental data.

4.10 Conclusions

The strain-rate and precompression effect on dynamic behavior of o-rings is investigated using drop weight tests at the range of global strain up to 0.7 and strain rates about 100 s^{-1}. The dynamic stiffness of uncompressed o-rings increases about 3 times in comparison with predictions based on quasistatic compression data. This dramatic difference must be taken into account in the design of machinery when o-rings can be exposed to dynamic loading and in the design of metamaterials using o-rings as strongly nonlinear elements. Three dynamic models are analyzed to explain the dynamic behavior of uncompressed o-rings under impact conditions: (1) Dynamic model using linear strain-rate dependence based on Brilliantov et all [l5] and Morgado et all [l6] approach, (2) Dynamic model using linear strain-rate dependence with Hertz-damp method, and (3) Proposed dynamic model using power-law strain-rate dependence. All three models express dynamic forces as a function of strain-rates describing hysteresis and subsequent energy dissipation. Proposed dynamic model using power-law strain-rate dependence

satisfactory describes our experimental result for uncompressed o-rings in a broad range of impact velocity from 0.5 m/s to 1.5 m/s.

Dynamic behavior of o-rings at precompressions strains 4% and 2% is close to the behavior of uncompressed o-ring. Dynamic response at increased initial precompression to 40% and 50% demonstrated unexpected behavior with forces initially starting at values corresponding to the force prescribed by the static curve despite high strain rate deformation at given precompression strain. Dynamic forces in tests with 40% and 50% pre-compression at higher strains during deformation process approach the dynamic curve corresponding to a relatively small initial 4% pre-compression. This behavior clearly indicates a memory effect caused by initial static precompression which vanishes with continuing deformation. Power-law model incorporating memory effect from initial precompression using simple approach based on introduction of additional parameter - critical strain, successfully explain experimental results. This model predicts force history of weakly compressed o-ring (initial strain 4%) on the stage of loading being an envelope for all other data in agreement with experiments. Significant increase of dynamic stiffness of o-rings with the increase of initial precompression observed in experiments was successfully explained by proposed model.

Chapter 4 contains part of the material of a submitted paper “Path Dependent High Strain, Strain-Rate, Deformation of Polymer o-rings” in Journal of Applied Physics. The dissertation author was the primary investigator and author of this paper.

4.11 References

1. P. B. Lindley, (1966) "Load-compression relationships of rubber units." The Journal of Strain Analysis for Engineering Design, 1(3), 190.

2. P. B. Lindley, Jour. Inter. Rubber Inst., 1, 202, (1967).

3. A. Freidenberg, C.W. Lee, B. Durant, V. F. Nesterenko, L. K. Stewart, G. A. Hegemier, (2013) "Characterization of the Blast Simulator elastomer material using a pseudo-elastic rubber model." International Journal of Impact Engineering, 60, 58.

4. E. Herbold, and V. Nesterenko, (2007) "Solitary and shock waves in discrete strongly nonlinear double power-law materials." Applied Physics Letters 90, 261902.

5. P. Dias, A. Rosas, A. H. Romero, K. Lindenberg, (2010) "Pulse propagation in a chain of o-rings with and without precompression." Physical Review E 82, 031308.

6. A. Spadoni, C. Daraio, W. Hurst and M. Brown, (2011) "Nonlinear phononic crystals based on chains of disks alternating with toroidal structures." Applied Physics Letters 98, 161901.

7. Yichao Xu and V. F. Nesterenko, Phil Trans A. (in press).

8. V. F. Nesterenko, Dynamic of Heterogeneous Materials (Springer-Verlag, NY, 2011).

9. S. Sen, J. Hong, J. Bang, E. Avalos, and R. Doney,(2008) "Soliton-like waves in low-dimensional granular systems." Phys.Rep. N 462, 21.

10. J. Addiss, J. Cai, S. M. Walley, W. G. Proud, and V. F. Nesterenko, (2007) "Hign stain and strain-rata behaviour of PTFE/aluminuim/tungsten mixtures" in shock compression of compression of condensed matter- 2007, Proceedings of the Conference of the American Physical Society Topical Group on Shock Compression of Condensed Matter, edited by M. Elert, M.D. Furnish, R. Chau, N. Holmes, and J. Nguyen (American Institute of Physics), pp. 773-776.

11. E. B. Herbold, V. F. Nesterenko, D. J. Benson, J. Cai, K. S. Vecchio, and F. Jiang. (2008) "Particle size effect on strength, failure, and shock behavior in polytetrafluoroethylene-Al-W granular composite materials." Journal of Applied Physics 104.10: 103903.

12. P. Chiu, C. Lee, and V. Nesterenko, (2012) "Processing and dynamic testing of Al/W granular composites." in AIP Conference Proceedings, 1426, 737.

13. K. Olney, P. Chiu, C. Lee, V. Nesterenko, and D. Benson, (2011) “Role of material properties and mesostructure on dynamic deformation and shear instability in Al-W granular composites.” Journal of Applied Physics 110, 114908.

14. C. Lee, and V. Nesterenko, (2013) “Dynamic deformation of strongly nonlinear toroidal rubber elements.” Journal of Applied Physics, 144(8), 083509.

15. N. V. Brilliantov, F. Spahn, J.-M. Hertzsch and T. Poschel, (1996) “Model for collisions in granular gases.” Physical review E 53, 5382.

16. W. Morgado, and I. Oppenheim, (1997) “Energy dissipation for quasielactic granular particle collisions.” Physical Review E 55, 1940.

17. C. Daraio, V. Nesterenko, EB Herbold S. Jin, (2005) “Strongly nonlinear waves in a chain of Teflon beads.” Physical Review E 72.1: 016603.

18. C. Daraio, and V. F. Nesterenko. (2006) “Strongly nonlinear wave dynamics in a chain of polymer coated beads.” Physical Review E 73.2: 026612.

19. K. H. Hunt, and F. R. E. Crossley, (1975) “Coefficient of restitution interpreted as damping in vibroimpact.” ASME Journal of Applied Mechanics, 42, 440-445.

20. D. W. Marhefka, and D. E. Orin, (1999) “A compliant contact model with nonlinear damping for simulation of robotic systems.” IEEE Transactions on Systems, Man, and Cybernetics-Part A: System and Humans, 29, 566-572.

21. H. M. Lankarani ,and P. E. Nikravesh, (1990) “A contact force model with hysteresis damping for impact analysis of multibody systems.” Journal of Mechanical Design(ASME) 112, 369-376.

22. Susendar Muthukumar, and Reginald DesRoches, (2006) “A hertz contact model with non-linear damping for pounding simulation.” Earthquake Engineering and structural Dynamics, 35,811-828.

23. Panayiotis C. Polycarpou, Petros Komodromos, and Anastasis C. Polycarpou, (2013) “A nonlinear impact model for simulating the use of rubber shock absorbers for mitigating the effects of structural pounding during earthquakes.” Earthquake Engineering & Structural Dynamics 42.1: 81-100.

24. P. Allen, P. Lindley, and A. Payne, (1966) “Use of rubber in engineering “, Proceedings of a conference held at Imperial College of Science and Technology, London.

25. Mary C. Boyce, David M. Parks, and Ali S. Argon, (1988) “Large inelastic deformation of glassy polymers. Part I: rate dependent constitutive model.” Mechanics of Materials, 7.1 (1988): 15-33.

26. Ellen M. Arruda, Mary C. Boyce, and R. Jayachandran, (1995) “Effects of strain rate, temperature and thermomechanical coupling on the finite strain deformation of glassy polymers.” Mechanics of Materials 19.2: 193-212.

CHAPTER 5

SOFT DROP WEIGHT TESTS

5.1 Introduction

In conventional drop weight tests, high frequency noises excited from the impact between the drop mass and the target is unavoidable and high amplitude noise is always recoded in strain gauges signals [1, 2], Figure 1-1. If the characteristic frequency of the noise is significantly higher than the characteristic frequency of the useful signal, analog or digital low-pass filters can be used remove unwanted noise in real time or after signal recording [3, 4]. However, if a signal itself has high-frequency components, it will be improper to introduce any low pass filter to cut frequencies for signals of similar magnitude.

In order to improve the signal quality of conventional drop weight test, a "soft" drop weight test is proposed by introducing an extra layer of "soft" elements (e.g., rubber pads or o-rings) as force profiler. The material properties or geometry of "soft" elements in the design of an impact test can create desired ramping of loading force [5] and reduce unwanted excitations. "Soft" drop weight tests was successfully used in the dynamic tests of low strength samples of reactive materials [6, 7] and it is currently used for dynamic testing of Al-W composites [8]. The deformation of "soft" o-rings ramp the force applied to the sample reducing the excitation of high frequency components following abrupt change in signal during impact. The results showed significant improvement in

the quality of records from load cells or accelerometers in comparison with conventional drop weigh tests [1, 9, 10].

In a “soft” drop weight test presented in this chapter, two independent instruments can be used to record both forces acting on the top and bottom of the sample: one is an accelerometer mounted on the drop mass and another one is strain gauges placed in the supporting anvil beneath samples. The comparison between the two data is used to validate the assumption of force equilibrium in the sample under dynamic conditions. Once force equilibrium is proven in the sample during impact test, single force measurement can be used to represent the force acting in the samples. The signal quality from strain gauges shows better than the signal from accelerometers in terms of noise ratio and is used to represent the measured force. Additionally, the deformation of o-rings can is monitored using a high speed camera allowing synchronized and independent record of engineering strain with measurements of force and acceleration.

Instead of explicitly observe the strain data from high speed recordings, strain data can also be implicitly derived from force measurement. Engineering strain of the sample is influenced by 3 quantities during an impact test: the displacement of drop mass, the displacement of supporting structure, and the deformation of o-ring. The steps to derive these three quantities from force measurement are discussed in this chapter. Force measurement combined with Newton’s second law is used to derive the displacement of drop mass. A mass, spring and dashpot system is used to represent supporting structure and the displacement of supporting structure is derived by solving the finite difference equation. Dynamic models of o-ring discussed in Chapter 3 are used to interpret deformation of o-ring during impacting force condition.

A soft drop weight test presents better signal quality than conversional drop weight tests by utilizing the geometric and material properties of extra layer of soft materials. Force and engineering strain data of the sample can be derived solely from strain gauges measurement in a soft drop weight test. The technique allows us to estimate force over engineering curve without using a high speed camera. Soft drop weight test can be applied to study median strain-rate dependent deformation of low strength materials, e.g., low strength granular composites [11].

5.2 Experimental Setup

Soft drop weight tests are conducted using the configuration introduced in section 2.4. Annealed Al cylindrical samples with diameter 8mm and height 10mm ± 0.5mm was impacted by the drop mass with an initial velocity 4m/s ± 0.2m/s. One Buna-N o-ring with cross section diameter 5mm, inner diameter 10mm and mean diameter 15mm was placed above the upper piston to assist the soft drop weight test. During the tests, a high speed camera was set up to record the deformation of the sample and the deformation of the o-ring in separate tests. The results are compared to constitute a complete picture of soft drop weight tests.

Detailed data processing steps of the soft drop weight test is presented in this chapter. The procedures are written in MATLAB scripts to process data efficiently. The same procedures can be used to retrieve stress-strain relation of different samples under high strain-rate during impact tests.

5.3 Force Measurement and Signal Filtering

Voltage signals are generated by strain gauges and can be translated into force as

discussed in chapter 2.5. The output generated by strain gauges and recorded by a oscilloscope after applying a 3 KHz ideal low pass filter is shown in Figure 5-1 together with their corresponding periodogram. Data corresponds to a soft drop weight test with annealed Al cylindrical sample having initial diameter 8mm and height 10.1mm. Buna-N o-ring with diameter of cross section 5mm, inner diameter 10 mm and mean diameter 15mm was used. Drop mass had an initial velocity of 3.82m/s.

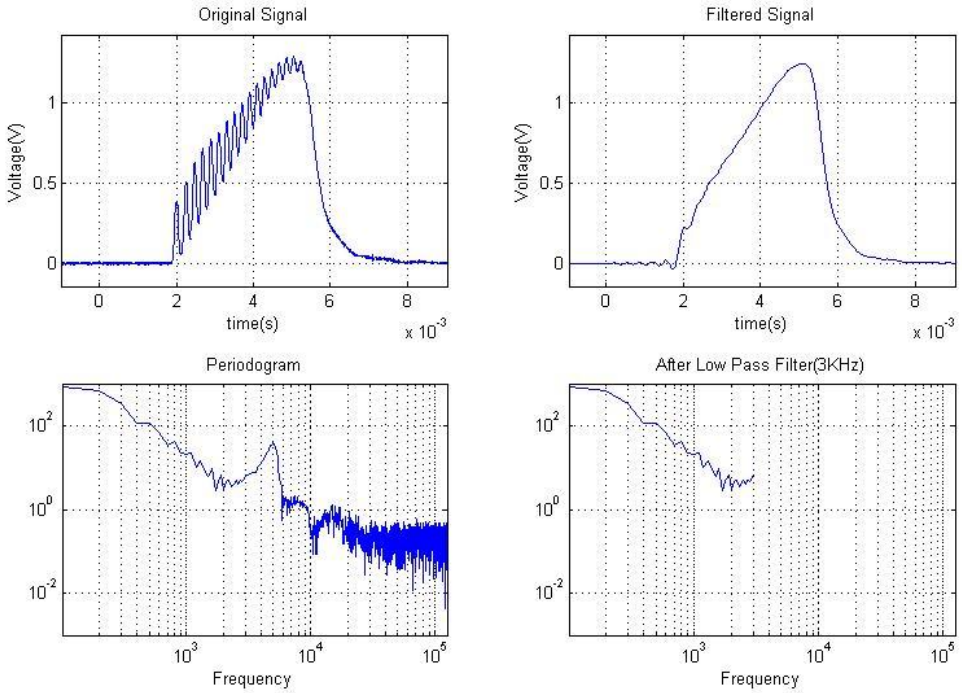

Figure 5-1 Voltage signal recorded by strain gauges, after filtering and their corresponding periodogram. Data corresponds to a soft drop weight test on annealed Al cylindrical sample with initial diameter 8mm and height 10.1mm. Buna-N o-ring with diameter of cross section 5mm, inner diameter 10 mm and mean diameter 15mm was used for softening of drop weight test. Drop mass had an initial velocity of 3.82m/s.

In the original signal, a resonant around 5 KHz is observed only in the loading phase from 2ms to 5ms when Al samples are deforming and not on the unloading phase after 5 ms. The oscillation can be caused by the vibrations of the sample or interaction between different components in the force chain. An ideal 3 KHz low pass filter is

applied to the signal to remove the oscillation and presented in the upper right figure of Figure 5-1.

5.4 Displacements of the Drop Mass, Upper Piston, and Change of O-ring Height

The high speed camera is set up to record the deformation of o-ring placed above upper piston during a soft drop weight test. The optical images are then processed by the image tracking algorithm introduced in chapter 2.7 and the displacement of the drop mass, the upper piston, and the o-ring can be derived.

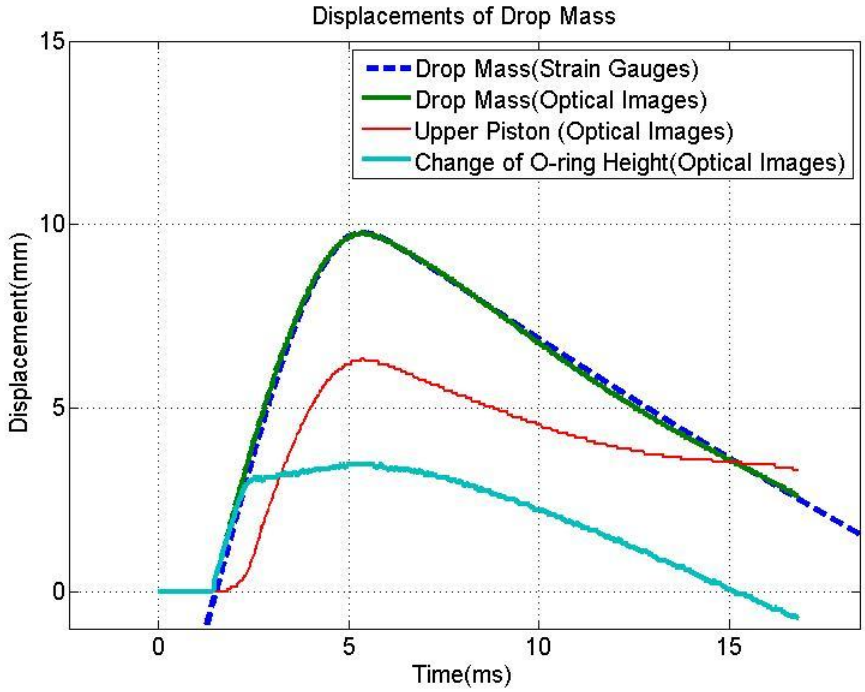

Figure 5-2 Displacement of drop mass, upper piston and change of o-ring height recorded in optical images by a high speed camera during a soft drop weight test. Theblue line is the displacement of drop mass derived from strain gauges.

The results are shown in Figure 5-2 which corresponds to a soft drop weight test on an annealed Al sample with initial height 10.1mm and initial diameter 8mm. Drop mass had an initial velocity 3.83m/s. A displacement of drop mass derived from strain

gauges measurement using the same procedures discussed in chapter 3.6 showing a perfect match with optical observation.

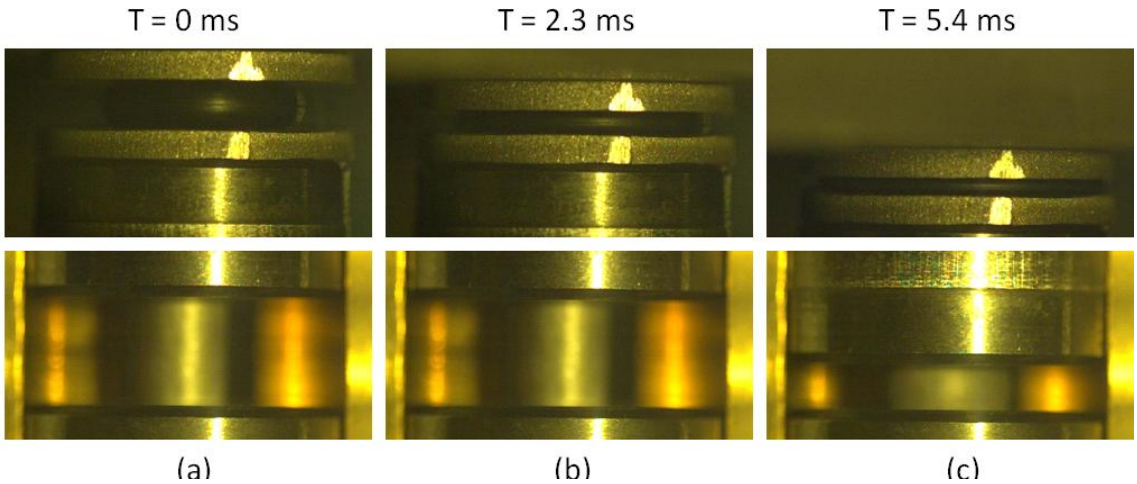

Figure 5-3 Optical images of the o-ring (top) and the Al 6061-0 sample (bottom) during soft drop weight tests. (a) Before impact. (b) Starting of impact, o-ring is compressed and the sample is only slightly deformed. (c) The maximum deformation of sample.

The tracking algorithm is used to capture the displacement of the drop mass and upper piston. The displacement of o-ring is derived by subtracting the displacement of upper piston from the displacement of the drop mass. By observing the curve corresponds to the change of o-ring height, it shows that most of the deformation of o-ring occurred during the initial contact with the drop mass. After the first deforming stage, the o-ring maintained at similar strain condition while the drop mass continues to deform the Al sample. The optical images of the o-ring and the sample in different stages of the testing are plotted in Figure 5-3.

Knowing the force recorded by strain gauges, the displacement of o-ring can be derived using equations discussed in the previous chapters. The displacement of o-ring in Figure 5-2 derived from optical images is compared with the displacement of o-ring derived from static equation (eq. (3.1)), dynamic equation using Brilliantov's model (eq.

(3.5)), and dynamic equation using power law model (eq. (4.6)) in Figure 5-4. It shows that the corresponding displacement from the static equation deviates from the optical result the most, especially after 5ms when the force start to drop. The static equation don't take strain-rate effect in account and the deformation of o-ring quickly drop back to zero as the force drop while in fact the o-ring gradually recover from the compressed state showing the viscoelastic character.

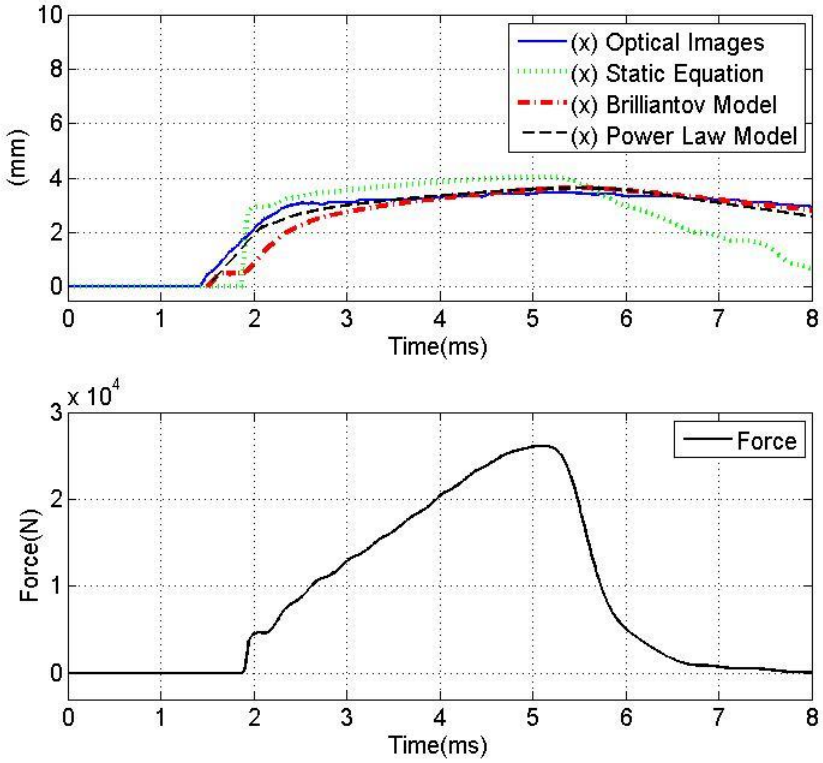

Figure 5-4 Displacement of the o-ring observed from optical images compared with displacement of the o-ring derived from static equation (eq. (3.1)), dynamic equation using Brilliantov's model (eq. (3.5)), dynamic equation using power law model (eq. (4.6)), and corresponding force recorded by strain gauges.

Both dynamic equations using approach based on modified Brilliantov's model and power law model predict the displacement of o-ring very well. The former model underestimates the displacement by about 1mm from 1.5 to 3ms during the loading phase.

This is reflects the same observation in chapter 4 that dynamic model based on modified Brilliantov's approach would overestimate the force while increasing strain-rate. The nominal engineering strain-rate in this test with initial velocity 3.83 m/s is 765/s which is higher than the strain-rate with impact velocity about 1m/s. It demonstrates that the weaker than linear strain-rate dependence need to be used to improve the accuracy of the model. The dynamic model using power law strain-rate dependence matched with the deformation of o-ring observed from optical images the best. It successful describes the loading path, the maximum strain and the unloading path.

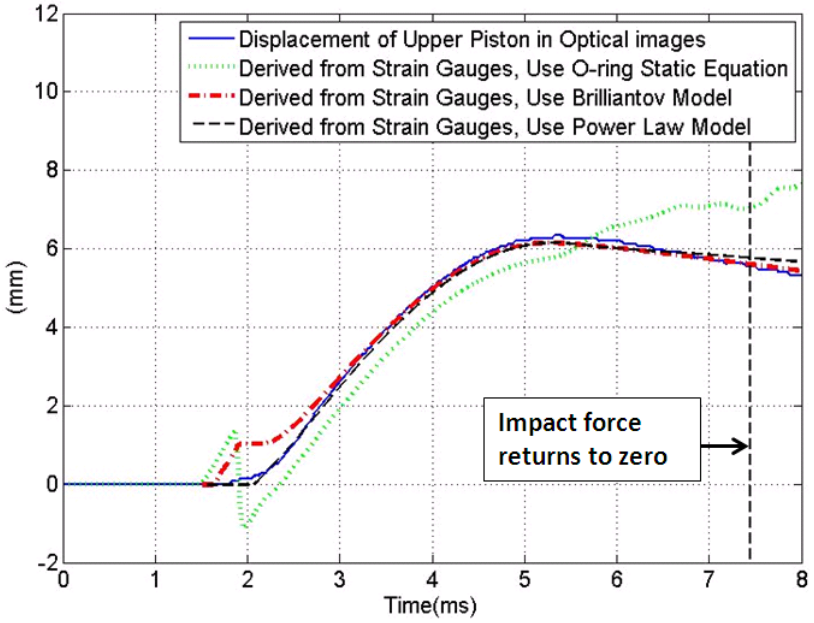

Figure 5-5 Displacement of the upper piston observed in optical images compared and derived solely from strain gauges. Deformation of o-ring was calculated using static equation, dynamic equation using Brilliantov's model, and dynamic equation using power law model.

Displacement of the upper piston can be observed in optical images or be derived by subtracting change of o-ring height from displacement of the drop mass. It's shown that change of o-ring height can be derived using strain gauges measurement and

different o-ring deformation models. It's also known that displacement of the drop mass can be derived by force measurement by strain gauges. Together displacement of the upper piston can be derived solely from strain gauges measurement. Displacement of the upper piston observed in optical images and derived solely from strain gauges measurement using three o-ring deformation models is shown in Figure 5-5. The three models are the same as discussed in Figure 5-4. It's shown that displacement of upper piston derived from strain gauges using power law model match well with optical observation.

5.5 Dynamic Strains in the Sample

Change of sample's height can be calculated by subtracting the displacement of the supporting structure from the displacement of upper piston and the result is shown in Figure 5-6. Base movement is derived using force measured by strain gauges and the equation modeling displacement of the base (eq. 2.4) discussed in chapter 2-8.

The deforming history of an annealed Al sample during a soft drop weight test is shown in Figure 5-6. The engineering strain-rate is estimated by the slope of the curve. Engineering strain-rate of Al gradually increased at the beginning of the deformation from 1.5 to 2.5 ms, while o-ring started to deform and ramped the contacting force to reduce unwanted noise. The major deformation of Al sample took place during 2.5 to 4.5 ms at a consistent rate about 3m/s, which corresponds to an engineering strain rate 300/s. The deformation finished when the sample reached its minimum height of 5.8mm at 5.4 ms and slightly rebounded by 0.2mm during compression time from 5.4 ms to 7.4 ms. The deforming history of an annealed Al sample shows that the soft drop

weight test can be easily used to achieve high strain with moderate strain-rate test (10^2/s to 10^3/s).

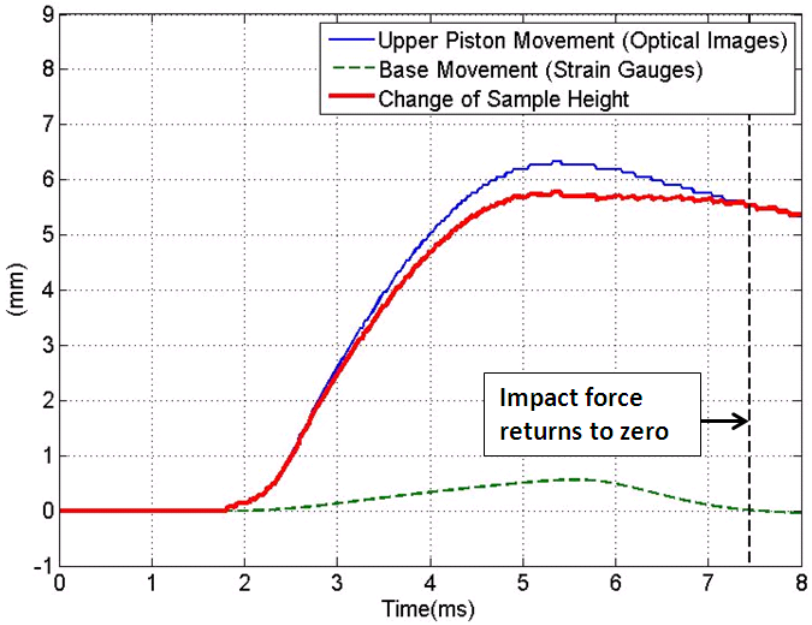

Figure 5-6 Displacement of upper piston observed in optical images and base movement derived from strain gauges measurement. Displacement of the sample is calculated using correction for base movement from the displacement of upper piston.

Change of sample's height can be derived from optical observation or solely from strain gauges measurement. Figure 5-7 compare the result observed in optical images and derived solely from strain gauges. It's shown that the strain data of the sample during a soft drop weight test can be derived from strain gauges measurement using the power law model.

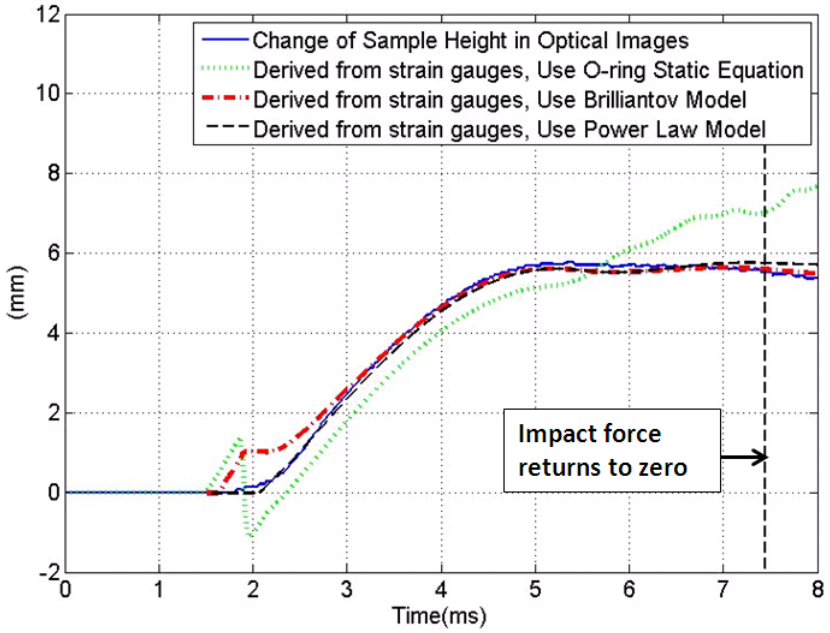

Figure 5-7 Change of sample's height observed in optical images compared and derived solely from strain gauges. Deformation of o-ring was calculated using static equation, dynamic equation using approach based on modified Brilliantov's model, and dynamic equation using power law model.

Change of Al sample's height from optical images and strain gauges measurement translated to engineering strain. Force over engineering strain of an annealed Al sample in a soft drop weight test is shown in Figure 5-8.

True strain of Al sample is derive from engineering strain and force versus true strain is shown in Figure 5-9. Assuming constant volume, true stress can be derived by eq. (2.10). True stress over true strain of the annealed Al sample is shown in Figure 5-10.

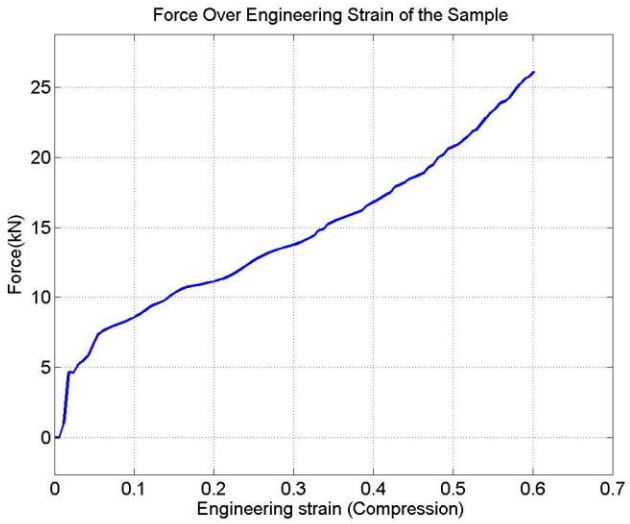

Figure 5-8 Force versus engineering compression strain of an annealed Al sample during a soft drop weight test. Data corresponds to a soft drop weight test on annealed Al cylindrical sample with initial diameter 8mm and height 10.1mm. Buna-N o-ring with diameter of cross section 5mm, inner diameter 10 mm and mean diameter 15mm was used. Drop mass had an initial velocity of 3.82m/s.

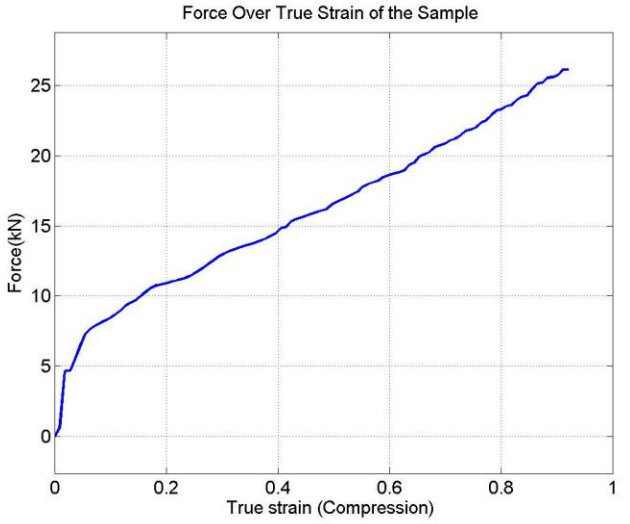

Figure 5-9 Force versus compression true strain of an annealed Al sample during a soft drop weight test. Data corresponds to a soft drop weight test on annealed Al cylindrical sample with initial diameter 8mm and height 10.1mm. Buna-N o-ring with diameter of cross section 5mm, inner diameter 10 mm and mean diameter 15mm was used. Drop mass had an initial velocity of 3.82m/s.

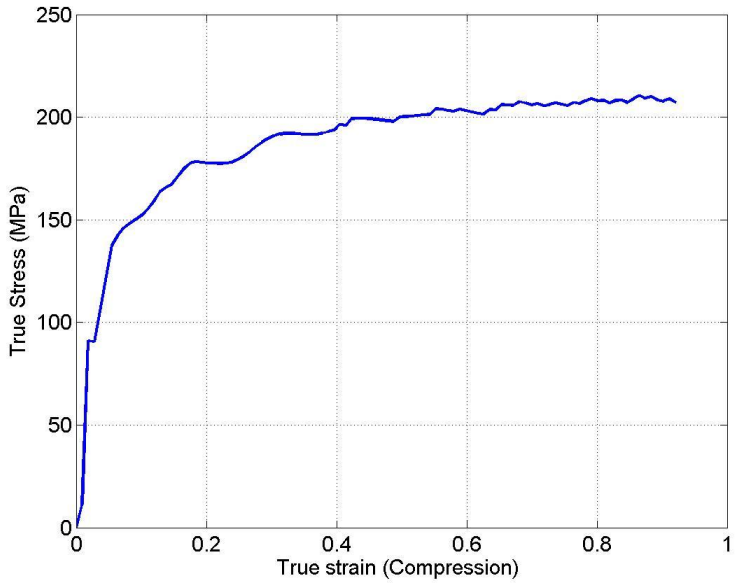

Figure 5-10 True stress versus true strain of an annealed Al sample during a soft drop weight test. Data corresponds to a soft drop weight test on annealed Al cylindrical sample with initial diameter 8mm and height 10.1mm. Buna-N o-ring with diameter of cross section 5mm, inner diameter 10 mm and mean diameter 15mm was used. Drop mass had an initial velocity of 3.82m/s.

It's shown that the annealed Al sample had linear range from 0 to 0.5% strain. The yield strength was at about 100 MPa and slight strain hardening effect can be observed as strain increase. Same procedures can be easily applied on low-strength compound material or polymers to study the effect of strain-rate acting on structure material under high strain deformation and moderate strain-rate using soft drop weight device.

More details of testing results on Aluminum 6061-0, Aluminum 6061-T6, Al/W CIPed and HIPed samples, and polyurethane using soft drop weight tests are discussed in Chapter 6.

Chapter 5 contains material currently being prepared for publication of "Soft drop weight tests of low strength materials." The dissertation author was the primary investigator and author of this material.

5.6 References

1. S. M. Walley, D. J. Chapman, D. M. Williamson, M. J. Morley, T. W. Fairhead, and W. Proud, (2009) "High rate mechanical properties of Dyneema in compression." Proceedings of DYMAT, 1133.

2. W. G. Proud, D. Porter, P. J. Gould, D. M. Williamson and S. M. Walley, (2010) "The Mechanical Performance of Polymers and Polymer Composites." in Proceedings of IMPLAST 2010 conference, Rhode Island, USA, October 12-14 2010, Society for Experimental Mechanics, Inc.

3. E. H. Wong, C. Selvanayagam, S. Seah, W. Van Driel, J. Caers, X. Zhao, N. Owens, L. Tan, D. Frear, M. Leoni, S. Y, and C.L. Yeh, (2008) Journal of Electric Materials 37, 829.

4. W. G. Proud, S. M. Walley, D. M. Williamson, A. L. Collins, and J. W. Addiss, (2009) "Recent trends in research on energetic materials at Cambridge." Central European Journal of Energetic Materials 6, 67.

5. A. Freidenberg, C.W. Lee, B. Durant, V. F. Nesterenko, L. K. Stewart, G. A. Hegemier, (2013) "Characterization of the Blast Simulator elastomer material using a pseudo-elastic rubber model." International Journal of Impact Engineering, 60, 58.

6. J. Addiss, J. Cai, S. M. Walley, W. G. Proud, and V. F. Nesterenko, (2007) "High stain and strain-rata behaviour of PTFE/aluminuim/tungsten mixtures" in shock compression of compression of condensed matter- 2007, Proceedings of the Conference of the American Physical Society Topical Group on Shock Compression of Condensed Matter, edited by M. Elert, M.D. Furnish, R. Chau, N. Holmes, and J. Nguyen (American Institute of Physics), pp. 773-776.

7. E. B. Herbold, V. F. Nesterenko, D. J. Benson, J. Cai, K. S. Vecchio, and F. Jiang. (2008) "Particle size effect on strength, failure, and shock behavior in polytetrafluoroethylene-Al-W granular composite materials." Journal of Applied Physics 104.10: 103903.

8. K. Olney, P. Chiu, C. Lee, V. Nesterenko, and D. Benson, (2011) "Role of material properties and mesostructure on dynamic deformation and shear instability in Al-W granular composites." Journal of Applied Physics 110, 114908.

9. D. Radford, S. Walley, P. Church, J. Field, (2003) "Dynamic upsetting and failure of metal cylinders: Experiments and analysis" in Journal de Physique IV (Proceedings), Vol. 110 pp. 263-268.

10. J. Field, S. Walley, and W. Proud, H. Goldrein, and C. Siviour, (2004) “Review of experimental techniques for high rate deformation and shock studied.” International Journal of Impact Engineering 30.7, 725.

11. V. F. Nesterenko, P. Chiu, C. H. Braithwaite, A. Collins, D. M. Williamson, K. L. Olney, D. J. Benson, and F. McKenzie, (2012) “Dynamic behavior of particulate/porous energetic materials.” in AIP Conference Proceedings, Vol. 1426, p.533.

CHAPTER 6

EXAMPLE APPLICATIONS OF SOFT DROP WEIGHT TESTS ON LOW STRENGTH MATERIALS

6.1 Verification of Soft Drop Weight Tests Using Well Characterized Materials Al 6061-T6 and Al 6061-0

Aluminum alloys are widely used in industry and their dynamic properties under various strain conditions are available [1-4]. Al 6061-T6 and Al 6061-0 cylinder samples are tested to verify the stress-strain measurement and data processing methods used in soft drop weight tests discussed in Chapter 5. The testing conditions of Aluminum 6061-0 and Aluminum 6061-T6 are listed in Table 6-1. 4 Tests are labeled from Al-1 to Al-4 with variation in material types and impact velocities. Repeatability of soft drop weight tests can be verified by applying the same testing conditions on Al 6061-0 (Al-1, Al-2). The effect of sample's strength on signal recording is compared by hitting Aluminum 6061-0 (Al-2) and Aluminum 6061-T6 (Al-3) with the same impact velocity 4m/s. The strain-rate effect on Al 6061-0 is demonstrated by doubling the impact velocity from 4m/s (Al-1) to 8m/s (Al-4) using soft drop weight test.

The voltage signals generated by strain gauges, amplified by an amplifier and recorded by an oscilloscope in Al-1 and Al-2 are presented in Figure 6-1. Time axis are adjusted for each recording such that "Time=0" corresponds to the moment when voltage signal started to change. Testing configuration discussed in chapter 2.4 was used and one Buna-N o-ring with diameter of cross section 5mm, inner diameter 10mm, and outer

diameter 20mm was placed on the top of upper piston to assist with the soft drop weight tests. The testing conditions of Al-1 and Al-2 are designed to be the same to confirm the repeatability of soft drop weight test. Al 6061-0 was tested with impact velocity 4m/s. There's only slightly difference in the height of two samples which might be the reason there's still a little difference observed measurement.

Table 6-1 Testing conditions of Aluminum 6061-0 and Aluminum 6061-T6 cylinder samples.

Test ID	Al-1	Al-2	Al-3	Al-4
Material Type	Al6061-0	Al6061-0	Al6061-T6	Al6061-0
Impact Velocity(m/s)	4.0	4.0	4.0	8.0
Original Height(mm)	10.1	9.75	9.6	10.1
Final height(mm)	4.35	4.10	6.50	1.70
Original Diameter(mm)	8	8	8	8
Engineering strain (Compression)	56.9%	57.9%	32.3%	83.2%
True strain (Compression)	0.84	0.86	0.39	1.78

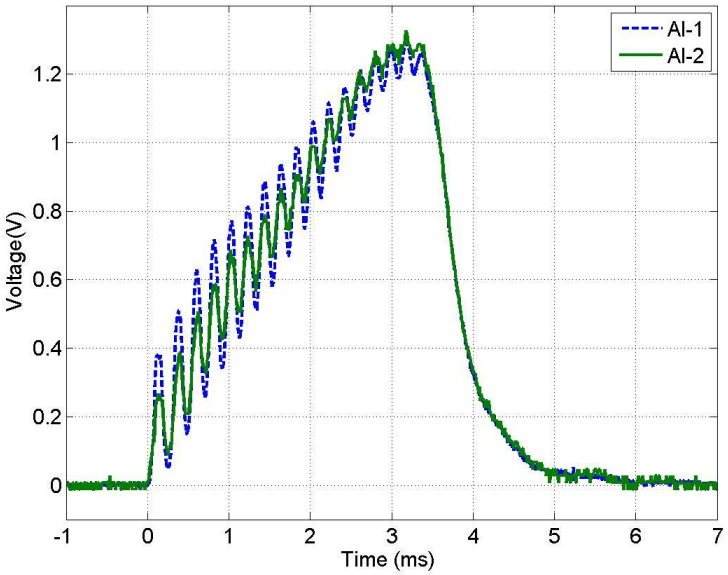

Figure 6-1 Electric signals generated by strain gauges in two soft drop weight tests Al-1 and Al-2. In both tests samples of Al 6061-0 were dynamically deformed with impact velocity 4m/s.

The engineering strain of samples after soft drop weight tests Al-1 and Al-2 are very similar as listed in Table 6-1 at about 57%-58%. From Figure 2-2 it shows that the signals from strain gauges are almost identical. In a soft drop weight test, the usage of o-rings reduced the embedded noise but ringing effect can still be observed on the loading stage. The dominant frequency of the noise is around 5KHz. It's suspected that this noise comes from a bending mode of upper piston which is excited from impact of drop mass. Both recordings followed the same path and Al-1 exhibit higher oscillation level on the loading path.

An ideal low pass filter with cutoff frequency 3KHz was applied on both signals to remove unwanted noise similar to the method discussed in chapter 2.6. The voltage signals can then be translated into force using eq. 2.1 and the force acting on the sample over time is shown in Figure 6-2. After filtering, the signals from the two tests look almost identical. The maximum force in Al-2 is slight greater than that of Al-1. This reflects the observation that Al-2 has slightly higher engineering strain after the test which would have been caused by slightly higher force. Aside from slightly different maximum force, the two force history curve overlap on each other in the whole impacting event.

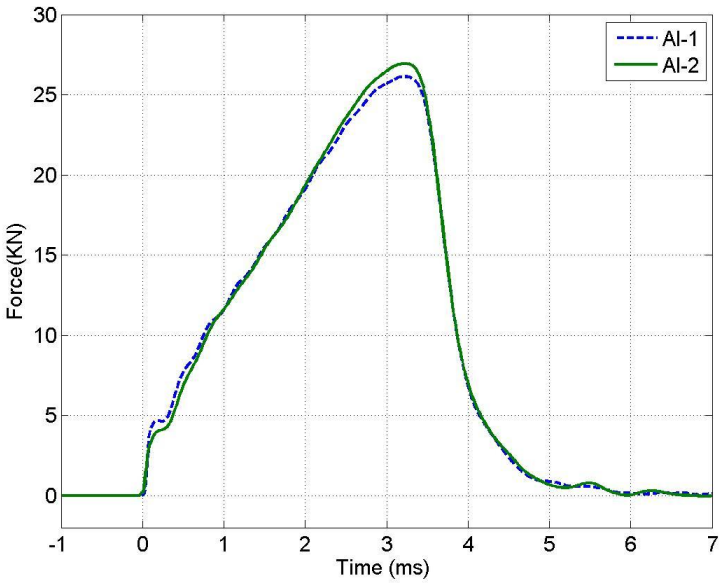

Figure 6-2 Force verses time of soft drop weight tests Al-1 and Al-2. Data corresponds to samples of Al 6061-0 impacted by 4 m/s.

The strain data of the sample is translated from videos recorded by a high speed camera using image tracking algorithm discussed in 2.7. The accuracy of this method is 1 pixel size which was set to 0.07mm in the video recording the deformation of Al 6061-0 sample during impact tests. True compression stain of Al sample is derived from engineering strain using eq. (2.7). True stress over true strain of Al-1 and Al-2 is plotted in Figure 6-3 together with existing stress-strain relation of Al 6061-0 derived using Hopkinson Split Pressure Bar [4]. The similarity between Al-1 and Al-2 shows that the measurements from soft drop weight tests are repeatable. The comparison with existing data suggests that soft drop weight tests can be used to observe high-rate stress-strain properties of the sample. It can further provide data on high-strain-rate behavior which was not easily accessible using Hopkinson Split Pressure Bar. From the result it suggests that Al6061-0 has flow stress of 200 MPa at true strain 0.4 and 210 MPa at strain 0.8. Slightly work hardening is observed in the measurement.

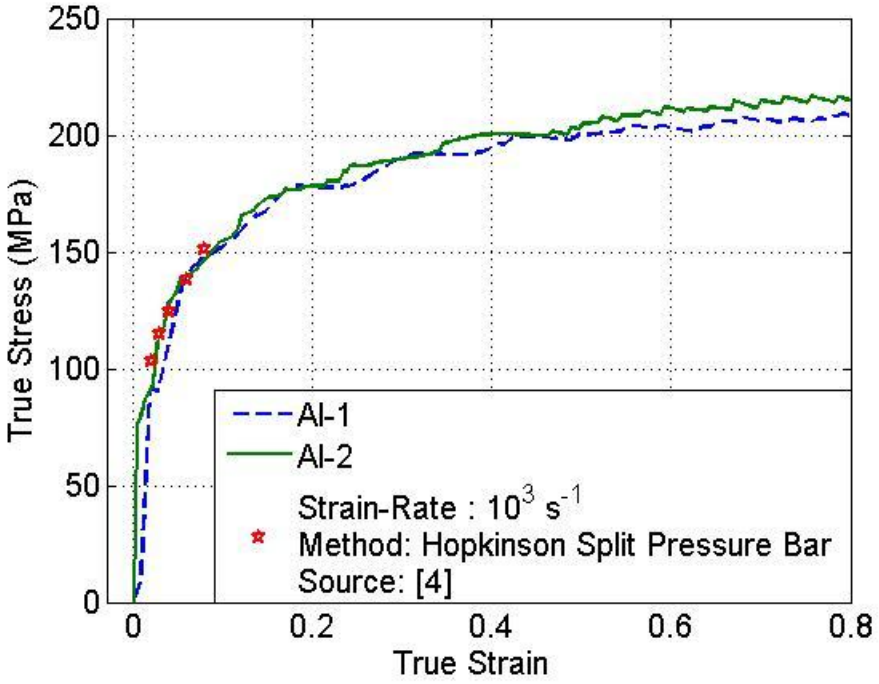

Figure 6-3 True stress versus compression true strain in Al-1 and Al-2 tests compared with data for Al 6061-0 measured by the Hopkinson Split Pressure Bar under strain rate 10^3 [4]

The mechanical properties including yielding strength, elastic modulus, and flow stress of the sample would affect force in soft drop weight tests. Figure 6-4 shows the force over time of Al-2(Al6061-0) and Al-3(Al6061-T6). Both are tested using soft drop weight tests with impact velocity 4m/s corresponds to a nominal strain-rate 400 s^{-1}. Signals were filtered with an ideal low pass filter with cutoff frequency 3 KHz. Starting from the initial of the impact, two curves overlapped on each other reflects the fact that elastic modulus of Al6061-0 and Al6061-T6 is the same. Al6061-0 has a lower yielding stress and departs from the initial linear increase of the force and started plastic deformation earlier. Responding to the same impact velocity, it's shown that Al-3 exhibit higher force value from 0.1 ms to 3 ms. Al-2 experienced longer impacting time and larger deformation. The area beneath each curve equals to integrating force over

time corresponds to the momentum exchanged during the impact test. The area of Al-3 is 70.0 N·s and is higher than the area of Al-2 is 69.0 N·s indicating that the drop mass had higher rebounding velocity in Al-3 than in Al-2 after the impact testing.

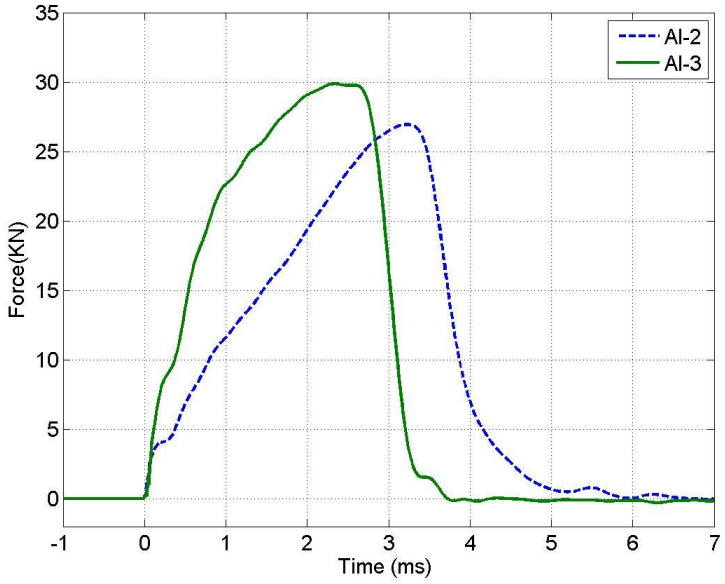

Figure 6-4 Force versus time in tests Al-2 (Al-6061-0) and Al-3 (Al-6061-T6). Both samples were tested using soft drop weight tests with impact velocity 4m/s.

The high speed camera was used to record sample's deforming history and the strain data of the Al sample is derived by observing the difference in the displacement of upper and lower pistons. The displacement of upper and lower pistons of Al-2 and Al-3 during soft drop weight tests is shown in Figure 6-5. Data is derived from optical images recorded by the high speed camera with frame rate 40,000 frames per second. Time zero corresponds to the moment when force started to rise and it is the synchronized with Figure 6-4. By comparing the displacement of upper piston in Al-2(Al6061-0) and Al-3(Al6061-T6) it shows that Al6061-0 started to deform earlier than Al6061-T6. The ramping of the signal in the beginning of the deformation of both curves is the characteristic of the soft drop weight test where o-ring ramps the impacting force and

reduced excitation of the noise in strain gauges measurement. After a short encounter stage, two curves increase to their maximum displacement with consistent strain-rate. The displacement of lower pistons is small comparing to that of upper piston. The maximum displacement of lower piston in Al-3 is slightly greater than that in Al-2. The optical images allow us to observe strain history with accuracy up to 1 pixel size.

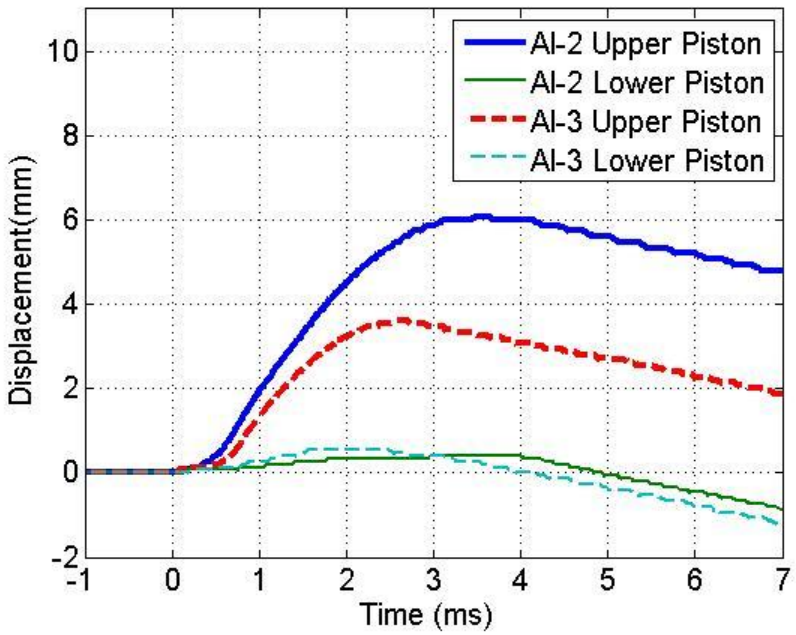

Figure 6-5 The displacement of upper and lower pistons in Al-2(Al6061-0) and Al-3(Al6061-T6) in soft drop weight tests with impact velocity 4m/s. Data were derived from optical images.

The true stress over true strain of Al-2 and Al-3 is shown in using the strain data derived from optical images and force data from strain gauges. The stress-strain relation of Al6061-0 and Al6061-T6 is compared with data reported in literature using Hopkinson Split Pressure Bar (HSPB) [1, 4]. The data derived using soft drop weight tests matches with data derived from HSPB very well. It shows that Al6061-T6 has a yielding strength at 300 MPa and flow stress at more than 400 MPa under a nominal strain-rate 400 s^{-1} using a soft drop weight test. The flow stress of Al6061-T6 is about 2 time

higher than Al6061-0.

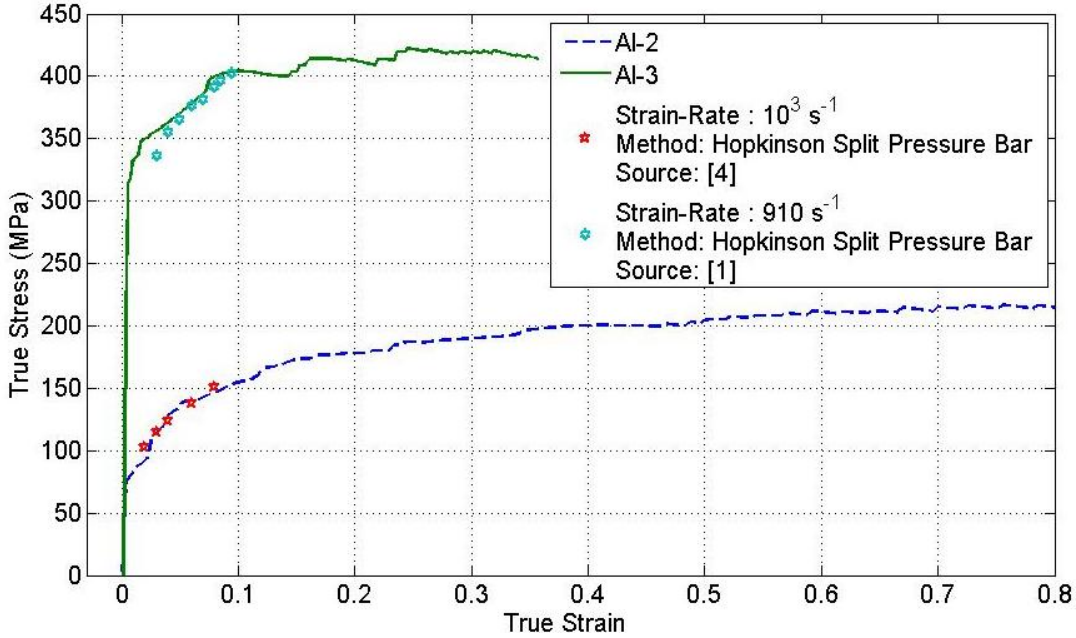

Figure 6-6 True stress versus true strain for tests Al-2(Al6061-0) and Al-3(Al6061-T6) measured in soft drop weight tests compared with Al 6061-T6 tested by the Hopkinson Split Pressure Bar under strain rate 910 s^{-1} [1] and Al 6061-0 tested by the Hopkinson Split Pressure Bar under strain rate 10^3 s^{-1}[4].

The effect of impact velocity during soft drop weight tests is compared by impacting Al6061-0 with two different velocities. The force over time data of Al-6061-0 samples during soft drop tests is shown in Figure 6-7. A 3 KHz ideal low pass filter is applied on both signals. It shows that the force condition for Al-2 is relatively smother.

The stress-strain curves of Al-2 and Al-4 tested using soft drop weight tests and Al 6061-0 tested by the Hopkinson Split Pressure Bar under strain rate 10^3 $s^{-1}$are compared in Figure 6-8. The impact velocity of Al-2 was set to 4m/s corresponds to a strain-rate of 400 s^{-1}. Al-4 was tested with 8m/s and the nominal strain-rate was 800 s^{-1}. The yielding stress of Al-2 was observed at 100MPa while the Al-4 exhibited a stronger

yielding point at 150 MPa. The observation shows that strain-rate does affect reactive force of Al6061-T6-0 samples. Under the same strain, the flow stress of Al-4 is greater than Al-2.

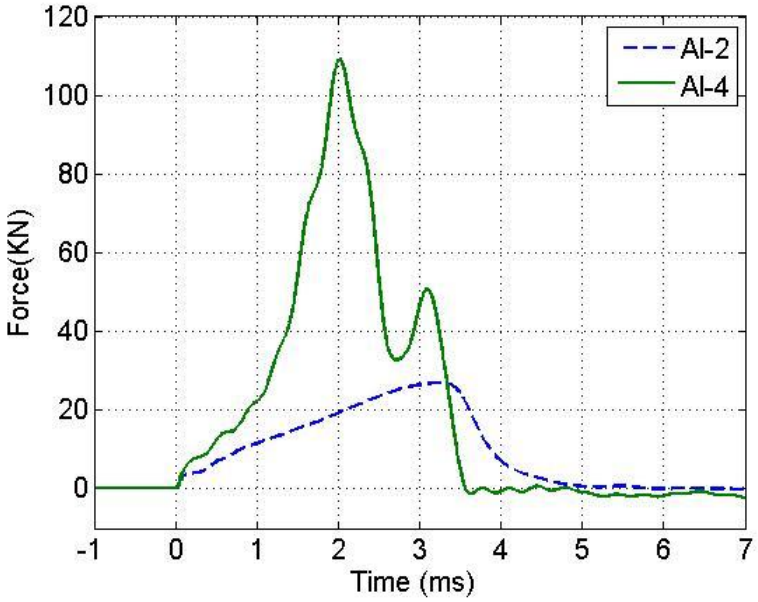

Figure 6-7 Force versus time for Al-6061-0 samples in soft drop weight tests. The impact velocity was 4m/s for Al-2 and 8m/s for Al-4.

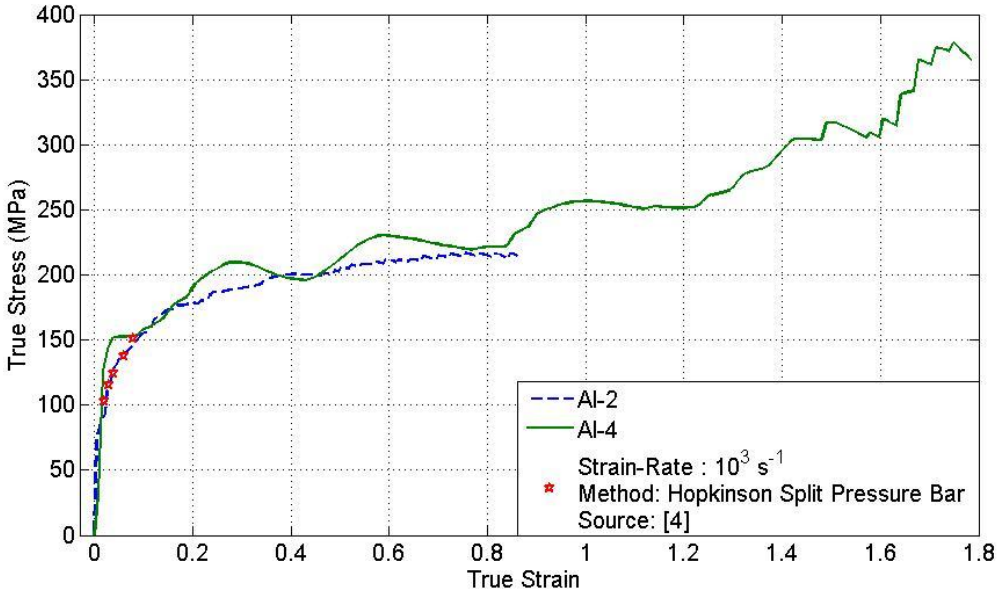

Figure 6-8 True stress versus true strain of Al6061-0 measured in soft drop weight tests compared with data of Al 6061-0 tested by the Hopkinson Split Pressure Bar under strain rate 10^3 s^{-1}[4]. The impact velocity was 4m/s for Al-2 and 8m/s for Al-4.

6.2 Soft Drop Weight Tests of Adiprene L-100

The soft drop weight test is ideal for the testing of polymer. Adiprene L-100 elastomer is used in hydraulic rams, which is an important component of the UCSD Blast Simulator tailor impulsive load. In order to construct the strain-rate dependent material properties of the polymer, soft drop weight tests are applied on cylindrical Adiprene L-100 samples. In LS-DYNA, strain-rate related material properties are be used to account for energy absorption of damping mechanism. The testing conditions are classified in Table 6-2 with impact velocities 0.65 m/s , 1m/s, and 2m/s. In all the tests, an o-ring with cross section diameter 1.78 mm, mean diameter 6.22 mm was used on top of the upper piston to assist with the soft drop weight test.

Table 6-2 Testing conditions of Adiprene L-100 cylinder samples.

Test ID	A.L.-1	A.L.-2	A.L.-3	A.L.-4
Material Type	Adiprene L-100			
Impact Velocity(m/s)	0.65	1.0	1.0	2.0
Original Height(mm)	10.7			
Final height(mm)	10.7	10.7	10.7	10.1
Original Diameter(mm)	15.75	15.6	15.6	15.6
Max Engineering strain (Compression)	9%	17.7%	17.7%	39%
Plastic strain (Compression)	0	0%	0%	5.6%

The deforming images of A.L.-4 are shown in Figure 6-9. The initial shape of the sample is the upper picture and the maximum strain is depicted in the lower picture. Slightly barreling effect is observed in the images and this phenomenon is compared with LS-DYNA simulation by Aaron[5] in the frame of research collaboration.

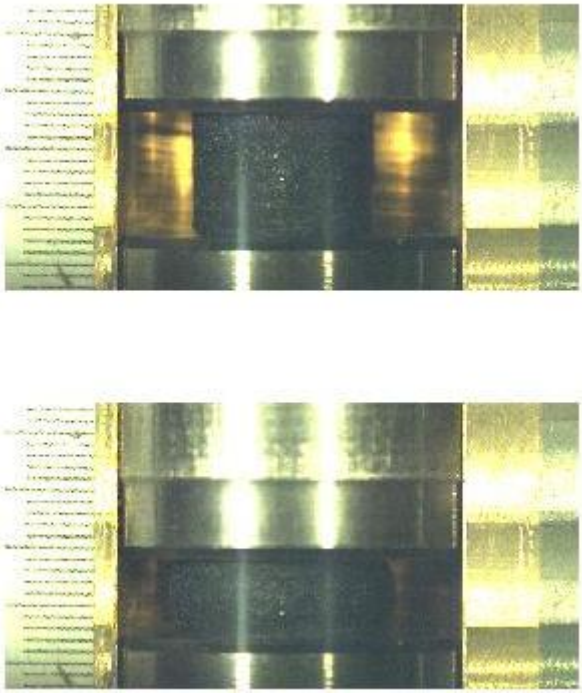

Figure 6-9 Images of Adiprene L-100 during a soft drop weight test with impact velocity 2m/s. The upper picture corresponds to the initial shape and the lower picture indicates the maximum strain.

The testing condition of A.L.-2 and A.L.-3 are set to be the same to show the repeatability of the testing of Adiprene L-100. The engineering stress over engineering strain curves of A.L-2 and A.L.-3 are compared in Figure 6-10. The strain data is derived from optical images and stress data is measured using strain gauges as discussed in chapter 5. There's no residual deformation after the impact test. A good repeatability is shown by the similarity of the two curves.

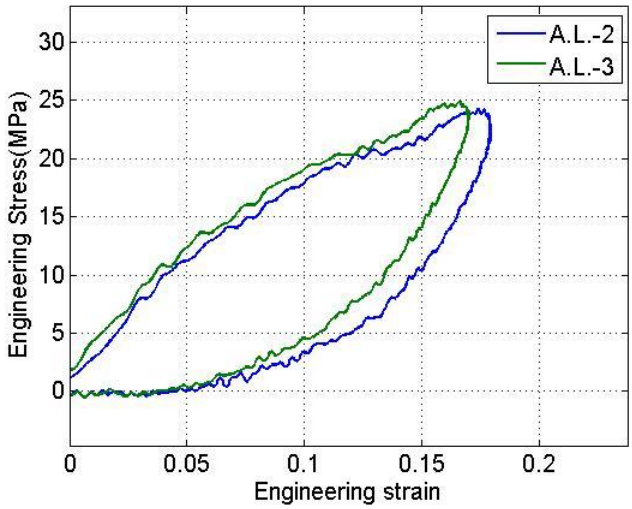

Figure 6-10 Engineering stress versus engineering strain of Adiprene L-100 samples using soft drop weight tests with impact velocity 1m/s. A.L.-2 and A.L.-3. are two tests with the same setup to show repeatability.

The engineering stress strain relation is plotted in Figure 6-11. Adiprene L-100 was tested using soft drop weight test with impact velocity 0.65m/s (A.L.-1) 1m/s (A.L.-2) 2m/s (A.L.-4). The engineering stress under dynamic deformation is compared with static data measurement independently. It's shown that the loading part of the curves A.L.- 1, A.L.-2 and A.L.-4 are all greater than static curve, which can be explained by the characteristic property of viscoelastic materials. The stress corresponds to higher strain-rate with impact velocity 2m/s is higher than that with impact velocity 1m/s. The

loading and unloading data presented in the figure is used to generate tabulated data used for Blast Simulator elastomer material model “MAT-183” [5].

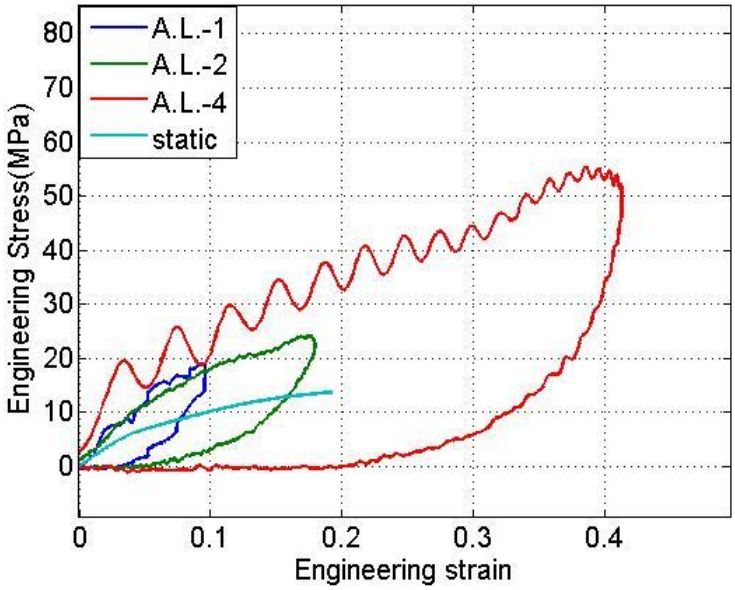

Figure 6-11 Engineering stress versus engineering strain of Adiprene L-100 samples using soft drop weight test with impact velocity 0.65m/s (A.L.-1) 1m/s (A.L.-2) 2m/s (A.L.-4).

6.3 Soft Drop Weight Test on Al-W CIPed/HIPed composites

High density (theoretical density of 7.8 g/cm^3) and low strength aluminum-tungsten granular/porous composites were prepared from elemental powder of Al (Alfa Aesar 4.5-7 μm), and different particle sizes and morphology of W: coarse W (Alfa Aesar,-325 mesh), fine W (Alfa Aesar <1 μm) and W wires (A-M system, diameter of 200 μm and length of 4mm). Two layers of W coils (14mm diameter for outer layer and 9mm diameter for inner layer) were added axially to some samples with W wires. Cold Isostatic Pressing (CIPing) was used and some samples were Hot Isostatic Pressed (HIPed) with vacuum encapsulation after CIPing. All samples had identical mass ratios of Al and W components (23.8% Al and 76.2% W, by weight, corresponding to volume ratio

of 69.0% Al and 31.0% W). Mixtures of Al and W component were ball-milled in an alumina vial set for 10 minutes using alumina balls with 1:5 mass ratio of balls to powder. The mixtures were then placed in a cylindrical stainless steel mandrel with moving pistons and encapsulated in rubber jacket providing axial loading during pressurization in CIP chamber. This allowed preparation of samples with exact sizes and cylindrical shape which are necessary for strength measurements. All samples were CIPed at 345 MPa under room temperature for 5 min. Subsequent HIPing for some samples are carried out at 200 MPa under temperature of 500 degree Celsius for 20 minutes.

The soft drop weight test is a good approach to measure high strain-rate properties of low strength composite materials. 7 tests on Al/W composites with different structure and processing method are listed in Table 6-3. All the samples are tested using soft drop weight test assisted with o-rings 3mm in cross section diameter. A high speed camera was used to capture deformation history and evaluate engineering strain of the samples. The deforming pictures of each sample are shown in the figures from Figure 6-12 to Figure 6-18. True Stress calculated using strain gauges measurement over true strain is shown in Figure 6-19 and Figure 6-20 assuming homogeneous deformation and constant volume.

Table 6-3 Description of Al/W composites with different Mesostructure after different processing routes (CIPed, CIPed twice, CIPed and HIPed)and testing conditions in soft drop weight tests.

ID	Material	Processing	Velocity	Yield Stress (MPa)	Flow Stress (MPa)	Max Strain
#1	Al Powder and W Wires	CIP Twice	7m/s	220	220~380	0.22
#2	Al Powder and W Wires/Coils	CIP	7m/s	220	220~280	0.25
#3	Al Powder and W Wires/Coils	CIP/HIP	7m/s	210	210~300	0.2
#4	Al Powder and Coarse W (ALCW)	CIP	7m/s	170	<20	
#5	Al Powder and Coarse W (ALCW)	CIP/HIP	7m/s	170	170~240	0.32
#6	Al Powder and Fine W (ALFW)	CIP	3m/s	85	<20	
#7	Al Powder and Fine W (ALFW)	CIP/HIP	7m/s	100	<20	

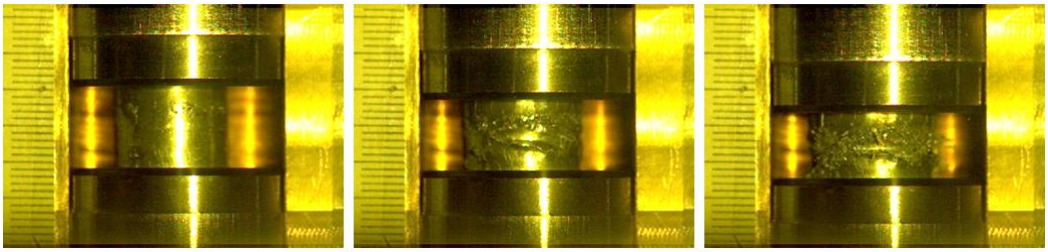

Figure 6-12 High speed images of dynamically deformed pictures of the composite processed from Al powder and W wires. The sample was CIPed twice.

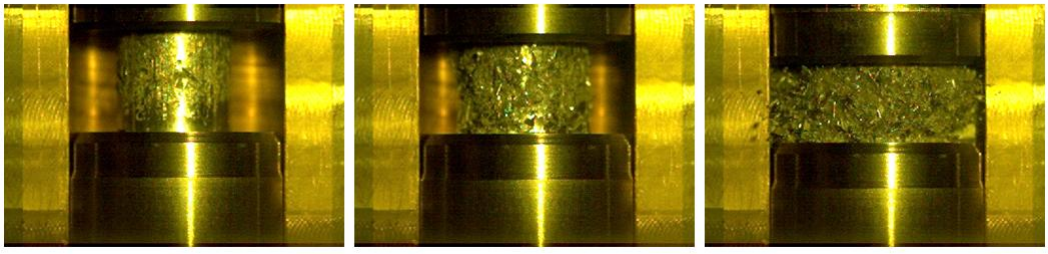

Figure 6-13 High speed images of dynamically deformed pictures of the composite processed from Al powder and W wires/coils. The sample was CIPed once.

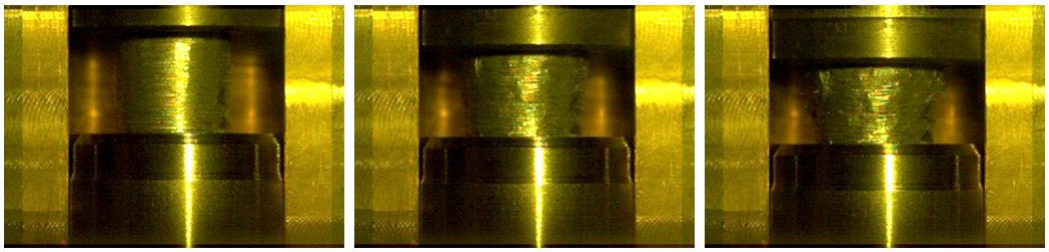

Figure 6-14 High speed images of dynamically deformed pictures of the composite processed from Al powder and W wires/coils. The sample was CIPed and HIPed.

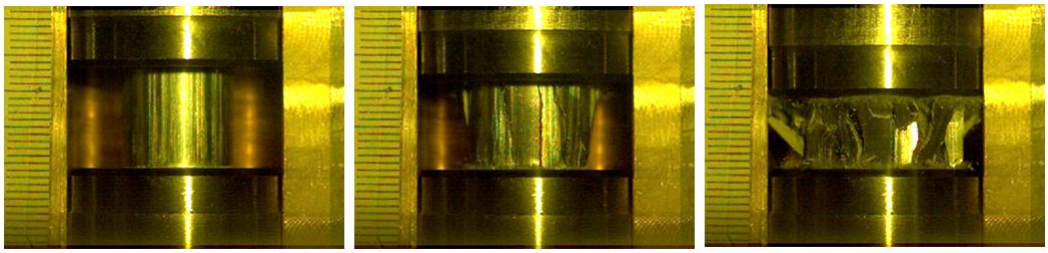

Figure 6-15 High speed images of dynamically deformed pictures of the composite processed from Al powder and coarse W powder. The sample was CIPed once.

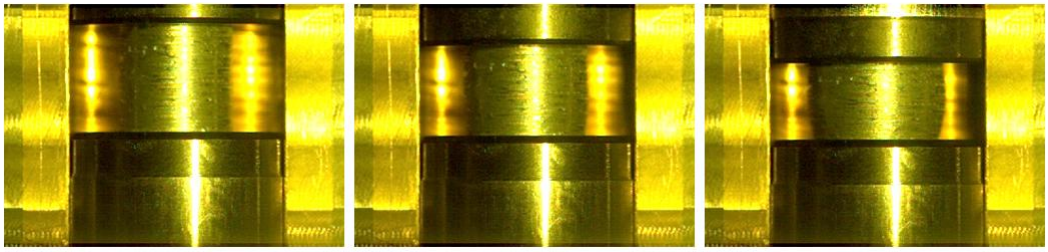

Figure 6-16 High speed images of dynamically deformed pictures of the composite processed from Al powder and coarse W powder. The sample was CIPed and HIPed.

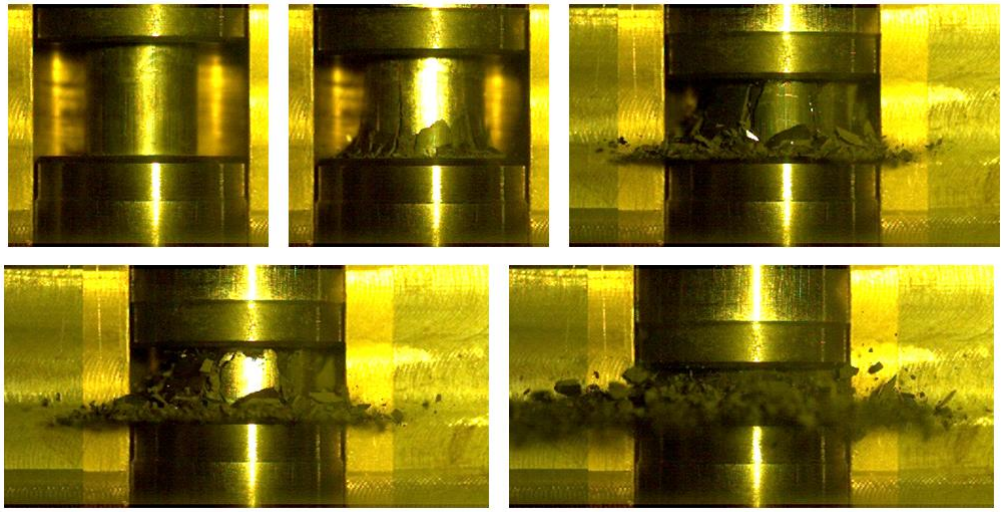

Figure 6-17 High speed images of dynamically deformed pictures of the composite processed from Al powder and fine W powder. The sample was CIPed once.

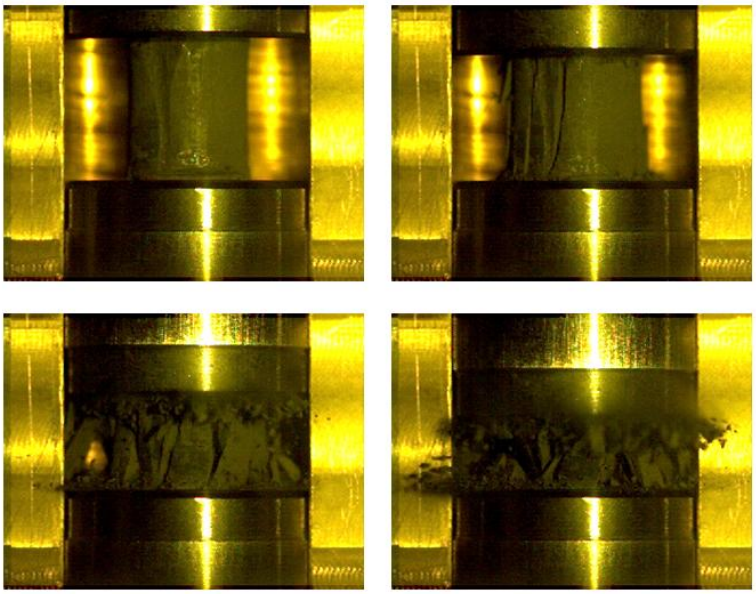

Figure 6-18 High speed images of dynamically deformed pictures of the composite processed from Al powder and fine W powder. The sample was CIPed and HIPed.

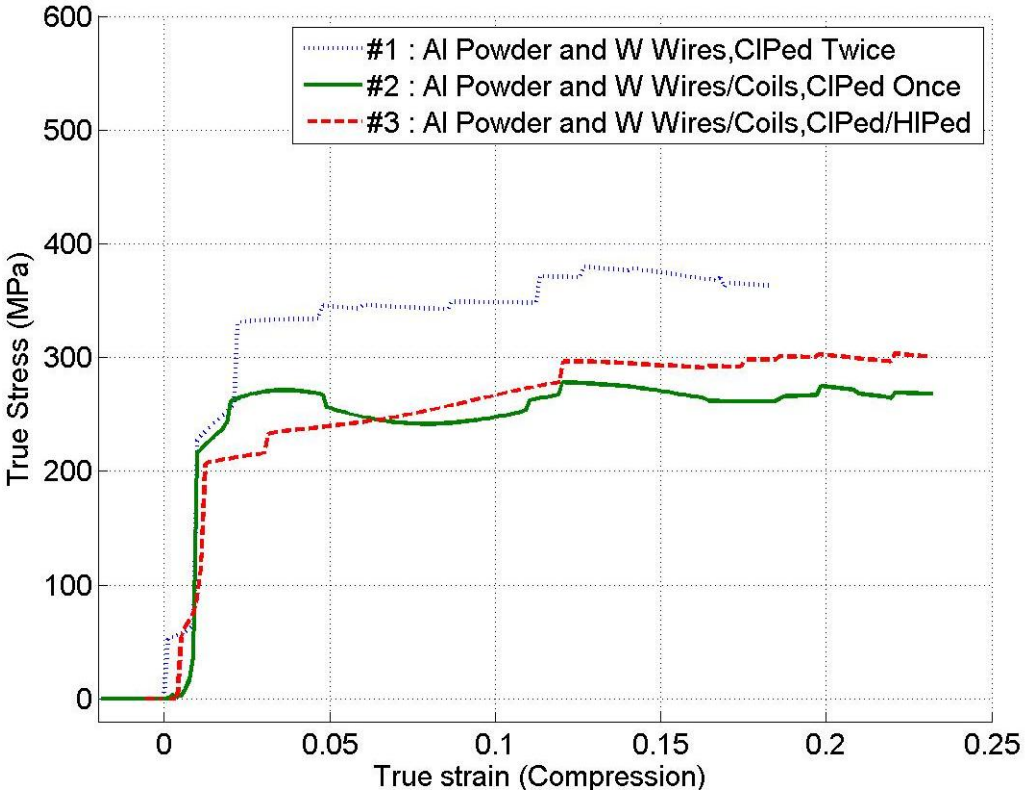

Figure 6-19 Stress strain relation of the sample processed from Al powder and W wires and was CIPed twice; the sample processed from Al powder and W wires/coils and was CIPed; the sample processed from Al powder and W wires/coils and was CIPed and HIPed. Soft drop weight tests with impact velocity 7 m/s

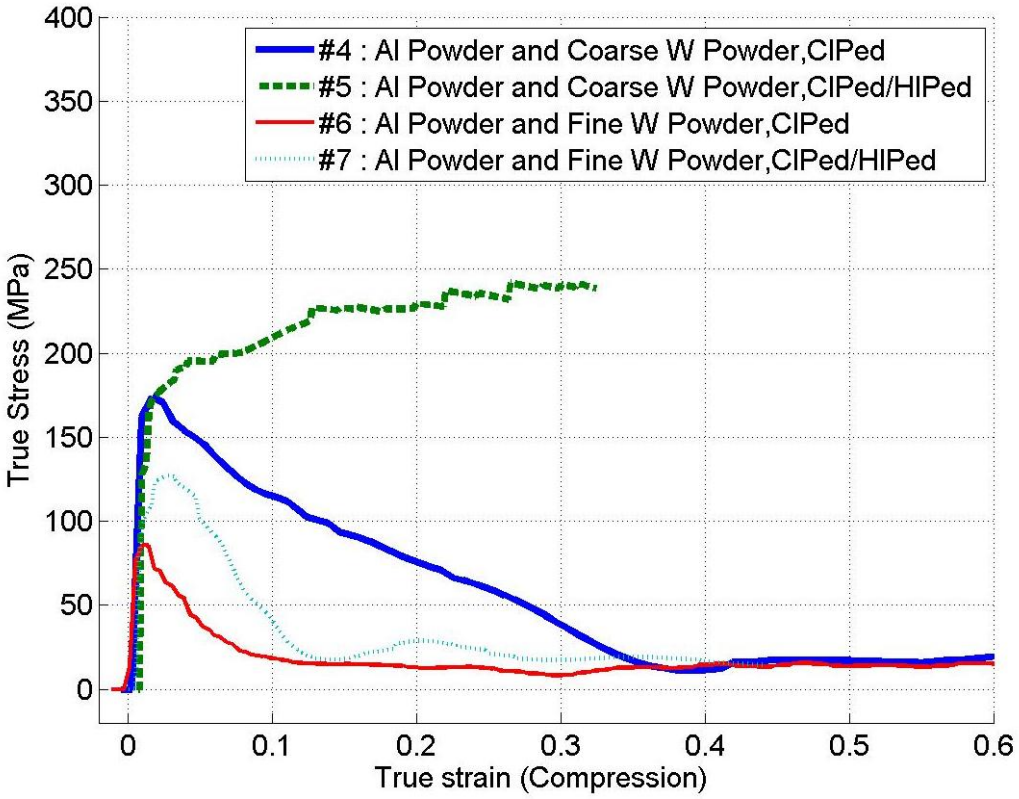

Figure 6-20 Stress strain curves of AlCW-CIP, AlCW-CIP/HIP, AlFW-CIP, AlFW-CIP/HIP. Except for AlFW-CIP which was impacted by 3m/s, all the other samples were impacted by 7m/s using soft drop weight tests.

The 7 samples can first be separated into two groups: the ones containing W wires and coils (samples #1-3) and the ones containing W powder (samples #4-7). In general the strength of samples with W wires is stronger because the tangling of W wire would trap Al mesh from flowing.

By comparing the deforming images of three samples with W wires (#1, #2, and #3)in Figure 6-12, Figure 6-13, and Figure 6-14, we can see that the different combination of material type and processing procedures would affect dynamic deformation. For example, after the high strain-rate deformation, sample #2(CIPed once) ejected large number of Al, W debris and short W wires. Sample #1(CIPed twice) generally remained its whole structure and only slight amount of debris was collected

after the test. Sample #2 has additional W coils to strengthen the composition. The design of sample #2 assumed that the introduction of two layers of cylindrical W coils inside the sample would provide stronger structure. The fact that sample #2 had much more debris than sample #1 shows that the second CIP effectively reduced porosity and add strength to the sample even more than adding W coils to the sample. There's almost no debris observed in sample #3 supporting the expectation that additional HIPing would increase connectivity between Al particles and greatly reduce the amount of small debris produced during impact.

Figure 6-19 shows the stress strain curves of samples #1, #2, and #3. The yielding strength of samples #1 and #2 is similar at 220 MPa, which is close to the yielding strength of Al6061-T6 [1], showing that the CIP process effectively pressed Al powder together and the yield strength is close to pure aluminum. The yielding stress of sample #3 is at 200 MPa and is slightly lower than sample #2. The difference between samples #2 and #3 is that sample #3 experienced one more HIP process. It's known that Al6061-T6 would lose the work hardening and become Al6061-0 after annealing and it can support this observation. The yielding strength of Al6061-0 is reported to be around 100 MPa [4]. Partial annealing of Al powder in the second HIP might decrease the yielding strength of sample #3 slightly. Sample #1 has the highest flow stress close to 380 MPa showing that a second CIP can greatly increase its yielding strength and flow stress. Samples #2 and #3 have similar flow stress about 300 MPa suggests that the additional HIP process won't increase overall strength of the sample. However, the HIP process would fuse Al powder and increase the connectivity between Al particles. This increased connectivity should also increase the sample's strength. It's also known that

HIP may also trigger partial annealing mechanism of Al and reduce its strength. The combined effect from increasing connectivity and decreasing individual strength contribute to the fact that sample #3 has similar flow stress as sample #2.

The deformation pictures of Al and W powder based samples #4-#7 are shown in Figure 6-15 to Figure 6-18. Sample #4 and sample # 5 are fine Al and coarse W powder composites. Sample #6 and sample #7 are made of fine Al and fine W powder. Three samples (#4, #6, and #7) of the four powder based materials are completely crashed after the impact. From Figure 6-15 , large cracks are observed on the wall from the top to the bottom in the beginning of the deformation of sample #4 followed by scattered powder and fragment separated from the sample. Sample #5(FALCW-CIP/HIP) is a special case because it maintained its shape as a cylinder after the impacted by the drop mass and only little amount of debris were separated from the sample. By comparing the deformation images of sample #4(FALCW-CIP) and sample #5(FALCW-CIP/HIP), it's found that the additional HIP process greatly increases the bonding between Al powder allowing resistance to large plastic deformation without fracture. Both samples #6 and #7 shattered similar to sample #4 after the impact. The fragments from sample #7 is larger than that in sample #6 demonstrating that the extra HIP process applied to sample #7 increases the bonding between Al powder. The impact test on sample #6 developed the largest amount of fragments and had the broader area of separated fragments.

Figure 6-20 shows the stress strain curves of samples #4, #5, #6, and #7. The strength of each sample follows the order: FALCW-CIP/HIP > FALCW-CIP > FALFW-CIP/HIP > FALFW-CIP/HIP. The sample #5 (FALCW-CIP/HIP) has the highest yielding stress at 170 MPa and exhibit a flow stress at 240 MPa in response to impact

deformation. It should be stressed that sample #5 is the only one among the four powder based Al-W composite to show a flow stress higher than yield stress. Sample #4 (FALCW-CIP) has similar yielding stress as #5 at 170 MPa and the true stress quickly decreased to 20 MPa as true strain reached 0.35. A hypothesis of deforming mechanism is that the connection between Al powder from CIP (sample #4) is not strong and large amount of shear bands grow inside the sample until disintegration of the structure. The composites made of coarse W powder (samples #4, #5) are stronger than the composites made of fine W powder (samples #6, #7). Sample #6 had the lowest yielding stress at 85 MPa and the true stress fast decreased to 20 MPa as strain increase to 0.1. Comparison of the maximum true stress of samples #6(CIP) and #7(CIP and HIP) shows that the additional HIP process slightly increases the strength of the sample. However, the combination of fine Al and fine tungsten after CIP and HIP (sample #7) didn't form the matrix as strong as the composites made of fine Al and coarse tungsten (sample #5). A possible explanation is that the combination of coarse tungsten and fine Al allows more Al particles fill the gap between W powder of diameter 40 μm providing better strength of Al matrix after HIPing.

Chapter 6 contains part of materials in the paper "Characterization of the Blast Simulator Elastomer Material Using a Pseudo-Elastic Rubber Model" in International Journal of Impact Engineering and in paper "Roles of Material Properties and Mesostructure on Dynamic Deformation and Shear Instability in Al-W Granular Composites" in Journal of Applied Physics. The dissertation author conducted experiments and obtained results on Adiprene L-100 and Al/W sample using soft drop weight tests. Chapter 6 contains material currently being prepared for publication of "Soft

drop weight tests of low strength materials." The dissertation author was the primary investigator and author of this material.

6.4 References

1. C. J. Maiden, and S. J. Green, (1966). "Compressive strain-rate tests on six selected materials at strain rates from 10^{-3} to 10^{4} /s." Journal of applied mechanics, 33(3), 496.

2. D. R. Christman, W. M. Isbell, S. G. Bobcock, A. R. McMillan, and S. J. Green, (1971). " Measurements of dynamic properties of materials." Material and Structures Labortory, General Motor Corporation, 3,1.

3. C. W. Jiang, M. M. Chen, (1974). "Dynamic properties of materials aluminum alloys." Defense Technical information Center, 2,1.

4. U. S. Lindholm, and R. L. Bessey, (1969). "A survey of rate dependent strength properties of metals." Southwest research inst. San Antonio, Dept. of mechanical sciences. 1.

5. A. Freidenberg, C.W. Lee, B. Durant, V. F. Nesterenko, L. K. Stewart, G. A. Hegemier, (2013) "Characterization of the Blast Simulator elastomer material using a pseudo-elastic rubber model." International Journal of Impact Engineering, 60, 58.

CHAPTER 7

SUMMARY

A commercial drop tower Instron Dynatup 9250 HV was modified to conduct compression impact tests including dynamic tests of single o-ring, dynamic tests of pre-compressed o-rings and soft drop weight tests assisted with o-rings. Force measurement from strain gauges and accelerometers validate the force equilibrium condition during the impact tests. Deformation history of the samples independently recorded by a high speed camera is processed by the image tracking algorithm to extract engineering strain of the samples with accuracy up to 1 pixel size.

The instrumented dynamic tests provide reliable data to analyze the strongly nonlinear viscoelastic dynamic response of toroidal rubber elements (o-rings). The displacements of drop mass based on integrating its acceleration using data from load cell agree with that observed from optical images. Force over engineering strain curves indicates strain and strain rate dependent, strongly non-linear dynamic force-strain relations for o-rings.

Nonlinear dynamic model using strain-rate dependence initially proposed for contact of spherical particles by Brilliantov et. all, and Morgado et. all is modified for nonlinear viscoelastic dynamic response of o-rings. The model successfully describes the difference between static behavior of o-rings and dynamic force measurement in the experiments reasonably for low strains and strain rates. But the dynamic model using linear strain rate dependence did not satisfactory agree with experimental data at larger

strain and strain rates. Weaker than linear strain-rate dependence is observed in impact tests with various initial velocities. A modified model with power-law strain-rate dependence is proposed based on experimental results and it describes the strongly nonlinear behavior of o-ring in a whole investigated range of strains and strain-rates. Logarithm strain-rate dependence is also considered as another possible solution to explain the weaker than linear dependence of viscous term in total force.

The testing results of pre-compressed o-rings express softer behavior or o-rings in comparison with smaller or no pre-compression demonstrating a memory effect. This behavior of pre-compressed o-rings was explained using model considering memory effect as a function of current engineering strain, initial pre-compression, and initial strain-rate. This model confirmed the observation from experiment that pre-compression of o-rings contribute to dynamic stiffness and performs stiffer in the initial stage of deformation.

The “soft” drop weight impact test using o-ring can greatly decrease high-frequency excitations by ramping the applied forces, which will be useful for the testing of low strength samples of reactive materials. Accurate engineering strain of the sample is recorded by a high speed camera and stress data is measured by strain gauges. It was confirmed that force data can be used to derive the displacement of the drop mass and change of o-ring height. Thus, the strain history of samples can also be estimated solely from force measurement using a fully calibrated drop tower.

High strain–rate stress strain relations of Al 6061-T6 and Al 6061-0 are measured using soft drop weight tests and the results are in agreement with data reported in literatures using Hopkinson Split Pressure Bar. The testing on aluminum samples

validate the accuracy of stress and strain measurement used in soft drop weight tests. Soft drop weight tests have advantages over HSPB for it is easier to operate and it can measure stress-strain relation for large strain and in post critical stages response of samples.

The soft drop weight test was used for constructing strain-rate dependent stress-strain relation of Adiprene L-100. The loading and unloading curves of Adiprene L-100 under different strain-rates are measured using soft drop weight tests and it' s successfully used to generate tabulated date for elastomer material model applied to tailoring load in UCSD Blast Simulator..

Stress strain relations of Al-W composites are measured using soft drop weight tests. Mechanisms of deformation are significantly different for different mesostructure generated by different processing. Samples mixed with W wires are significantly stronger than the ones composed of only powders. Aluminum powder and W wire composite after CIPing twice at 345 MPa shows a yielding strength of 220 MPa and flow stress about 380 MPa. Aluminum powder and W wire/coil after CIPing shows a yielding stress 220MPa and flow stress about 280 MPa. Additional HIPing of Aluminum powder and W wires/coils slightly reduced the yield stress to 210 MPa and flow stress slightly increased to 300.

Dynamic tests on Al-W powder based composited indicates that under the same processing routes, fine Al / coarse W composites are stronger than fine Al / fine W composites. Fine Al / fine W composites after CIPing at 345 MPa show a yielding stress at 85 MPa and fine Al / fine W composites after CIPing and HIPing have a yield stress of 100 MPa. Both of them couldn't resist large plastic deformation and

disintegrated quickly after yielding.

Fine Al / coarse W composites after CIP show a yielding strength of 170 MPa and the structure shattered after yielding with relatively small flow stress. Additional HIPing after CIPing of fine Al / coarse W composites show similar yielding strength of 170 MPa but surprisingly increasing their flow stress up to 240 MPa. This indicated that the additional HIPing process increases the bonding between Al powder forming stronger Al matrix and allowing large plastic deformation without disintegration.